

**IMPROVEMENTS FOR CHIP-CHIP INTERCONNECTS AND
MEMS PACKAGING THROUGH MATERIALS AND PROCESSING
RESEARCH**

A Dissertation
Presented to
The Academic Faculty

by

Erdal Uzunlar

In Partial Fulfillment
of the Requirements for the Degree
Doctor of Philosophy in the
School of Chemical & Biomolecular Engineering

Georgia Institute of Technology
May 2015

COPYRIGHT© 2015 BY ERDAL UZUNLAR

**IMPROVEMENTS FOR CHIP-CHIP INTERCONNECTS AND
MEMS PACKAGING THROUGH MATERIALS AND PROCESSING
RESEARCH**

Approved by:

Dr. Paul A. Kohl, Advisor
School of Chemical & Biomolecular
Engineering
Georgia Institute of Technology

Dr. Dennis W. Hess
School of Chemical & Biomolecular
Engineering
Georgia Institute of Technology

Dr. Michael A. Filler
School of Chemical & Biomolecular
Engineering
Georgia Institute of Technology

Dr. Azad Naeemi
School of Electrical and Computer
Engineering
Georgia Institute of Technology

Dr. Yogendra Joshi
School of Mechanical Engineering
Georgia Institute of Technology

Date Approved: January 8, 2015

To my family

ACKNOWLEDGEMENTS

I would first like to express my sincerest gratitude to my advisor, Prof. Paul A. Kohl, for his precious guidance, encouragement and support during my time in Georgia Tech. I would also like to thank my thesis committee members, Prof. Dennis W. Hess, Prof. Michael A. Filler, Prof. Azad Naeemi and Prof. Yogendra Joshi for their helpful input to my Ph.D. study.

I would also like to give thanks to the current and past members of Kohl group. Thank you in particular to Dr. Rohit Sharma, Dr. Rajarshi Saha, Dr. Yu-Chun Chen, Dr. Hyo-Chol Koo, Dr. Mehrsa Raeiszadeh, Dr. Murat Unlu, Zachary T. Wilson, Jared M. Schwartz and Brennen K. Mueller for their help with the work presented in this thesis, and encouragement throughout my Ph.D. study. Thank you to IEN cleanroom staff, especially Walter Henderson, Gary Spinner and Eric Woods for all their assistance throughout my time in the cleanroom.

This work would not have been possible without the support of Promerus, LLC, Sumitomo Bakelite, Co. Ltd. and Raytheon Company. I would like to acknowledge Dr. Ed Elce of Promerus, LLC for his insight.

Finally and most importantly, I would like to thank to my parents, Zuhre and Celil Uzunlar, my sister Gulsen Uzunlar Altin, and my wife, Sibel Kalyoncu Uzunlar, for all their encouragement and support throughout the years. Without them, I would have never dreamed of making it to this point. I praise God for endowing me with such a supportive and loving family, and for providing me with enthusiasm and patience to pursue my goals in life.

TABLE OF CONTENTS

	Page
ACKNOWLEDGEMENTS	iv
LIST OF TABLES	viii
LIST OF FIGURES	ix
LIST OF ABBREVIATIONS	xii
LIST OF SYMBOLS	xiv
SUMMARY	xv
 <u>CHAPTER</u>	
1 Introduction and Background	1
1.1 Project Motivation	1
1.2 Background	2
1.2.1 Electroless Copper Deposition on PWBs for Chip-Chip Interconnection	2
1.2.2 Polymer-based Air-gap MEMS Packaging	12
1.2.3 Thermal Stability Enhancement of Poly(propylene carbonate)	18
1.3 Research Objectives	22
2 Experimental	23
2.1 Electroless Copper Deposition on PWBs for Chip-Chip Interconnection	23
2.1.1 Materials	23
2.1.2 Processing	23
2.1.2.1 Surface Pretreatment Methods	23
2.1.2.2 Electroless Copper Deposition Procedure	24
2.1.3 Analysis Techniques	25

2.1.3.1	Measurement of Electroless Copper Deposition Rate	25
2.1.3.2	Measurement of Adhesion Strength of Electrolessly Deposited Copper on PWB	25
2.1.3.3	Surface Roughness Determination	26
2.1.3.4	Chemical Characterization of Surfaces	27
2.2	Polymer-based Air-gap MEMS Packaging	28
2.2.1	Materials	28
2.2.2	Processing	29
2.2.2.1	Purification of PPC	29
2.2.2.2	Preparation of Photosensitive PPC solution	30
2.2.2.3	Air-gap Formation Processes	30
2.2.3	Analysis Techniques	34
2.2.3.1	Thermal Characterization of Different PPC types	34
2.2.3.2	Chemical Structure Determination of PPCs using Nuclear Magnetic Resonance	34
2.2.3.3	Mechanical Characterization of Overcoat using Nanoindentation	35
2.2.3.4	Chemical Characterization and Thickness Measurement of PPC Residue	35
2.3	Thermal Stability Enhancement of Poly(propylene carbonate)	37
2.3.1	Materials	37
2.3.2	Processing	40
2.3.2.1	Preparation of PPC/PAG Solutions	40
2.3.2.2	Preparation of Copper-Sputtered Substrates and PPC/PAG Coating	41
2.3.3	Analysis Techniques	42
2.3.3.1	Thermal Characterization of PPC/PAG Films	42

2.3.3.2	Copper Oxidation State Determination on the Surface of PPC/PAG Films	42
2.3.3.3	Investigation of Photobleaching in PPC/PAG Films	43
3	Electroless Copper Deposition using Tin-Silver Catalyst on Epoxy Laminates	45
3.1	Results	46
3.2	Discussion	64
3.3	Summary and Conclusions	69
4	Size-compatible, Polymer-based Air-gap Formation Processes and Polymer Residue Analysis for Wafer-level MEMS Packaging Application	71
4.1	Results and Discussion	72
4.2	Summary and Conclusions	93
5	Thermal and Photocatalytic Stability Enhancement Mechanism of Poly(propylene carbonate) due to Copper(I) Impurities	94
5.1	Results	94
5.2	Discussion	108
5.3	Summary and Conclusions	110
6	Conclusions and Suggestions for Future Work	111
	REFERENCES	116

LIST OF TABLES

	Page
Table 2.1: Trade names, suppliers and chemical structures of PAGs	38
Table 2.2: The molecular weights (g/mol) and required amounts of PAGs in the solutions expressed as wt% of PPC	41
Table 3.1: The average (R_a) and root-mean-square (R_q) surface roughness values measured for samples at each step in electroless deposition process	50
Table 3.2: The atomic percentage of elements in samples obtained from XPS survey spectra	53
Table 3.3: C1s peak deconvolution results of as-received PWB sample	58
Table 3.4: C1s peak deconvolution results of H ₂ SO ₄ treated PWB sample	59
Table 3.5: C1s peak deconvolution results of H ₃ PO ₄ treated PWB sample	60
Table 3.6: C1s peak deconvolution results of HCl treated PWB sample	61
Table 3.7: Sn peak deconvolution results	63
Table 3.8: Ag peak deconvolution results	64
Table 4.1: Carbon functionalities in non-photosensitive PPC residue	89
Table 4.2: Carbon functionalities in photosensitive PPC residue	90
Table 5.1: XPS analysis results for elements and relative percentages	97
Table 5.2: UV-vis spectra peak wavelength (nm) and absorbance (AU) values	108

LIST OF FIGURES

	Page
Figure 1.1: Chip-chip interconnection on PWB with copper traces	3
Figure 1.2: The processes taking place during swell-and-etch application	9
Figure 1.3: Comparison of growth rates in MEMS packaging sector versus IC packaging sector	13
Figure 1.4: Cross-sectional and 3-D view of MEMS packaging using wafer capping	14
Figure 1.5: Dynamic TGA plots for PPC films in GBL cast on a copper surface and cast on silicon with and without UV exposure compared with decomposition of neat PPC without UV exposure	21
Figure 2.1: Air-gap formation process flows for (a) RIE process, and (b) Direct photopatterning process	32
Figure 3.1: The amount of electroless copper deposited per area on epoxy laminates versus duration of electroless copper deposition	46
Figure 3.2: AFM surface roughness profiles and surface roughness values R_a and R_q obtained from (a) plain epoxy laminate sample, (b) 1 min H_2SO_4 treated sample, (c) 30 min H_2SO_4 treated sample, (d) 3 hr H_2SO_4 treated sample, and (e) swell&etch sample	49
Figure 3.3: As-received PWB XPS survey spectrum	54
Figure 3.4: High resolution XPS C1s spectrum, peak fit and peak deconvolution for as-received PWB sample	58
Figure 3.5: High resolution XPS C1s spectrum, peak fit and peak deconvolution for H_2SO_4 treated PWB sample	59
Figure 3.6: High resolution XPS C1s spectrum, peak fit and peak deconvolution for H_3PO_4 treated PWB sample	60
Figure 3.7: High resolution XPS C1s spectrum, peak fit and peak deconvolution for HCl treated PWB sample	61
Figure 3.8: Ag activated PWB sample high resolution XPS spectrum, peak fit and peak deconvolution for Sn	63

Figure 3.9: Ag activated PWB sample high resolution XPS spectrum, peak fit and peak deconvolution for Ag	64
Figure 4.1: TGA results of neat and purified Novomer 160K	73
Figure 4.2: TGA results of neat and purified QPAC 40 141K	73
Figure 4.3: The chemical structure of PPC with carbon and hydrogen atoms labeled for referencing to NMR signals	74
Figure 4.4: ^{13}C -NMR spectra for neat QPAC 40 141K (top), neat Novomer 160K (middle) and purified Novomer 160K PPC (bottom)	75
Figure 4.5: ^1H -NMR spectra for neat QPAC 40 141K (top), neat Novomer 160K (middle), and purified Novomer PPC 160K (bottom)	78
Figure 4.6: Kinetic comparison between BCB curing and PPC decomposition processes at (a) 170°C, (b) 190°C, and (c) 210°C	81
Figure 4.7: Top-view optical images and Dektak profiles of a 2.5x3.2 mm air-gap feature obtained from a medium thick non-photosensitive PPC sample subjected to two-step thermal treatment of 1.3 hr at 190°C and 11 hr at 240°C	83
Figure 4.8: An XPS depth profile obtained from the air-gap region of a medium thick non-photosensitive PPC sample with initial PPC thickness of 19.3 μm subjected to a two-step thermal treatment of 1.3 hr at 190°C and 13 hr at 240°C	84
Figure 4.9: The configurations of two-layer PPC film for direct photopatterning process, where (a) photosensitive PPC layer is at the bottom, and (b) photosensitive PPC layer is on top	86
Figure 4.10: An XPS depth profile obtained from the air-gap region of a two-layer PPC sample with initial photosensitive (PAG-loaded) PPC at the bottom (2.8 μm), and non-photosensitive PPC on top (23.5 μm) subjected to a three-step thermal treatment of 30 hr at 150°C, 30 hr at 180°C and 11 hr at 240°C	87
Figure 4.11: High resolution XPS scan, peak fit and peak deconvolution of C1s peaks obtained from non-photosensitive PPC residue	89
Figure 4.12: High resolution XPS scan, peak fit and peak deconvolution of C1s peaks obtained from photosensitive PPC residue	90
Figure 5.1: XPS elemental survey scan of surface of a PPC film cast on copper surface, UV exposed, and post-baked	96

Figure 5.2: High resolution XPS Cu scan on surface of a PPC film cast on copper surface, UV exposed, and post-baked	97
Figure 5.3: TGA results for PPC film containing sulfonium-based PAG TAPSPS-FABA	99
Figure 5.4: TGA results for PPC film containing sulfonium-based PAG TAPSPS-TMM	99
Figure 5.5: TGA results for PPC film containing iodonium-based PAG BTBPI-TF	102
Figure 5.6: TGA results for PPC film containing iodonium-based PAG BTBPI-NF	102
Figure 5.7: TGA results for PPC film containing iodonium-based PAG DPI-TF	103
Figure 5.8: UV-vis spectroscopy results of PPC films on copper and on silicon with or without UV exposure	107

LIST OF ABBREVIATIONS

IC	Integrated Circuit
MEMS	Microelectromechanical Systems
PPC	Poly(propylene carbonate)
PWB	Printed Wiring Board
XRD	X-ray Diffraction
XPS	X-ray Photoelectron Spectroscopy
AFM	Atomic Force Microscopy
AC	Alternating Current
DC	Direct Current
POSS	Polyhedral Oligomeric Silsesquioxane
FR-4	Flame Resistant Epoxy Laminate
CAGR	Compound Annual Growth Rate
GBL	Gamma-Butyrolactone
BCB	Benzocyclobutene
RIE	Reactive-ion Etching
EDS	Energy-Dispersive X-ray Spectroscopy
PAG	Photoacid Generator
UV	Ultraviolet
UV-vis	Ultraviolet-visible
DI	De-Ionized
EDTA	Ethylenediaminetetraacetic Acid
PEG	Polyethylene Glycol
ASTM	American Society for Testing and Materials

TGA	Thermogravimetric Analysis
NMR	Nuclear Magnetic Resonance
Rhodorsil-FABA	4-methylphenyl[4-(1-methylethyl)phenyl]iodonium tetrakis(pentafluorophenyl)borate
BTBPI-TF	Bis(4-tert-butylphenyl)iodonium triflate
BTBPI-NF	Bis(4-tert-butylphenyl)iodonium perfluoro-1- butanesulfonate
DPI-TF	Diphenyliodonium triflate
TAPSPS-FABA	Tris[4-(4-acetylphenyl)sulfanylphenyl]sulfonium tetrakis(pentafluorophenyl)borate
TAPSPS-TMM	Tris[4-(4-acetylphenyl)sulfanylphenyl]sulfonium tris(trifluoromethylsulfonyl)methide

LIST OF SYMBOLS

T_g	Glass Transition Temperature
R_a	Arithmetic Average Surface Roughness
R_q	Root-mean-squared Surface Roughness
δ	Skin Depth
ρ	Electrical Resistivity
f	Frequency
μ_o	Magnetic Permeability of Free Space
μ_r	Relative Magnetic Permeability
R	Electrical Resistance
l	Length
A	Cross-Sectional Area
P	Pressure
h	Vertical Deflection
t	Membrane Thickness
a	Radius of Membrane
σ_o	Residual Stress
E	Elasticity Modulus
ν	Poisson's Ratio

SUMMARY

The work presented in this dissertation focuses on improvements for ever-evolving modern microelectronic technology. As the microelectronics technology progresses, new challenges in materials and processing are faced and need to be resolved. Improvements in metallization, packaging and the materials used in these processes can further enable reducing cost, and attaining higher performance. Specifically, three topics were investigated in this work: electroless copper deposition on printed wiring boards (PWBs), polymer-based air-gap microelectromechanical systems (MEMS) packaging technology, and thermal stability enhancement in sacrificial polymers, such as poly(propylene carbonate) (PPC). Electroless copper is important in the fabrication of electronic substrates for the formation of dense copper wiring traces on printed wiring boards (PWBs). Electroless copper deposition on PWB materials currently uses costly Pd-based catalysts. The conventional surface pretreatment of PWBs by swell-and-etch method increases the surface roughness dramatically, which leads to high conductor losses that limit the signal propagation speed and integrity between chips on PWB substrates. In that regard, low-cost and equally active Ag-based catalysts, and non-roughening surface treatment methods using mineral acids were investigated for improved electroless copper deposition processes. MEMS packaging plays an important role in protecting MEMS devices, in preserving device performance and in the final product cost. The industrial standard of wafer capping is a heterogeneous process that requires careful alignment of MEMS and capping wafers and bonding at high temperatures which might damage the devices and integrated circuits (ICs). Monolithic,

wafer-level, IC-compatible and low-temperature packaging technologies need to be developed to reduce cost and improve reliability. In order to address this challenge, a polymer-based air-gap MEMS packaging technology was investigated, which uses a sacrificial polymer, PPC, to create an air-gap by thermal decomposition around the MEMS device, enclosed with a polymeric overcoat, BCB. The air-gap technology relies on the sacrificial polymer, such as PPC, that provides a temporary place-holder for micro cavity creation. The selection of materials and processing conditions in air-gap technology are often limited by the decomposition temperature of PPC, implying the requirement to control or fine-tune PPC thermal stability. For that reason, the thermal stability enhancement of PPC by Cu(I) ions previously reported was investigated to further understand its mechanism.

In the electroless copper deposition study, we investigated an electroless copper deposition technique on an unclad epoxy laminate substrate, composed of a H₂SO₄ surface pretreatment, Sn/Ag nano-colloidal catalyst seeding, and immersion in a formaldehyde copper electroless bath. The lower cost and similar catalytic activity of Ag compared to Pd for formaldehyde oxidation makes Ag a rational catalyst choice for electroless copper deposition. It was found that the H₂SO₄ treatment cleaned the substrate of its impurities and provided the adhesion of the catalyst and electroless copper without increasing the surface roughness. Surface pretreatment with H₂SO₄ was unique in catalyst seeding, compared to other acid treatments including HCl and H₃PO₄. The sulfate content adsorbed on the epoxy laminate after H₂SO₄ treatment enabled Sn(II) sensitization by electrostatic attraction. The measured adhesion strength of deposited electroless copper layers indicated that even though H₂SO₄ treatment did not increase surface roughness,

adhesion was still dependent on the existing initial surface roughness of the substrate. X-ray photoelectron spectroscopy (XPS) results showed Sn(II) oxidation to Sn(IV) and Ag(I) reduction to Ag(0), so as to form a core-shell nano-colloidal catalyst with Ag(0) core and SnO₂ shell. It was plausible to consider some residual Sn(II) complexing with chloride ions to form SnCl₃⁻ on the outer surface of nano-colloids and preventing agglomeration. Sn/Ag nano-colloids were observed to well catalyze the electroless copper deposition reaction at a practical rate. The chemical adhesion was promoted by H₂SO₄ treatment rather than mechanical adhesion, and the use of Sn/Ag catalyst with H₂SO₄ surface treatment facilitated adherent, continuous and uniform electroless copper layers on epoxy laminates.

In the MEMS packaging study, a polymer-based air-gap MEMS packaging approach was investigated to reduce the cost, to simplify the packaging process and to analyze the polymeric residue. The idea was to achieve wide (~2.5x3.2 mm) and tall (10-20 μm) air-gaps to provide size-compatible packaging to MEMS devices, such as accelerometers and gyroscopes. The study provides a framework for size-compatible and clean air-gap formation by selecting the type of PPC, optimizing thermal treatment steps, identifying air-gap formation options, assessing air-gap formation performance, and analyzing the chemical composition of residue. BCB was identified as a PPC-compatible overcoat material providing excellent mechanical stability to air-gap structures. A kinetic comparison was done between PPC decomposition and BCB curing processes to determine the optimal thermal treatment recipe. It was found that the optimal treatment is a two-step heating process that includes a BCB curing at a lower temperature in the first step, and PPC decomposition at a higher temperature. Two air-gap formation processes,

RIE process (uses non-photosensitive PPC) and direct photopatterning process (uses photosensitive PPC), were proposed depending on how the PPC was patterned. Less residue and more reliable air-gap structures were obtained using the RIE process. The direct photopatterning process was simpler, however a greater amount of residue was observed due to photoacid generator (PAG), at least twice the residue in the RIE process. Comparison of two-layer PPC structures with both photosensitive and non-photosensitive PPC layers revealed that it was possible to obtain reliable air-gap structures only if the photosensitive PPC was the bottom layer. Nanoindentation measurements indicated that the mechanical strength of BCB caps was due to prestressing in BCB because of its tensile stress on silicon substrates. The polymer-based air-gaps provide a monolithic, low-cost, IC-compatible MEMS packaging option.

In the study of thermal stability of PPC, the thermal stability enhancement of PPC by Cu(I) ions was investigated to determine its mechanism. An increased thermal stability of PAG-containing PPC film was previously reported by our group (PAG was Rhodorsil-FABA, an iodonium-based PAG). XPS analysis done on the surface of PPC/PAG films prepared on Cu-sputtered substrates showed the presence of copper in Cu(I) oxidation state. The amount of copper obtained in the film was found to be similar to the amount of PAG (Rhodorsil-FABA). Cu(I) ion can be formed through oxidation of copper surface by dissolved oxygen in the PPC solution. The thermal stability of PPC/PAG films was studied for a number of iodonium and sulfonium-based PAGs. Every PAG/PPC film including iodonium-based PAGs showed thermal stability increase in the UV exposed cases. No thermal stability increase was observed using any sulfonium-based PAG. Based on these observations, a mechanism was postulated for the

observed thermal stability increase. A complexation-type of interaction between the iodonium in the cation of the PAG and Cu(I) disturbs acid creation mechanism of PAG. In the absence of acid, the PPC decomposition is not catalyzed, so the thermal stability of PPC increases on Cu surfaces.

Overall, the work presented in this dissertation endeavored to improve the chip-chip interconnection and MEMS packaging through metallization, processing and materials research. Ag-based catalysts can reduce cost, and non-roughening H₂SO₄ treatment can ensure fast and reliable signal propagation between chips through electroless copper layers on PWBs. MEMS packaging using polymer-based air-gaps can enable simpler packaging process and produce low-cost MEMS devices. Control of thermal decomposition temperature of PPC can allow a wider range of processes and applications.

CHAPTER 1

INTRODUCTION AND BACKGROUND

1.1 Project Motivation

Modern microelectronic technology is based on digital components such as integrated circuits (ICs), and on analog components such as microelectromechanical systems (MEMS). While the improvement in IC performance has been conventionally obtained by increasing transistor speed through transistor scaling and high frequency operation, the performance of ICs is currently limited by the delay in the interconnect lines connecting the ICs due to high loss (conductor loss and dielectric loss), rather than transistor speed. For MEMS, improvements have been focused more on the functionality and sensitivity of devices, while packaging of devices has become a bottleneck due to a wide range of device dimensions and packages being device-specific. The overarching goal of this thesis study is to improve IC interconnection and MEMS packaging through materials and processing research, technology development and reliability advancement. For IC interconnection improvement, we have investigated electroless copper deposition on epoxy laminate substrates that could be used for chip-chip interconnection. For MEMS packaging improvement, we have pursued an air gap-based MEMS packaging technique utilizing a sacrificial polymer, poly(propylene carbonate) (PPC) to achieve low-cost, monolithic, IC-compatible packaging option. For materials improvement, we have studied the thermal stability enhancement mechanism of PPC through Cu incorporation. The mechanism could allow control or fine-tune of thermal decomposition of PPC, and could widen PPC's processing and application space.

1.2 Background

1.2.1 Electroless Copper Deposition on PWBs for Chip-Chip Interconnection

The electroless deposition of copper is essential in fabricating epoxy-based substrates for microelectronic devices, such as printed wiring boards (PWB) and chip-chip interconnection on PWBs [1]. Figure 1.1 shows a schematic of copper traces on PWB used for interconnecting two ICs. The electroless copper layer can be utilized as a seed layer of electroplating (i.e. semi-additive process), or can be deposited to full metal thickness (i.e. fully additive process). The basic process steps in electroless deposition on PWB substrate are substrate surface pretreatment, catalyst seeding and electroless copper deposition, respectively. The major challenges facing electroless deposition for interconnect include cost, deposition time, reliability, electrical conductivity, and excess surface roughness [1-4]. The insulating surface onto which the deposit to be made needs to be first catalytically activated prior to electroless copper deposition. The conventional Pd-based catalyst is expensive, due to the high cost of Pd, ~\$750/oz [4]. Another concern is the reliability of the deposit if there is poor adhesion between the deposited electroless copper layer and the substrate [2, 3]. In addition, the electrical performance of copper interconnect is adversely affected by surface roughness which results in surface scattering of electrons, especially at high frequency [4-6]. At high frequency, the metal conductivity can be compromised because the conventional swell & etch process is based on an increase in the surface roughness in order to achieve acceptable adhesion through mechanical anchoring of the catalyst and the deposited metal [4, 7, 8]. Thus, there is a need for improved catalysts which can lower the cost (i.e. non-palladium catalysts), and

surface treatment methods which can avoid adding surface roughness (i.e. elimination of the swell & etch process).

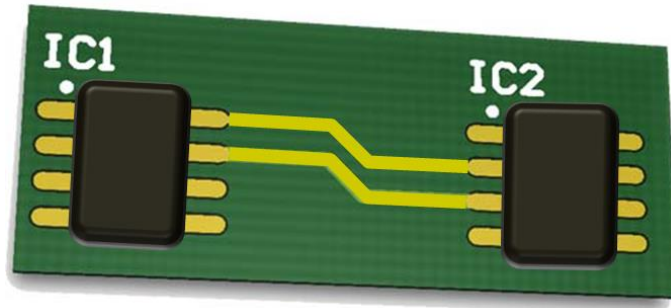
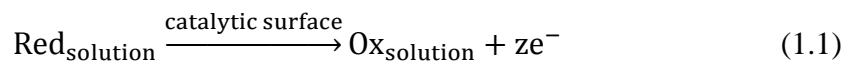


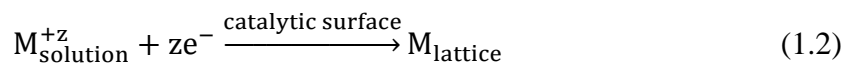
Figure 1.1 Chip-chip interconnection on PWB with copper traces

The electroless metal deposition involves the oxidation of a reducing agent (i.e. anodic partial reaction) and the reduction of metal ions (i.e. cathodic partial reaction) on the same catalytic surface. The electrons generated in the anodic partial reaction are utilized for reduction in the cathodic partial reaction. The general partial reactions and overall reaction can be shown as below:

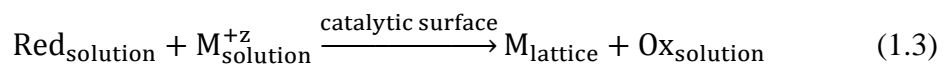
Anodic partial reaction:



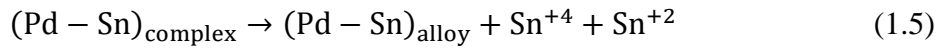
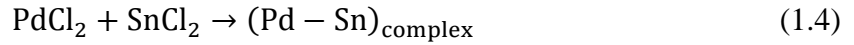
Cathodic partial reaction:



Overall reaction:



The catalytic surface needed for electroless deposition can be achieved by seeding the catalyst onto the substrate. The established catalyst for electroless copper deposition is the Sn/Pd nano-colloids. The Sn/Pd nano-colloids can be prepared in a dilute solution containing SnCl₂ and PdCl₂. The Sn(II) adsorbs onto the substrate surface by interacting with the oxygen-containing functionalities on the substrate, and facilitates reduction of Pd(II) to Pd(0). The general mechanism is given in Equation 1.4 and Equation 1.5 as [9]:



The Sn/Pd colloids are core-shell nano-structures with Pd-rich core and Sn-rich shell. Holderer et al. previously showed that the core is a Pd-Sn alloy with 60-70% Pd surrounded by a Sn shell [10]. The catalytic activity comes from the Pd content at the core. The Sn helps the colloid obtain spherical shape due to lower surface tension of Sn compared to Pd [11]. The Sn(IV) can be present in the oxidized to form SnO₂ shell around the core. The Sn(II) interacts with excess chloride ions and forms SnCl₃⁻ complexes on the shell which prevents agglomeration of nano-colloids [9, 10].

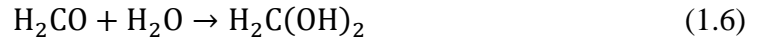
The reduction of copper ions in the cathodic partial reaction in Equation 1.2 can be readily achieved. The catalytic activity of the electroless copper deposition process is directly related to the oxidation of the reducing agent in the electroless bath, Equation 1.1, which is the rate-determining step in the process [3]. Both the anodic and cathodic

partial reactions have two main steps in which first an electroactive species is formed, and then there is electron transfer from or to the catalytic surface, as shown below.

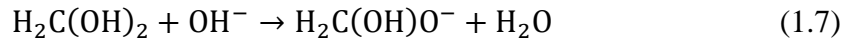
Anodic partial reaction

Formation of electroactive species

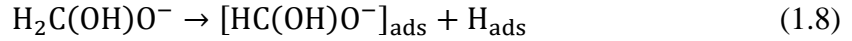
Hydrolysis of H₂CO (formaldehyde) and formation of methylene glycol



Dissociation of methylene glycol and formation of methylene glycolate anion



Dissociative adsorption of methylene glycolate anion



Charge transfer to catalytic surface



Hydrogen ionization on Pd or Pt



Hydrogen desorption on Cu



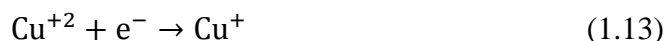
Cathodic partial reaction

Formation of electroactive species



Charge transfer from catalytic surface

First electron transfer (rate-determining step in charge transfer)



Second electron transfer



Overall reaction



The role of the surface catalyst is to facilitate the dissociative adsorption of the reducing agent (i.e. formaldehyde in this case) resulting in an adsorbed anion radical and adsorbed atomic hydrogen (Equation 1.8). The oxidation of adsorbed anion radical generates an electron (Equation 1.9), and the adsorbed atomic hydrogen recombines (Equation 1.11) or becomes ionized (Equation 1.10) [12]. The Sn/Pd nano-colloids are highly effective at catalyzing the oxidation of formaldehyde [3, 13]. The dominance of the Pd-based catalyst is due to its high catalytic activity for oxidation of a wide variety of reducing agents, and its stability and resistance to dissolution in the electroless bath [3, 13-15]. However, the high cost of Pd is an issue, and there is a need for low-cost catalyst.

In the seminal paper by Ohno et al., the catalytic activity of metallic Ag for formaldehyde oxidation was shown to be similar to Pd [12]. Vaskelis et al. showed that Ag-based catalysts for electroless copper deposition can be formed by reducing Ag(I) to Ag(0) by Sn(II) oxidation to Sn(IV), a process similar to the conventional Sn/Pd colloidal catalyst formation [15]. X-ray diffraction (XRD) measurements showed that the Sn/Ag nano-colloids had Ag in the metallic phase only, and Sn(IV) oxy-compounds, such as SnO₂, which was speculated to give the nano-colloid a “self-stabilizing” property. Fujiwara et al. followed a similar procedure to prepare Sn/Ag nano-colloids, and used XRD to confirm that the nano-colloids had Ag core and SnO₂ shell [16]. In addition, zeta potential measurements indicated the Ag/Sn nano-colloids were negatively charged because of an adsorbed Sn(IV) citrate layer on the nano-colloid surface providing the stability. Cationic surfactants were shown to adhere to the bare epoxy substrate and increase the density of adsorbed Ag nano-particles due to electrostatic interactions between the positively charged cationic surfactant on the substrate and the negatively charged Sn/Ag nano-colloid [17]. In both studies [15, 17], the catalytic activity of the Sn/Ag nano-colloids for electroless copper deposition was shown by cyclic voltammetry. Thus, Ag seems as a promising and inexpensive substitute for Pd in catalyzing electroless copper deposition.

The adhesion strength of electroless copper layers onto PWBs is an important issue in achieving reliable components. The adhesion strength of electroless copper to epoxy laminates (e.g. PWB) has been shown to have two contributions: mechanical adhesion and chemical adhesion [7, 8, 18-22]. Mechanical adhesion is based on the increase of the surface in surface area due to roughness from micropores, cavities and

asperities on the substrate surface [8, 19, 22]. Generally, the higher the surface roughness, the higher the adhesion strength. The higher surface roughness leads to greater contact area between the epoxy laminate substrate and the metal as well as the catalyst [7, 8, 18, 23, 24]. In addition, the presence of micropores and cavities creates mechanical interlocking between the epoxy laminate substrate and the catalyst/metal surface [8, 23, 25]. Depositing the electroless copper in the micropores and cavities causes the epoxy failures to be cohesive in nature rather than adhesive. That is, the epoxy surrounding the pores fails cohesively during adhesion testing, rather than simply pulling the copper metal off the epoxy surface. On the other hand, chemical adhesion is based on the chemical affinity between the substrate surface and the catalyst/deposited metal [7, 22, 26]. Chemical adhesion involves forming primary bonds, such as ionic or covalent bonds, at the epoxy/metal interface [4, 8, 19, 27]. The type and the abundance of chemical functionalities on the substrate surface play a major role in the chemical adhesion [8, 24, 28]. Chemical adhesion can be characterized by obtaining the density of functional groups on the surface and the oxygen-to-carbon ratio using X-ray photoelectron spectroscopy (XPS). Mechanical adhesion can be characterized by surface roughness measurements using atomic force microscopy (AFM) [18]. While both mechanisms contribute to total adhesion strength of the deposited metal, the mechanical adhesion is usually greater than the chemical adhesion [4, 8, 23, 24, 29].

Surface pretreatment methods play an important role in the adhesion of electroless copper to insulating surfaces, such as PWBs. The surface pretreatment method cleans the substrate surface of impurities that can hinder the electroless deposition process, and mechanically and/or chemically conditions the surface for attachment of the catalyst [25,

28]. A number of surface pretreatments have been used to improve the adhesion of electroless copper to epoxy laminate substrates including wet-chemical treatments [7, 8, 25, 26, 29], surface modification through synthesis [21, 22, 30-32], plasma treatments [24, 28], sonochemical treatments [33, 34], photocatalytic reaction [35], and treatment with surfactants [17]. Two general categories of surface pretreatment are wet-chemical treatment and plasma treatment [7, 18, 24, 28, 36]. Wet-chemical treatment is usually easy to implement and does not require expensive vacuum tools. The most common wet-chemical pretreatment for epoxy is the swell-and-etch process [4, 18, 25]. The swell-and-etch process is based on increasing the surface roughness leading to high adhesion strength of the electrolessly deposited metal [7, 8, 18, 22, 25]. The processes taking place during swell-and-etch application are shown in Figure 1.2 [8].

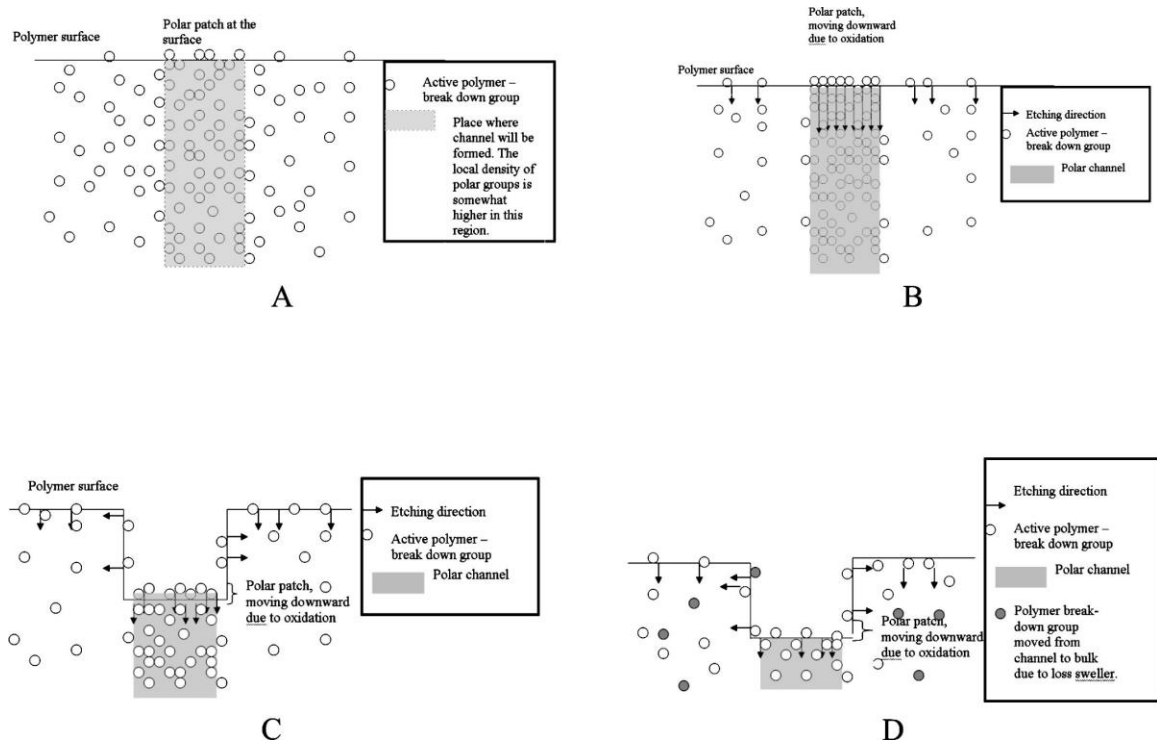


Figure 1.2 The processes taking place during swell-and-etch application [8]

The epoxy laminate has polar groups, such as primary and secondary alcohols and ethers, which are susceptible to oxidation (Figure 1.2A) [7, 8, 22]. During swelling, the solvent (e.g. 2-(2-butoxyethoxy)ethanol) diffuses into the near-surface free volume of the epoxy causing swelling. The polymer chains are distorted in a way that exposes the polar groups to the epoxy surface, and creates channels into the epoxy which are lined with polar groups (Figure 1.2B) [7, 8, 18]. During etching, an oxidizer (e.g. alkaline KMnO_4) oxidizes the polar groups and forms functionalities such as carboxylic acid, ketones, and aromatic alcohols, and breaks ether bonds in the epoxy, creating micropores and cavities (Figure 1.2C) [7, 22, 37]. Although the effect of the oxidizer is isotropic in nature, the heterogeneous distribution of polar groups on the epoxy surface and within the near-surface region leads to different etch rates at the various sites. The etch rate are higher in regions where there is a high concentration of polar groups which leads to an increase in surface roughness (Figure 1.2D) [36]. In the swell-and-etch process, the physical anchoring contribution to the adhesion strength due to the high surface roughness is about 5 to 10 times greater than the chemical contribution to adhesion coming from the interaction of the catalyst and deposited copper with the oxidized functionalities on the epoxy laminate [25].

A second wet-chemical surface treatment method is chromic acid etching, which is less commonly used. Chromic acid etching is also based on an increase in surface roughness created by chemical etching with a strong oxidizer (e.g. $\text{K}_2\text{Cr}_2\text{O}_7$ in H_2SO_4) [4, 7, 38, 39]. However, the increase in the surface roughness of an epoxy laminate is less than that for the swell-and-etch method [7]. In addition, the hexavalent chromium is toxic, carcinogenic and corrosive [40].

The high frequency signal degradation that occurs in the roughened electroless copper layer is an important issue for electronic devices. At high frequency, high surface roughness degrades the electrical signal due to electron scattering, especially when the surface roughness is comparable to the “skin depth” of the metal at the operating frequency [4-6]. The skin effect is the phenomenon that the alternating current (AC) density tends to be largest at the outer surface of the conductor than the interior of the conductor at high frequencies. This occurs due to opposing eddy currents due to AC magnetic field which cancel the current flow in the interior of the conductor. So that, the electric current flows mainly near the surface of the conductor rather than through bulk of the conductor. The skin depth is defined as the depth below the surface at which the current density drops to $1/e$ (~37%) of the current density at the surface. The skin depth can be calculated for any material at a given frequency using Equation 1.16:

$$\delta = 10^9 \sqrt{\frac{\rho}{\pi f \mu_0 \mu_r}} \quad (1.16)$$

where δ is the skin depth in nanometers, ρ is the resistivity of the conductor in $\Omega\cdot\text{m}$, f is the frequency in Hz, μ_0 is the magnetic permeability of free space (1.26×10^{-6} H/m), and μ_r is the relative magnetic permeability of the conductor. The signal loss in the conductor increases as the operating frequencies goes up in each new technology node due to increased resistance of the conductors. The resistance of the conductors increases due to decreased conduction area, as shown in Equation 1.17:

$$R = \rho \frac{l}{A} \quad (1.17)$$

where R is the resistance in Ω , ρ is the resistivity of the conductor in $\Omega\text{-m}$, l is the length in m , and A is the cross-sectional area of the conductor in m^2 .

The surface roughness as a result of the conventional swell-and-etch process leads to high conductor losses in electroless copper on epoxy laminate substrates, and this becomes a bottleneck for chip-chip interconnects at high operating frequencies. In order to mitigate the signal loss, one approach is to use an electroless copper surface treatment that promotes chemical adhesion without increasing the surface roughness. The surface treatment method can utilize the already present surface roughness of the epoxy laminate to provide some mechanical adhesion anchoring. The chemical effect of the surface treatment method can modify the type and abundance of certain chemical functionalities so as to increase the interfacial forces between the substrate, catalyst, and electroless copper. In a previous study, it was shown that a combined oxygen plasma treatment and hot sulfuric acid treatment produced adherent electroless layers deposited with a Sn/Ag catalysts on polyhedral oligomeric silsesquioxane (POSS) coated, smooth FR-4 boards [4]. The role of oxygen plasma was to remove the organic component of the POSS. It is possible that the hot H_2SO_4 treatment increased the chemical adhesion on the smooth surface. Based on this result, the role of a H_2SO_4 treatment for epoxy surfaces can be investigated as an alternative surface treatment to the swell-and-etch method in this study.

1.2.2 Polymer-based Air-gap MEMS Packaging

Packaging of microelectromechanical systems (MEMS) is essential for providing physical protection and electrical connectivity to the MEMS device. MEMS packaging is a challenging technology and an important part of the final device cost and performance

[41]. MEMS packaging can compromise up to 60-80% of the total MEMS product cost [42]. MEMS packaging is an emerging sector estimated to grow ~2.5x faster than the IC packaging sector, because of ever-increasing penetration of MEMS technology into mobile and consumer applications in recent years, as shown in Figure 1.3 [41]. Despite its importance, many challenges remain in MEMS packaging [43].

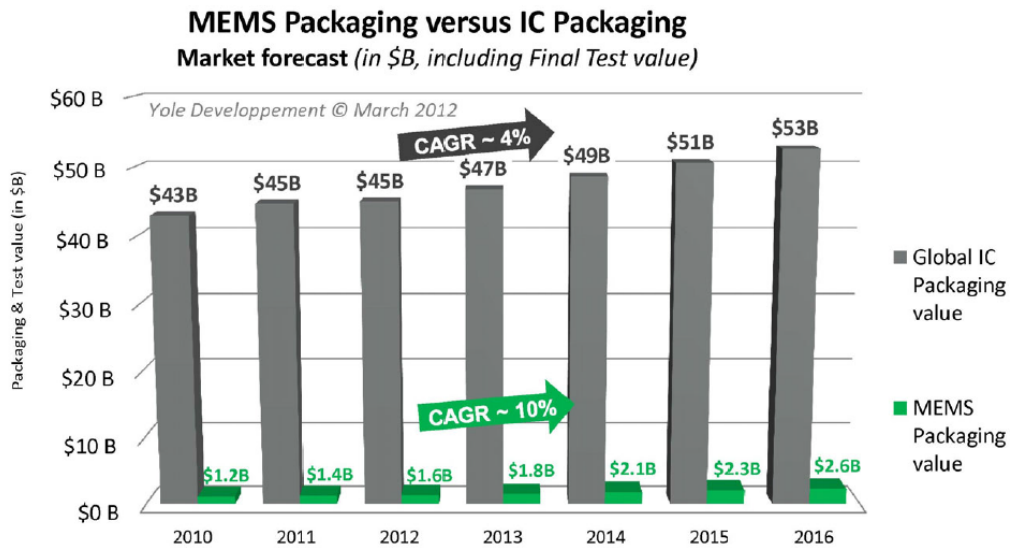


Figure 1.3 Comparison of growth rates in MEMS packaging sector versus IC packaging sector [41]. CAGR stands for “compound annual growth rate”, and it is a measure of growth based on the geometric progression ratio that provides a constant rate of return over the time period [44].

Wafer-level packaging is an emerging approach that allows testing and packaging of multiple MEMS die at the wafer-level, thereby decreasing the test and package cost per die [45]. Conventional wafer-level packaging often involves bonding a MEMS wafer to a silicon or glass capping wafer by direct bonding (anodic bonding or fusion bonding) or by use of intermediate layers (glass frit, soldering, eutectic bonding, or epoxy-based polymers) [45-47]. The current industrial standard MEMS packaging technique of wafer capping is shown in Figure 1.4 [47].

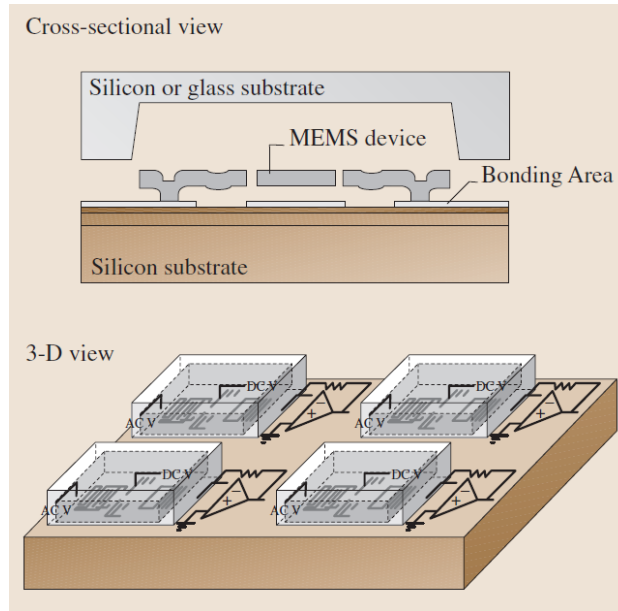


Figure 1.4 Cross-sectional and 3-D view of MEMS packaging using wafer capping [47]

These conventional processes require careful alignment of the capping and MEMS wafer, and high temperature processes that might cause damage to the MEMS device or the package (e.g. anodic bonding at $\sim 400^{\circ}\text{C}$) [46]. A monolithic and low temperature wafer-level MEMS packaging process can decrease the packaging cost and ensure reliability. For such a MEMS packaging process, size-compatibility is an important aspect, especially for devices that require large area, e.g. MEMS accelerometers or gyroscopes [41, 48]. The MEMS packaging process also needs to provide clean MEMS surfaces after packaging to prevent dampening effects or oxidation which might interfere with the device performance and reliability. Therefore, there is a clear need for low-cost, clean, IC-compatible, wafer-level packaging solutions.

Polymer-based air-gap packaging is an approach that can be performed at the wafer-level [48-50]. The process flow for the formation of a polymer-based air-gap can be summarized as follows. First, a sacrificial polymer film is coated and patterned on the

MEMS device. This sacrificial polymer film encases the MEMS device and serves as a temporary place holder. The sacrificial polymer can be a polycarbonate (e.g. poly(propylene carbonate) (PPC)) that thermally decomposes at low temperatures, 180°C to 250°C [51, 52]. Two air-gap formation processes can be identified depending on how the sacrificial polymer is patterned, namely (i) reactive ion etching (RIE), and (ii) direct photopatterning process. In the RIE process, a non-photosensitive sacrificial polymer film is cast from a solution containing only the sacrificial polymer (e.g. PPC) dissolved in the solvent (e.g. gamma-butyrolactone (GBL)). The sacrificial polymer film is patterned by anisotropic RIE in an oxygen-rich plasma. A pattern-transfer material with high selectivity, such as silicon dioxide, can first be patterned with photoresist [50] or the PPC can be patterned with a thin photodefinable polymer [49]. In the direct photopatterning process, the sacrificial polymer is made photosensitive and can be patterned directly by UV-exposure through a photomask followed by dry-development. The dry-development is possible since the photoacid generated by UV exposure catalyzes the PPC decomposition, thus lowering the PPC decomposition temperature [51]. After the sacrificial polymer has been patterned, an overcoat polymer is conformally coated on and around the sacrificial polymer. The overcoat material can be a photodefinable dielectric with adequate mechanical strength, such as Avatrel or epoxy-cyclohexyl polyhedral oligomeric silsesquioxane (POSS) [48-50]. Finally, the overcoat polymer is cured and the sacrificial polymer is thermally decomposed. The low molecular weight decomposition products, such as CO₂ and acetone, permeate through (dissolve into, diffuse through and evolve out of) the overcoat polymer [48-50]. This leaves the MEMS device in an encased air space and encapsulated in a protective overcoat envelope. The

processing temperature for polymer-based MEMS packaging is low ($<250^{\circ}\text{C}$), and the process is monolithic, i.e. bonding of a capping wafer is not required. The mechanical strength and hermeticity of the overcoat can be increased if a thin metal film is deposited (e.g. 1 to 3 μm of Al or Cu) on the overcoat polymer [48, 49]. Vacuum hermeticity in the package can be obtained by first thermally decomposing the sacrificial polymer in a vacuum chamber (evaporation or sputtering tool) followed by deposition of a thin metal film while the sample is still under vacuum.

Various polymer-based air-gap MEMS packaging studies have been reported in the literature using both the RIE process and the direct photopatterning process [48-50]. Previously, Joseph et al. used a polycarbonate-based sacrificial polymer (Unity 2303) and a SiO_2 /Avatrel 2195 overcoat to package microresonators with air-gaps (~ 10 μm in height, $\sim 100 \times 150$ μm in size) [50]. The non-photosensitive sacrificial polymer was found to leave no visible residue [50, 53]. However, the RIE patterning process was complex due to the use of a temporary, thin SiO_2 pattern-transfer layer. Using the direct photopatterning process, a minimal decrease in resonant frequencies (1.3% decrease in average) and a small degradation in quality factor values ($\sim 20\%$) were observed after packaging. The lower quality factor was due to residue left on resonators after PPC decomposition. The residual fluorine content detected in the residue by energy-dispersive X-ray spectroscopy (EDS) analysis indicated that the photoacid generator (PAG) contributed to the residue [53]. The non-photosensitive PPC can also contribute to the residue especially if the PPC contained impurities, such as polyether, catalyst particles, or residual solvent, from the PPC synthesis [53-55]. Monajemi et al. packaged resonators, with similar dimensions as in [50], in addition to accelerometers with air-gaps (1.5×1.8

mm in the x-y direction, 1 to 100 μm in height by spin-coating or few millimeters by dispensing) using a photodefinable polycarbonate-based sacrificial polymer (Unity 2000P) and Avatrel 2195 overcoat [48]. However, the residue contribution was not discussed, and the packaging process required a very thick ($\sim 120 \mu\text{m}$) Avatrel 2195 overcoat layer. In order to minimize the residue, Saha et al. used a non-photosensitive PPC sacrificial polymer patterned by a thin layer of POSS and overcoated by a thick POSS layer [49]. The air-gap dimensions were 20 to 200 μm in width and 200 to 600 μm in length with a 3.5 μm in height. Also, air-gap structures of 10 to 18 μm tall and 1 to 2 mm in diameter were obtained with some degree of sagging of the overcoat (i.e. 60% sagging) which occurred during the compression epoxy-molding process. However, POSS is a sticky material that is difficult to work with, and the pattern generation using spray-developing of isopropanol is challenging.

The amount of PPC residue left by the photosensitive PPC was previously lowered by using a hybrid PPC film which had both photosensitive and non-photosensitive PPC layers [56]. Photodecomposition of the PPC occurred as long as the photoacid concentration was above a minimum threshold in one region of the PPC film. As decomposition occurred, the acid front moved through the PPC film causing non-acid layers to decompose. Chun et al. achieved 600 μm wide and 32.7 μm high air-gap channels using a photosensitive PPC layer (6.3 μm) on top of a non-photosensitive PPC layer (26.4 μm) with an Avatrel 8000P overcoat [56].

The requirements for improving the polymer-based air-gap MEMS packaging approach can be summarized as (i) simplification of the air-gap formation processes, (ii) minimization of the amount of residue to ensure unchanged device performance, and (iii)

formation of large and reliable air-gap sizes to accommodate different MEMS devices. This requires a closer look at the sacrificial and overcoat polymers, residues, air-gap structure architectures and optimization of the processes.

1.2.3 Thermal Stability Enhancement of Poly(propylene carbonate)

Sacrificial polymers have been used in the microfabrication of a variety of microelectromechanical (MEMS) and microfluidic devices. The basic function of the sacrificial polymer is to provide a space holder for micro-cavity creation [57, 58]. Recently, sacrificial polymers have been used to fabricate air-gaps as an ultra low-k insulator for electronic devices and packages [58-67]. Air-clad electrical connections provide a low-loss transmission media for electrical signals, particularly at high frequencies where both the real and imaginary parts of the dielectric constant are important [60-62]. The decomposition temperature of the sacrificial polymer is critically important in the process sequence since it must be compatible with the substrate, encapsulating material(s), and subsequent processing steps [52]. The selection of materials and methods of fabrication are thus limited by the chosen sacrificial polymer. For that reason, there is a clear need to control or fine-tune the decomposition temperature of the sacrificial polymer to accommodate a wide range of materials and processes.

Polynorbornenes [58, 63, 68-71] and polycarbonates [50, 51, 61, 71-75] have been widely used as sacrificial polymers. Polycarbonates generally have a lower decomposition temperature than polynorbornenes and can be used with a wide variety of permanent dielectrics, however, their low glass transition temperature (T_g) can lead to mechanical problems during fabrication. The decomposition of polycarbonates has been

catalyzed by photoacid generators (PAGs) making them photopatternable [52]. Poly(propylene carbonate) (PPC) can be obtained by the copolymerization of carbon dioxide and propylene oxide using organometallic catalysts [76]. PPC has a modest decomposition temperature, ranging from 100°C to 300°C depending on its molecular weight. There are two mechanisms for PPC decomposition: (i) chain unzipping from the end group, and (ii) random chain scission [77-82]. Chain unzipping reaction occurs at lower temperatures compared to chain scission because it has a lower activation energy compared to chain scission [77-79, 81, 82]. In most studies, chain unzipping is shown to be the primary decomposition mechanism [77-79, 81, 83, 84]. It is postulated that chain unzipping occurs either by (i) alkoxide activation where a relatively strong nucleophile at the chain end attacks the carbonyl atom, or (ii) carbonate activation where a relatively weak nucleophile attacks the electrophilic carbon atom [82, 83, 85]. It is also proposed that when the temperature is ramped from low to high, the PPC decomposition takes place in three stages: (i) at lower temperature, chain unzipping is the primary degradation mechanism, (ii) at modest temperatures, decomposition takes place by competing multi-step reactions, and (iii) at the higher temperatures, chain scission dominates the decomposition [86].

There are numerous studies in the literature focusing on increasing the thermal stability of PPC through the blending PPC with fillers [80, 87-95], polymerizing with additional backbone components [96-102], adding cross-linking [103, 104], hydrogen-bonding [94, 95, 105], end-capping [77, 79, 86, 99], and metal ion coordination [74, 78]. Among these, end-capping is the more efficient technique. It also provides simple processing and lower cost. Basically, the nucleophilic hydroxyl groups at the PPC ends

are replaced with less reactive groups inhibiting the hydroxyl initiated chain unzipping reaction. Taking the temperature at the point where 5% weight loss occurs as the characteristic temperature for decomposition (i.e. 5 wt% loss point), Dixon et al. reported ca. 20°C increase in thermal stability (at 2.5°C/min heating rate) using acetyl chloride/pyridine reagent as the end-capping agent [77]. Peng et al. observed improved thermal stability by 27°C to 42°C (at 5 wt% loss point using 10°C/min heating rate) by end-capping PPC with phosphorous oxychloride, acetic anhydride, ethyl silicate, benzoyl chloride, and maleic anhydride reagents [79]. Yao et al. showed a thermal stability increase of ca. 140°C (at 5 wt% loss using 15°C/min heating rate) where PPC was end-capped with maleic anhydride with weight fractions between 0.5 wt% and 5 wt% through melt blending [86].

Improving the thermal stability of PPC by metal ion coordination is another technique in which chain unzipping is inhibited through coordination between a metal ion and oxygen in the carbonate groups. Yu et al. showed that the thermal stability of PPC is significantly enhanced with calcium stearate [78]. It was speculated that Ca cations coordinate with oxygen in the carbonate groups throughout the PPC backbone leading to inhibition of the chain unzipping reaction. Recently, Spencer et al. reported ca. 50°C increase in thermal stability of PPC (at 50 wt% loss point using 0.5°C/min heating rate) by copper ion incorporation [74]. The substrate was a copper-sputtered silicon wafer where the native oxide on the copper surface was removed before solvent casting the PPC film. The PPC was cast from a solution containing γ -butyrolactone (GBL) as the solvent and Rhodorsil-FABA as the photoacid generator (PAG). Rhodorsil-FABA is an iodonium-based PAG with a borate anion, as shown in Table 1. The PAG can be

activated photolitically (i.e. UV radiation) or thermally. Upon activation, the PAG cation produces two radicals which react either with the hydrocarbon portion of the cation, polymer, or residual solvent to create a proton in order to catalyze the decomposition of the PPC [53].

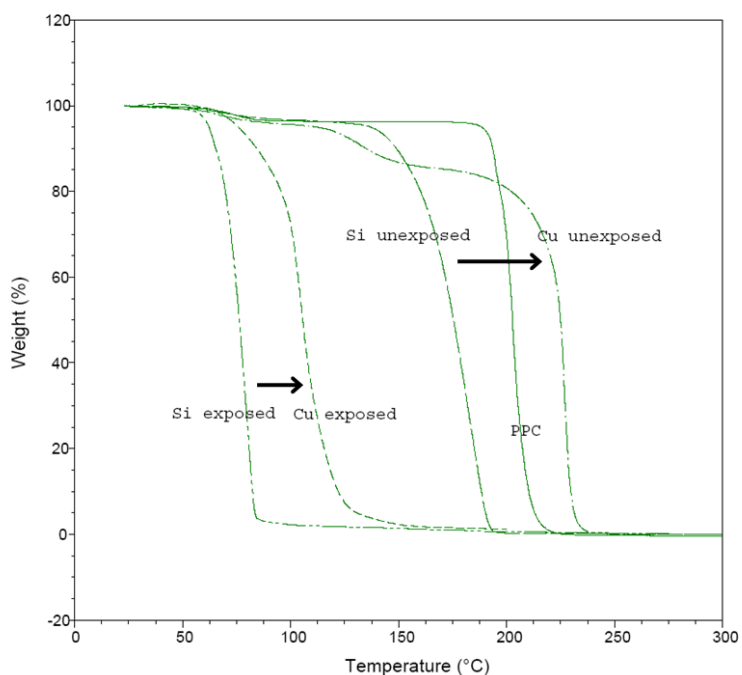


Figure 1.5 Dynamic TGA plots for PPC films in GBL cast on a copper surface and cast on silicon with and without UV exposure compared with decomposition of neat PPC without UV exposure [74]

Spencer et al. [74] observed an increase in the thermal stability when the PPC/PAG mixture was coated on copper for both the UV exposed and unexposed cases. As seen in Figure 1.5, the samples prepared on copper (cases labeled “Cu exposed” and “Cu unexposed”) both decompose at a higher temperatures relative to the samples prepared on silicon (cases labeled “Si exposed” and “Si unexposed”). The decomposition temperature of the unexposed film on copper (copper unexposed case) was even higher than the decomposition temperature of neat PPC. Thus, it is clear that observed thermal

stability effect is directly related to the presence of the copper surface. Even though copper incorporation is obviously responsible for thermal stability, the cause of the shift in decomposition temperature was only speculated. It was shown that only trace amounts of copper are needed, estimated to be one copper ion per 100 PPC monomer units (or carbonyl oxygens). The authors discussed that the copper may hinder the unzipping reaction by interacting with the PPC chain ends, so that the decomposition of PPC becomes suppressed. However, there is a scarcity of copper available for interaction with polymer. In addition, there may be no specificity of chain ends to interact with copper, i.e. it is not guaranteed that the copper will interact with PPC chain end rather than interacting with the PPC backbone. The specificity of the interaction between copper and PPC chain end was not discussed in [74]. Thus, a better explanation for thermal stability enhancement of PPC is needed.

1.3 Research Objectives

The overarching goal of this study is to improve chip-chip interconnection and MEMS packaging through materials, processing and technology development. This goal will be pursued in three subtopics, as presented above. In electroless copper deposition study, the objective is to obtain adherent electroless deposition on PWB substrates by replacing the expensive Pd-based catalysts with a cheap and equally active Ag-based catalyst, and by finding a non-roughening surface treatment method that will not increase the conductor loss. In the MEMS packaging study, the objective is to develop a polymer-based air-gap packaging approach, identify air-gap creation processes and assess the polymeric residue in order to obtain size-compatible and clean air-gaps. In the thermal stability study of PPC, the objective is to understand the thermal stability enhancement mechanism of PPC by Cu(I) interaction.

CHAPTER 2

EXPERIMENTAL

In this section, a detailed description of materials, processing, and analysis techniques used in this dissertation is presented. This chapter is organized to cover the experimental methods for each study separately for clarity.

2.1 Electroless Copper Deposition on PWBs for Chip-Chip Interconnection

2.1.1 Materials

The PWBs used in this study was ISOLA 185HR unclad laminate PWBs supplied from Isola Global [106]. ISOLA 185HR is a multifunctional epoxy novolac laminate, obtained from the reaction of novolac (i.e. phenol formaldehyde) resin with epoxy [107].

2.1.2 Processing

2.1.2.1 Surface Pretreatment Methods

The standard surface treatment method used here was a hot H_2SO_4 treatment. The substrates were immersed in 12 M H_2SO_4 at 95°C for 30 min prior to Sn/Ag catalyst seeding. Several surface treatment methods were investigated for comparison with hot H_2SO_4 pretreatment. These methods involve surface pretreatment using hot H_3PO_4 or HCl solutions. For consistency, the concentrations of H_3PO_4 and HCl were the same as that of H_2SO_4 , 12 M. The duration of the surface pretreatment was 30 min in each acid solution. The temperature for the H_3PO_4 treatment was kept constant at 95°C , whereas the temperature for HCl was kept constant at its boiling point at 48°C . For comparison of

introduced surface roughness, surface treatment using swell-and-etch method was also performed. The swelling step of the swell-and-etch process consisted of a 1:1 volume mixture of 2-(2-butoxyethoxy)ethanol and deionized (DI) water. The etching bath consisted of 55 g/L KMnO_4 and 1.2 M NaOH in DI water. First, a sample was washed under DI water followed by swelling for 7.5 minutes at 80°C . After swelling, the sample was rinsed with DI water, and then placed in the etching bath for 10 minutes at 80°C [7].

2.1.2.2 Electroless Copper Deposition Procedure

The default electroless copper deposition method involved the substrate pretreatment with hot H_2SO_4 , as explained above. The substrate pretreatment was followed by the Sn/Ag catalyst seeding and electroless Cu deposition. The electroless copper activation and plating process involved immersion in three sequential baths: (i) tin sensitization bath, (ii) silver activation bath, and (iii) electroless copper deposition bath, as outlined previously in [4, 108]. The tin sensitization bath consisted of 1.4 g $\text{SnCl}_2 \cdot 2\text{H}_2\text{O}$, 2 mL HCl and 200 mL deionized (DI) H_2O . The tin sensitization was performed at 25°C for 30 min. The samples were then rinsed thoroughly with DI H_2O . The samples were then immersed in the silver activation bath which consisted of 0.75 g AgNO_3 , 10 g $(\text{NH}_4)_2\text{SO}_4$, 20 mL NH_4OH , and 180 mL H_2O . The silver activation was done at 25°C for 1 min, and the samples were then rinsed thoroughly with DI H_2O . The electroless copper deposition bath was composed of 0.75 g $\text{CuSO}_4 \cdot 5\text{H}_2\text{O}$ as the copper source, 1.89 g ethylenediaminetetraacetic acid (EDTA) as the complexing agent, 2.58 g potassium hydroxide for adjusting the pH, 0.2 mL Triton X-100 as the surfactant, 0.58 g paraformaldehyde $(\text{CH}_2\text{O})_n$ as the reducing agent and 200 mL DI H_2O . It is important that the components were added into the DI water in the order listed and given sufficient

time to dissolve before the next component was added. The pH of the electroplating bath was measured to be 12.5. The electroless copper deposition was performed at 55°C for different deposition times. The deposition time was longer than the 3 min induction period of the electroless copper [109].

2.1.3 Analysis Techniques

2.1.3.1 Measurement of Electroless Copper Deposition Rate

The deposition rate of the electroless copper was obtained gravimetrically using a balance (Mettler AE200). Multiple samples were simultaneously processed in the sulfuric acid, tin sensitization, silver activation, and electroless copper baths. The samples for each electroless deposition time were taken out of the electroless copper bath, rinsed and blow-dried with dry N₂. The mass of each sample after electroless copper deposition was measured. The electroless copper was then chemically stripped off the sample by immersion in concentrated HNO₃ for 3 to 5 s. Afterwards, the sample was rinsed with DI water, dried with nitrogen gas, and its mass was measured again. The difference between the two mass readings gave the amount of the electroless copper deposited. The superficial area of the each sample was used to calculate the deposition rate per unit area using the bulk density of copper, 8.96 g/cm³.

2.1.3.2 Measurement of Adhesion Strength of Electrolessly Deposited Copper on PWB

The adhesion strength of the electrolessly deposited copper layer was evaluated by performing qualitative tape tests and quantitative pull tests. The thickness of the electrolessly deposited copper was increased in order to perform the quantitative adhesion strength tests. Copper was electroplated on the electroless copper using an

acidic copper electroplating bath [107]. The recipe consisted of 200 g $\text{CuSO}_4 \cdot 5\text{H}_2\text{O}$, 60 g H_2SO_4 , 0.5 g polyethylene glycol (PEG), and 0.14 g CuCl in 1 L DI water. Copper was plated at a current density of 25 mA/cm^2 at room temperature for 50 to 60 min. The 90° peel test was then performed to quantify the adhesion strength of the electroless copper layer using an Instron load frame tool (Model 5842) following the ASTM B 533-85 standard. The test involved vertically peeling a 3-mm wide copper strip from the substrate surface. The pull force was measured as a function of time. The average pull force was divided by the width of the copper strip width to give the peel strength in N/mm. At least three samples were run and acquired data were averaged to obtain each data point. The error range in 95% confidence interval for each data point was calculated.

2.1.3.3 Surface Roughness Determination

The topography of the samples was investigated using a Veeco Dimension 3100 atomic force microscopy (AFM) with a Series 15 MikroMash single cantilever probe. A square area of $50 \times 50 \mu\text{m}$ was scanned for every measurement. The surface roughness measurements were done in tapping mode with a tip velocity of $25 \mu\text{m/s}$. The resolution of the scans was either 256 samples/line or 768 samples/line. In all measurements, the resonant frequency of the tip was constant at ca. 318.694 kHz, and the same proportional-integral control and amplitude set point parameters were used. The average (R_a) and root-mean-square (R_q) roughness values were extracted from the acquired AFM images using NanoScope Analysis v1.40 software. No smoothing of the images or data was applied. At least two measurements were performed for each sample, and the surface roughness was reported for the one with the larger surface roughness.

A second, quick turn-around surface topology characterization was performed in some experiments using a Dektak 3 profilometer. Individual line scans were obtained, and the average surface roughness was evaluated. The PWB surface was sometimes polished using a Buehler polisher with short felt pads (Carbimet 600/P1200) in order to decrease the surface roughness of the as-received PWBs without changing their materials. After polishing, the samples were rinsed with DI water, and blow-dried with N₂. Three 1-mm Dektak line scans were obtained and averaged (i.e. average R_a and R_q values) for each sample. The samples then underwent surface pretreatment with H₂SO₄, catalyst seeding (tin sensitization and silver activation), and electroless copper deposition.

2.1.3.4 Chemical Characterization of Surfaces

The surface characterization of the samples was performed using a Thermo K-alpha X-ray photoelectron spectrometer (XPS). The energy step size of the survey scans was either 0.5 eV or 1 eV, whereas the energy step size for the elemental scans was 0.1 eV. The X-ray spot size was 200 μm in diameter for all measurements. A low-voltage electron flood gun was kept on during measurements for charge compensation. In order to reduce noise in the XPS signals, each point was investigated twice for the survey scan, and five times for the elemental scan. The surface scans were performed without argon ion etching, whereas the atomic concentrations in the depth profiles were obtained using an argon ion gun with a raster size of 0.3 mm. The argon ion gun was operated with an ion energy of 3000 eV, and the current was adjusted to give an etch rate of 16.36 nm/s, as referenced to tantalum etching. The acquired XPS survey scans were analyzed using Avantage software [110]. The C1s signal was used as a reference signal for charge-shifting the acquired survey spectra so that the C1s peak position would be at 285.0 eV.

In addition to the survey scans, high resolution elemental XPS scans were also performed. The elemental scans were used to confirm the presence of elements detected in survey scan results. The elemental scans were also used for detailed chemical characterization via deconvolution of individual peaks, such as the C1s peaks, into several peaks for that element corresponding to different oxidation states. The fractional composition for each oxidation state obtained from the deconvoluted spectra corresponds to their relative molar concentration on the substrate. The deconvolution and analysis of C1s signals were done using CasaXPS software [111]. The functional groups associated with the C1s scans were hydrocarbon functionalities C-C and C-H with reference peak position of 285.0 eV, alcohol and ether functionalities C-O-H and C-O-C with reference peak position of 286.5 eV, carbonyl functionality C=O with reference peak position of 288.0 eV, acid and ester functionalities O-C=O with reference peak position of 289 eV, and carbonate functionality O-C(=O)-O with reference peak position of 290.3 eV. The peak position tolerances were accepted as ± 0.2 eV for all functional groups in the C1s spectra [112]. The full width at half maximum (fwhm) values for all functional groups were constrained between 0.85 eV and 1.7 eV. The built-in simplex algorithm in CasaXPS was used to optimize the fitting of functional group peaks to the overall C1s peak with the objective of minimizing the residual. Monte-Carlo simulation was performed to obtain the standard deviations in the calculated peak areas.

2.2 Polymer-based Air-gap MEMS Packaging

2.2.1 Materials

The PPC used in this study was generously supplied from two sources. PPC with a molecular weight of 160,000 g/mol (Novomer 160K) was supplied from Novomer, Inc.

(Ithaca, NY), and PPC with a molecular weight of 141,000 g/mol (QPAC 40 141K) was supplied by Empower Materials (New Castle, DE).

The photoacid generator, Rhodorsil-FABA, was supplied from Solvay Inc. Rhodorsil-FABA is a diphenyliodonium PAG which creates a strong acid upon UV exposure (248 nm) or at high temperature, ca. 180°C [53, 54, 113].

Photodefinable BCB (Cyclotene 4026-46) was supplied from Dow Chemical Co. (Midland, MI) and used as-received. BCB undergoes cross-linking above 160°C [114-117]. It has a high glass transition temperature (>350°C) and low moisture uptake (0.14% at 23°C and 84% relative humidity) [114]. Its coefficient of thermal expansion (CTE) is 52 ppm/K [114]. The spin-coating thickness range for as-received BCB is between 7.3 and 14.2 μm for spin-speeds between 1500 rpm and 5000 rpm [118]. For thinner coating (e.g. pattern-transfer layer in the RIE process), BCB was diluted with mesitylene in a ratio of 1:4 mesitylene:BCB (referred as “diluted BCB” in this study).

The substrates were <100> p-type silicon wafers supplied from University Wafers. The silicon substrates used without prior cleaning. In order to remove dust, the substrates were blown with dry N₂ gas before PPC application.

2.2.2 Processing

2.2.2.1 Purification of PPC

A precipitation-based purification procedure was employed to remove impurities in the as-received PPC, such as particles. The PPC was dissolved in acetone to achieve a 10-15 wt% solution, followed by vacuum filtering using a fine filtering paper and precipitation with isopropanol. The precipitate was then washed with excess isopropanol. The procedure was repeated three times followed by vacuum drying at 100°C overnight.

The purified PPC was dissolved in gamma-butyrolactone (GBL) to achieve 25 to 35 wt% PPC solution. The solution was left to mix on a roller overnight at room temperature.

2.2.2.2 Preparation of Photosensitive PPC solution

In cases where a photosensitive PPC solution was required, the PPC solution was made photosensitive by adding a photoacid generator (PAG), Rhodorsil-FABA (Solvay Inc.), and mixing overnight on the roller at room temperature. The concentration of Rhodorsil-FABA was adjusted to be 3 wt% of the PPC in the solution.

2.2.2.3 Air-gap Formation Processes

Two air-gap formation procedures were used in this study, as shown in Figure 2.1, i.e. the RIE process (Figure 2.1a) and the direct photopatterning process (Figure 2.1b). The RIE process consisted of first coating <100> p-type silicon wafers without additional cleaning (Figure 2.1a step (i)) with a 25 to 35 wt% non-photosensitive PPC solution by spin-coating using a CEE spinner followed by soft-baking on a hotplate. The soft-bake was usually done for 5 to 10 min at 100°C, depending on the thickness of PPC (5 min if PPC thickness was 10 µm or less, and 10 min if PPC thickness was greater than 15 µm) (Figure 2.1a step (ii)). A thin layer of BCB (2.5 to 3 µm) was coated on top of the PPC and patterned (Figure 2.1a step (iii)). The processing conditions for thin BCB layer were as follows: spin-coating “diluted BCB” at 5000 rpm for 120 s with a ramp rate of 500 rpm/s, soft-baking at 60°C for 2 min on a hotplate, exposure to 365 nm wavelength UV light with a dosage of 210 mJ/cm² using a negative-polarity photomask, post-exposure bake at 60°C for 5 min on the hotplate, pattern development by immersion into 1,3,5-triisopropylbenzene at 32°C for 1.5-2 min, and blow-drying with N₂ for 5 min. This thin BCB layer, referred to as pattern-transfer BCB layer, was utilized as an etch mask for

patterning PPC by O₂ plasma RIE (Figure 2.1a step (iv)). The RIE was performed using a Plasma-Therm RIE tool with 100 sccm O₂ flowrate at 25°C and 300 mTorr and with an AC power of 250 W. The etch selectivity of the RIE for BCB vs. PPC was 1:36. The PPC etch rate was 0.66 μm/min. Afterwards, a thick overcoat layer of BCB (undiluted, as-received) was coated on the substrate for encapsulating the patterned PPC (Figure 2.1a step (v)). The thickness of the overcoat BCB layer used in this study ranged between 7 μm to 16 μm, where the spin speed (1000-5000 rpm), soft-bake temperatures (70-85°C), exposure dosages (used intensity was 60 mJ/cm² per μm of BCB, 365 nm UV light) and post-exposure bake temperatures (70-85°C) were adjusted accordingly [118]. The encapsulation of the patterned PPC with overcoat BCB was found to be conformal using Dektak profile measurements. For the exposure of overcoat layer BCB, no photomask was used, and the flood exposure was done to initiate cross-linking all over the BCB. After that, the sample was placed horizontally on a glass rack and subjected to thermal treatment in a convection oven where the PPC was decomposed and BCB was cured simultaneously (Figure 2.1a step (vi)). During the thermal treatment, the convection oven was continuously purged with 2.5 L/min N₂. A ramp rate of 1°C/min was for all thermal treatments. The thermal treatment was done using various recipes that are discussed in the Results and Discussion section of Chapter 4.

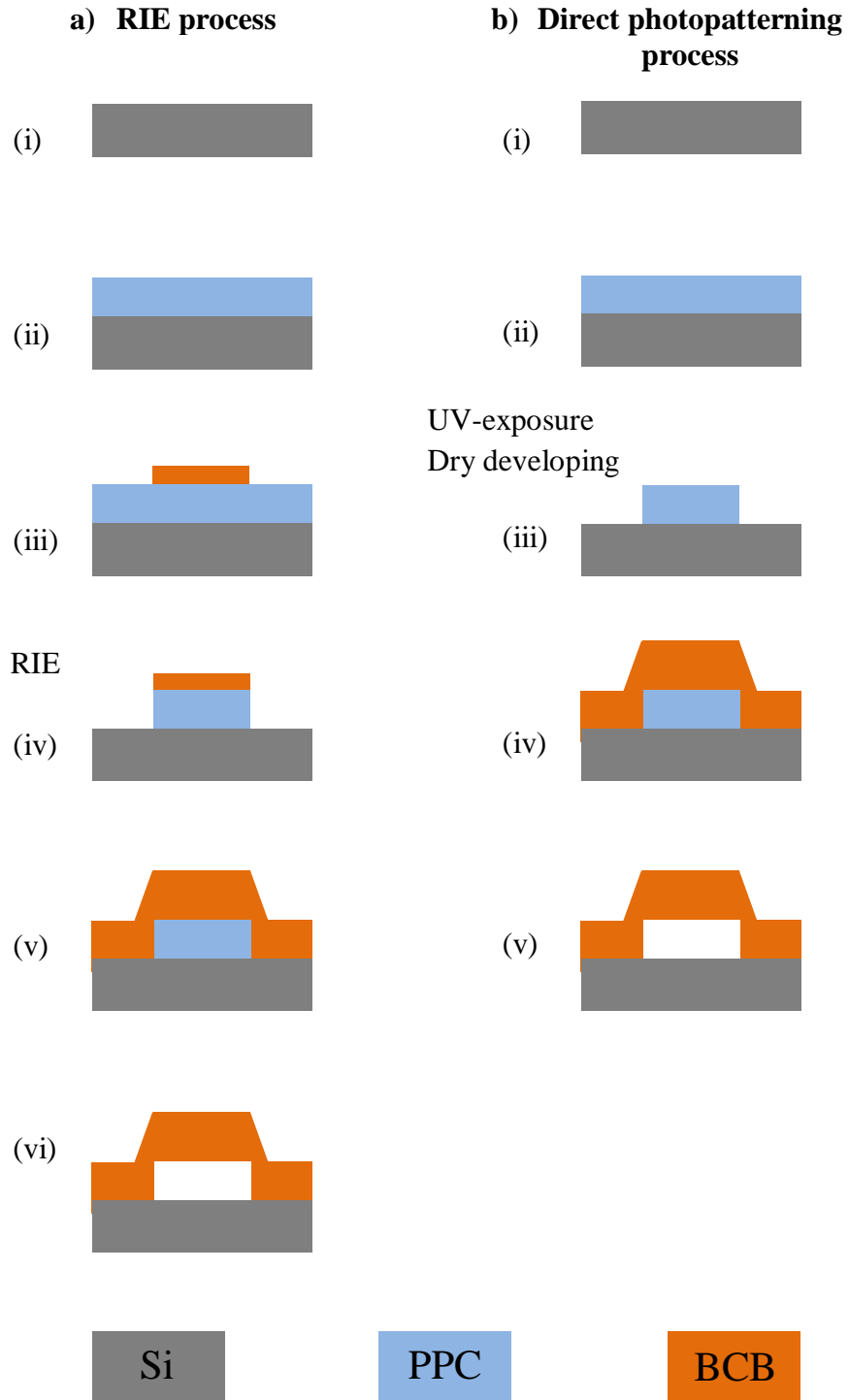


Figure 2.1 Air-gap formation process flows for (a) RIE process, and (b) Direct photopatterning process

The direct photopatterning process used photosensitive PPC as a single PPC layer, or a two-layer PPC film. A <100> silicon wafer (Figure 2.1b step (i)) was spin-coated and soft-baked (Figure 2.1b step (ii)). Unlike the RIE process, the PPC film was directly patterned using 248 nm UV radiation with a positive-polarity photomask (Figure 2.1b step (iii)). The PAG inside the photosensitive PPC film, Rhodorsil-FABA, forms a catalytic acid upon exposure. The exposure was performed using a Oriel Instruments exposure tool equipped with Hg(Xe) arc lamp which had an intensity of 71 mW/cm². The exposure time was selected to be 10 s per μm of the PAG-containing PPC layer if the PAG-containing PPC layer directly faces the UV light with no other layer in between (e.g. single photosensitive PPC layer or photosensitive PPC layer on top in a two-layer PPC film). If the photosensitive PPC layer was below a non-photosensitive layer in a two-layer film, the exposure time was selected to be 10 s per μm of the total two-layer PPC film in order to account for the intensity loss within the non-photosensitive PPC. After UV exposure, the PPC pattern was dry-developed at 100°C on a hotplate. During dry-development, the UV-exposed PPC decomposed into volatile compounds such as acetone or CO₂ at a temperature lower than the unexposed PPC. The duration of dry-development depended on the thickness of photosensitive PPC layer. Surface residue present after dry-development was removed by rinsing the sample with isopropanol followed by drying in a nitrogen stream. After dry-development, an overcoat layer of BCB was coated onto the substrate (Figure 2.1b step (iv)), exposed to 365 nm UV light, and post-exposure baked, as in the RIE process. Then, a thermal treatment was performed to obtain air-gaps (Figure 2.1b step(v)).

The lateral dimensions of the air-gap structures fabricated in this study were 2.5x3.2 mm rectangles, unless otherwise stated. A 2 mm diameter circular air-gap was used for nanoindentation.

2.2.3 Analysis Techniques

2.2.3.1 Thermal Characterization of Different PPC types

Thermogravimetric analyses (TGA) were performed to determine the decomposition temperature of the different PPC polymers in dynamic mode (temperature ramp) using a Q50 dynamic thermogravimetric analyzer from TA instruments (New Castle, DE). 3 to 15 mg of sample was loaded in a platinum pan in each run. The temperature ramp rate was 1°C/min. Isothermal TGA experiments were used to quantify the decomposition kinetics. The temperature was ramped at 20°C/min to the temperature of interest and held at that value for 500 min. The decomposition chamber was continuously purged with N₂ at a flow rate of 40 ml/min at the balance and 60 ml/min at the sample.

2.2.3.2 Chemical Structure Determination of PPCs using Nuclear Magnetic Resonance

The chemical structure of PPC was investigated using nuclear magnetic resonance (NMR) in order to determine any changes before and after purification. NMR measurements were performed using a Varian Mercury Vx 400 (400 MHz) tool (Agilent Technologies, Santa Clara, CA). The NMR solvent was chloroform-d (CDCl₃) supplied from Sigma Aldrich (product #:151831, 99.8 atom % D, contains 1 % v/v TMS). For each polymer, the concentration of PPC in the NMR tubes was held constant at 45 mg polymer in 0.75 ml CDCl₃. 512 scans were collected for ¹³C-NMR, and 64 scans were

collected for $^1\text{H-NMR}$. The relaxation time was 1 s for both $^{13}\text{C-NMR}$ and $^1\text{H-NMR}$. The spectra were analyzed using MestReC v4.9.9.9 software (Mestrelab Research, Escondido, CA). The peak positions in $^1\text{H-NMR}$ were calibrated by referencing the spectra with respect to the chemical shift of the residual solvent singlet peak at 7.26 ppm (i.e. $\sim 0.001\%$ undeuterated chloroform in CDCl_3). The peak positions in $^{13}\text{C-NMR}$ were calibrated by referencing the spectra to the center peak of the CDCl_3 triplet at 77.16 ppm [119]. The molar fractions of species in the NMR spectra were calculated by integrating the area under the peaks and normalizing with respect to total area of all identified species.

2.2.3.3 Mechanical Characterization of Overcoat using Nanoindentation

The mechanical properties of the overcoat were measured by nanoindentation. Nanoindentation measurements were conducted in quasistatic mode using a Hysitron TriboIndenter (model 1BR-12, Hysitron, Inc. Minneapolis, MN). The nanoindentation was performed in the acoustic housing, and the tool was vibration-isolated. A north star head diamond tip with a 100 nm radius of curvature was used for indentation. The load normal to the surface was varied nominally between 100 and 220 μN in a 3x3 grid with a 50 μm pitch. The load and unload times were kept constant as 10 s with no hold time between measurements. The maximum indentation depth was less than the 6.5% of the film thickness across all samples in order to minimize the effect of the substrate on the nanoindentation results.

2.2.3.4 Chemical Characterization and Thickness Measurement of PPC Residue

The thickness of the residue and its chemical composition were investigated using a Thermo K-alpha X-ray photoelectron spectrometer (XPS) (Thermo Fisher Scientific,

Waltham, MA). The energy step size was 1 eV for the survey scans and 0.1 eV for the elemental analysis. The X-ray spot size was 200 μm across all measurements. A low-voltage electron flood gun was used during measurements for charge compensation. In order to reduce noise in the XPS signals, each point was investigated twice for the survey scan, and five times for the elemental scan. The surface scans were performed without argon ion etching. The atomic concentrations in the depth profiles were obtained using an argon ion gun with a raster size of 0.3 mm. The argon ion gun was operated with an ion energy of 1000 eV, and the current was adjusted to give an etch rate of 5.65 nm/s, as referenced to Ta_2O_5 etching. The XPS scans were taken from the center of air-gap regions, unless otherwise stated. The acquired XPS survey scans were analyzed using Avantage software [110]. The carbon C1s signal was used as a reference signal for charge-shifting the acquired survey spectra so that the C1s peak position would be at the binding energy of 285.0 eV. The characteristic residue thickness was evaluated from the intersection of the Si and C signals as a function of depth. In addition to the survey scans, high resolution XPS scans for carbon were performed for detailed chemical characterization of the residue. The C1s peaks were deconvoluted into individual peaks corresponding to various carbon functionalities with different oxidation states. The fractional composition for each oxidation state was obtained from the deconvoluted spectra. The deconvolution and analysis of C1s signals were performed using CasaXPS software [111]. Same functional groups were looked for in both the non-photosensitive PPC residue and photosensitive PPC residue. The C-H peak position was 285.2 eV, C-C peak position was 284.7 eV, C-O-C peak position was 286.7 eV, C-O peak position was 287.0 eV, C=O peak position was 288.7 eV, O-C(=O)-O peak position was 290.6 eV, C-

F peak position was 287.8 eV, and there were two shake-up peaks at 291.9 eV and 294.1 eV [120-123]. The peak position tolerances were accepted as ± 0.2 eV for all functional groups in the C1s spectra. Linear or Shirley backgrounds were used for C1s region including all functionality peaks. The full width at half maximum (fwhm) values for all functional groups were constrained between 0.85 eV and 1.7 eV, and were kept same in a single peak set. The built-in simplex algorithm in CasaXPS was used to optimize the fitting of functional group peaks to the overall C1s peak with the objective of minimizing the residual. Same mixed Gaussian-Lorentzian line shapes were assigned to functionality peaks in a single C1s region. The mixing ratios of the Gaussian-Lorentzian line shape were optimized to further minimize the residual. Monte-Carlo simulation was performed to obtain the standard deviation of the calculated peak areas.

2.3 Thermal Stability Enhancement of Poly(propylene carbonate)

2.3.1 Materials

PPC with a molecular weight of 179,000 g/mol was obtained from Novomer Inc. The decomposition temperature (at 50% weight loss) was 210°C as determined by thermogravimetric analysis (TGA) using 0.5°C/min heating rate. PPC was used as-received without purification.

Silicon wafers with <100> orientation were supplied from University Wafers. The silicon wafers were used as substrates without prior cleaning except N₂ blowing to remove any dust or particles.

The PAGs used in this study were either iodonium-based PAGs including 4-methylphenyl[4-(1-methylethyl)phenyl]iodonium tetrakis(pentafluorophenyl)borate (Rhodorsil-FABA), bis(4-tert-butylphenyl)iodonium triflate (BTBPI-TF), bis(4-tert-

butylphenyl)iodonium perfluoro-1-butanesulfonate (BTBPI-NF) and diphenyliodonium triflate (DPI-TF), or sulfonium-based PAGs including tris[4-(4-acetylphenyl)sulfanylphenyl]sulfonium tetrakis(pentafluorophenyl)borate (Irgacure PAG 290, TAPSPS-FABA in this study) and tris[4-(4-acetylphenyl)sulfanylphenyl]sulfonium tris(trifluoromethylsulfonyl)methide (Irgacure GSID 26-1, TAPSPS-TMM in this study). The chemical structures and suppliers of PAGs are shown in Table 2.1. The PAGs were used as-received.

Table 2.1 Trade names, suppliers and chemical structures of PAGs

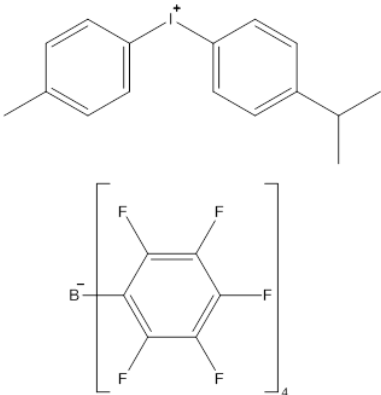
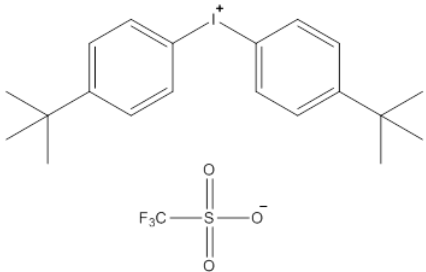
Trade name	Supplier	Chemical Structure
Rhodorsil-FABA	Rhodia	
BTBPI-TF	Sigma-Aldrich	

Table 2.1 continued

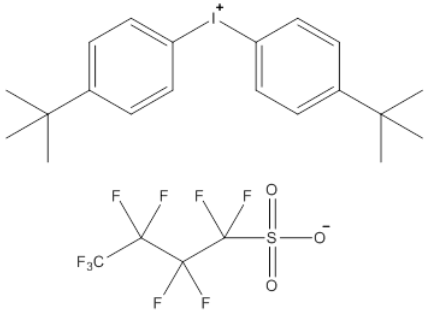
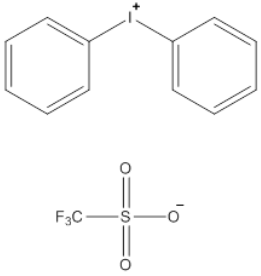
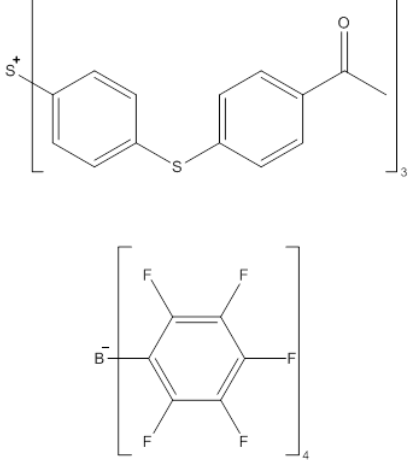
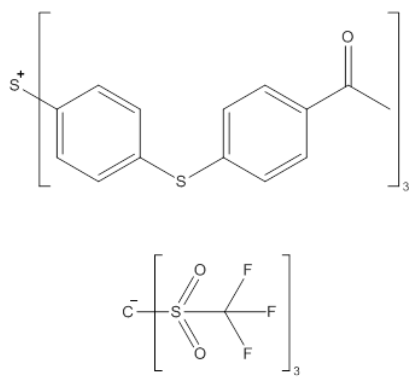
Trade name	Supplier	Chemical Structure
BTBPI-NF	Sigma-Aldrich	
DPI-TF	Sigma-Aldrich	
Irgacure PAG 290 (TAPSPS-FABA in this study)	Ciba/BASF	

Table 2.1 continued

Trade name	Supplier	Chemical Structure
Irgacure GSID 26-1 (TAPSPS-TMM in this study)	Ciba/BASF	

2.3.2 Processing

2.3.2.1 Preparation of PPC/PAG Solutions

The PPC/PAG solutions were prepared by mixing PPC with the PAG in γ -butyrolactone (GBL) solvent and mixing on a roller overnight. It is assumed that each PAG could produce one proton upon activation. Each PPC/PAG solution was prepared to have the same PAG molar concentration. A 3 wt% Rhodorsil-FABA PAG, with respect to PPC, was taken as the standard concentration so that a direct comparison could be made to previous studies [74]. The required amounts of PAGs as a weight percentage of PPC were calculated accordingly. The molecular weights and required amounts of PAGs in the PPC/PAG solutions are listed in Table 2.2. Amount of GBL added was four times the amount of PPC, so that the PPC/PAG solutions were each 20 wt% PPC in GBL. For UV-vis spectroscopy experiments, a solution of 20 wt% PPC in GBL without Rhodorsil-FABA was prepared.

Table 2.2 The molecular weights (g/mol) and required amounts of PAGs in the solutions expressed as wt% of PPC

PAG	Molecular weight (g/mol)	Required wt% of PPC
Rhodorsil-FABA	1016.25	3.00
BTBPI-TF	542.39	1.60
BTBPI-NF	692.42	2.04
DPI-TF	430.18	1.27
TAPSPS-FABA	1393.01	4.11
TAPSPS-TMM	1125.19	3.32

2.3.2.2 Preparation of Copper-Sputtered Substrates and PPC/PAG Coating

Silicon wafers with <100> orientation were supplied from University Wafers. The polymer films were spin coated using a CEE spinner onto either bare silicon wafers with a native oxide (no prior oxide cleaning) or wafers sputtered with Ti/Cu (300 Å/3000 Å) using a Unifilm DC sputterer. The Ti/Cu sputtered wafers were cleaned in a 11 vol% H₂SO₄ in de-ionized (DI) water solution for 30 sec with agitation before use in order to remove the native oxide on the copper. After the acid dip, the wafers were rinsed with DI water and dried with dry N₂. All polymer films were spin-coated to a thickness of ca. 10 µm using a spin speed of 1000 rpm for 40 s. The samples were then soft-baked at 105°C for 5 min on a hot plate. An Oriel Instruments Hg(Xe) lamp with 248 nm optics was used to irradiate the "exposed" samples to UV radiation at a dose of 154 mJ/cm² per µm of film thickness. No post-exposure baking was performed on the samples except the ones prepared for X-ray photoelectron spectroscopy (XPS) analysis.

2.3.3 Analysis Techniques

2.3.3.1 Thermal Characterization of PPC/PAG Films

Thermogravimetric analysis (TGA) experiments were performed to characterize the decomposition temperature of the polymer samples. Small pieces of polymer film were removed from the silicon substrates using a clean razor blade and loaded into platinum TGA pans. A Q50 dynamic thermogravimetric analyzer from TA Instruments was used. The temperature ramp rate was 0.5°C/min for the TGA runs. The decomposition chamber was purged with nitrogen at a flow rate of 40 ml/min at the balance and 60 ml/min at the sample. The microbalance was zeroed prior to each TGA run.

2.3.3.2 Copper Oxidation State Determination on the Surface of PPC/PAG Films

XPS analyses were performed to investigate the oxidation state of the copper in the polymer films. The XPS sample was a Ti/Cu sputtered silicon wafer with a 11 µm thick, UV-irradiated PPC film containing Rhodorsil-FABA PAG. The sample was post-exposure baked at 105°C for 5 min in order to obtain a copper-rich layer which was identified as responsible for the shift in decomposition temperature, as described previously [74]. After the post-exposure bake, the thickness of the polymer was measured as 6.4 µm, a value which is consistent over a range of experiments. Thus, it was concluded that copper ions migrate into the first ca. 7 µm of the film and cause the shift in decomposition temperature. A Thermo K-Alpha XPS tool was used for XPS analysis on the surface of copper-rich PPC layer. The binding energies for copper species were scanned between 925 eV and 965 eV with a step size of 0.1 eV. The elements present on

the surface of the sample were scanned in elemental survey mode between -10 eV and 1350 eV with a 1 eV step size.

2.3.3.3 Investigation of Photobleaching in PPC/PAG Films

UV-vis spectroscopy analysis was performed in order to evaluate the absorbance of the polymer solutions. UV-vis spectra were measured using Agilent 8453 UV-vis spectrophotometer and Quartz cuvettes (283 QS 1.000). Using a GBL blank, six samples were investigated: No PAG, Mixture, Cu Exposed, Si Exposed, Cu Unexposed, and Si Unexposed. The copper-sputtered or bare silicon substrates were spin-coated with PPC/Rhodorsil-FABA PAG solution, soft-baked, and exposed, if necessary. Pieces of polymer film were removed from the substrates, weighted, loaded into vials and diluted with fresh GBL to make the PAG concentration 0.286 $\mu\text{mole/ml}$. The amount of GBL required for dilution was calculated assuming that all GBL in the PPC film evaporated during soft-bake. This assumption was adequate for mixture calculations, however, Spencer et al. showed that a small amount of residual solvent remained in the films after soft-bake, which may affect the onset temperature of the decomposition [83]. All samples, except the ones identified as "No PAG" and "Mixture", were transferred into the cuvettes and the UV-vis spectra were measured. The "Mixture" sample was prepared by diluting the Rhodorsil-FABA solution directly with a certain amount of GBL in a vial in order to make the PAG concentration 0.286 $\mu\text{mole/ml}$, without spin-coating the solution on a substrate and collecting the baked film. In order to prepare the "No PAG" sample, a 20 wt% PPC in GBL solution with no Rhodorsil-FABA PAG was put into a vial and diluted with GBL whose amount was calculated assuming the PPC solution contained PAG. Since the UV-vis spectroscopy samples were prepared to have the same concentrations,

the UV-vis spectroscopy results would enable us to assign the absorbance peaks and wavelengths to certain species and assess the changes in their concentrations through changes in corresponding absorbance values.

CHAPTER 3

ELECTROLESS COPPER DEPOSITION USING TIN-SILVER CATALYST ON EPOXY LAMINATES

The goal of this study is to improve the electroless copper deposition process on epoxy laminate substrates using a non-palladium catalyst, and without the use of the swell-and-etch process. The motivation behind this study is three-fold: (i) there is a cost barrier with the conventional Pd-based catalysts in electroless deposition, (ii) the adhesion strength of the deposited electroless copper layer is critical to reliability, and (iii) the electrical performance of the deposited electroless copper is adversely affected by the surface roughness increase on which the conventional surface treatment methods are based (e.g. swell-and-etch method). Thus, it is attractive to lower the catalyst cost (i.e. non-palladium catalysts), and/or develop surface treatment methods that avoid adding surface roughness (i.e. elimination of the swell-and-etch process), without sacrificing the adhesion strength of the electrolessly deposited copper layers. In this study, different wet-chemical surface treatment methods including H_2SO_4 , H_3PO_4 and HCl treatments were investigated. The previously reported two-step catalyst seeding method involving Sn(II) oxidation to Sn(IV), and Ag(I) reduction to Ag(0) was used to activate the epoxy laminate surface for electroless copper [4]. The Sn/Ag catalysts created by the process were characterized using X-ray photoelectron spectroscopy (XPS). The adhesion strength of the electroless copper layers was evaluated.

3.1 Results

The quality and the rate of electroless copper deposition were evaluated using the baseline electroless sensitization and deposition process described in the Experimental Section (i.e. immersion in three sequential baths: (i) tin sensitization bath, (ii) silver activation bath, and (iii) electroless copper deposition bath). The amount of copper deposited onto the epoxy PWBs per area over a 20 min time was obtained gravimetrically, and the results are shown in Figure 3.1.

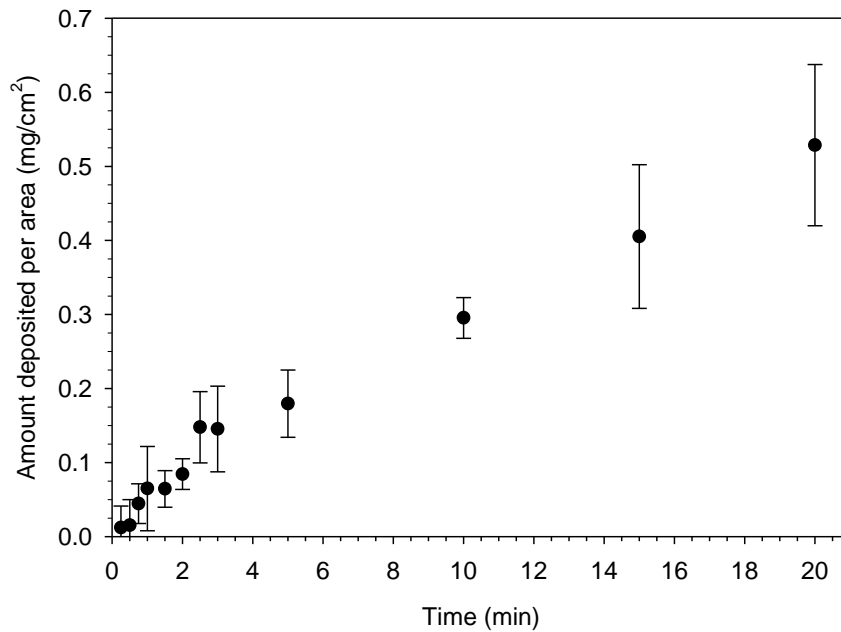


Figure 3.1 The amount of electroless copper deposited per area on epoxy laminates versus duration of electroless copper deposition

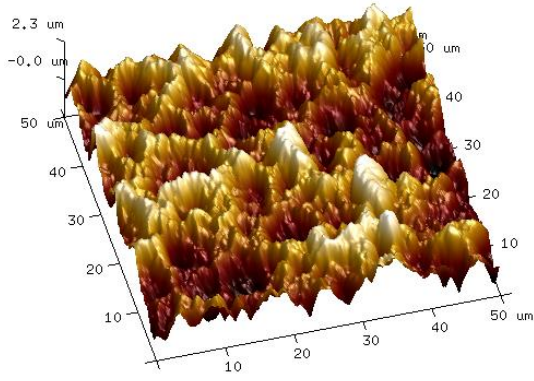
Four samples were processed to obtain the average mass of copper deposited and the error bars represent the 95% confidence interval. The mass of copper deposited changes almost linearly with time, which implies a constant deposition rate with little induction period needed to initiate deposition. Extrapolation of the longer time experiments back to zero thickness would indicate a 2 to 3 min induction time for the

electroless deposition process [109]. The error during the inductance period is high since there is little copper on the substrate. The average deposition rate calculated from Figure 3.1 after the induction period is 5.6×10^{-4} mg/cm² s. This deposition rate is in agreement with the deposition rate calculated using mixed potential theory, 6.3×10^{-4} mg/cm² s for this electroless plating bath [13].

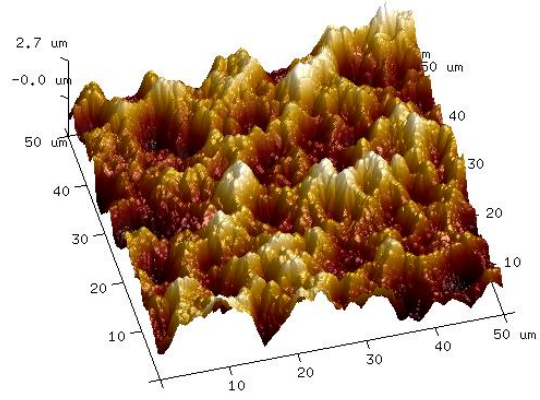
One of the interesting aspects of this process is the ability to catalyze the electroless process and achieve acceptable adhesion strength without using a palladium catalyst and the more complicated swell-and-etch pretreatment process. The surface pretreatment step and the catalyst seeding step are two critical steps responsible for the adhesion of electroless copper to the substrate. The conventional swell-and-etch wet-chemical treatment is based on the swelling of the epoxy polymer in a solvent, exposing the oxygen-containing functionalities to the surface and removing them with an etchant [8]. This method has been shown to increase the surface roughness, which in turn facilitates mechanical anchoring of the seed layer and the subsequent electroless copper layer.

The increase in surface roughness of the PWB substrate resulting from the sulfuric acid treatment was investigated using AFM after 1 min, 30 min and 180 min H₂SO₄ treatments at 95°C. The results were compared to a sample processed by the swell-and-etch treatment. The average (R_a) and root-mean-square (R_q) surface roughness values are shown in Figure 3.2. The starting PWB material had a R_a surface roughness of 621 nm. There was little change in the surface roughness after 1 min (660 nm), 30 min (685 nm) or 180 min (618 nm), while the swell-and-etch process increased the surface

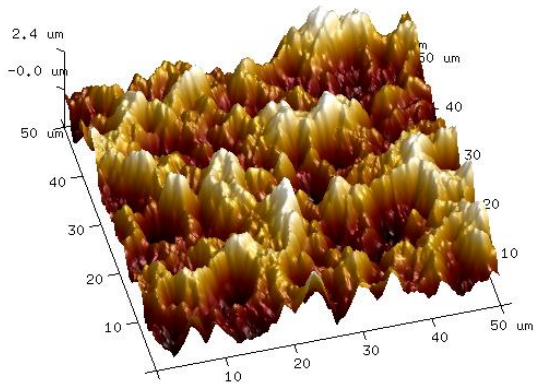
roughness to 819 nm. After 180 min in H_2SO_4 , there may have been a degree of surface smoothing due to the removal of the oxygen-containing functionalities [8, 25].



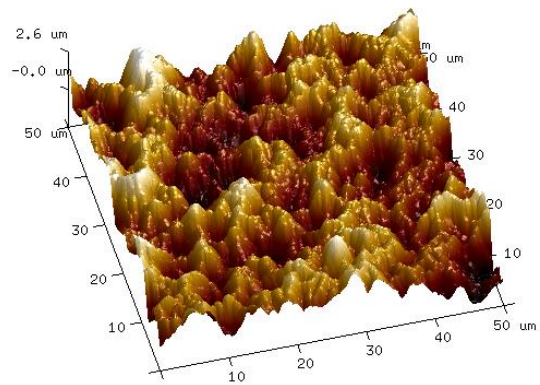
a) Plain Sample, R_a : 621 nm, R_q : 767 nm



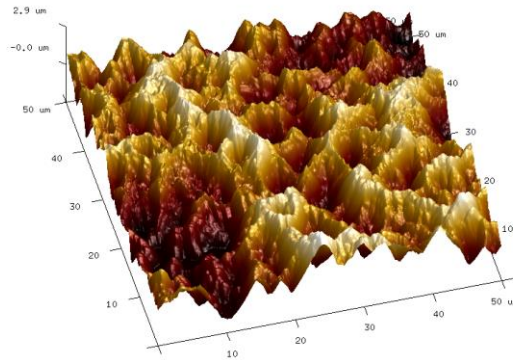
b) 1 min H_2SO_4 sample, R_a : 660 nm, R_q : 816 nm



c) 30 min H_2SO_4 sample, R_a : 685 nm, R_q : 840 nm



d) 3 hr H_2SO_4 sample, R_a : 618 nm, R_q : 773 nm



e) Swell-and-etch sample, R_a : 819 nm, R_q : 997 nm

Figure 3.2 AFM surface roughness profiles and surface roughness values R_a and R_q obtained from (a) plain epoxy laminate sample, (b) 1 min H_2SO_4 treated sample, (c) 30 min H_2SO_4 treated sample, (d) 3 hr H_2SO_4 treated sample, and (e) swell&etch sample

The evolution of the surface roughness during the electroless copper deposition procedure (sensitization, activation and deposition) was evaluated by AFM also for the tin sensitized, silver activated, electrolessly plated samples (1 and 10 min deposition). The surface roughness values are given in Table 3.1 along with the surface roughness values of the starting PWB and the sample treated for 30 min in H_2SO_4 . Except for a small increase in roughness as the electroless copper grows in thickness, there is little change in the roughness caused by any of the steps in this silver-catalyzed electroless process. The small decrease in the surface roughness after the silver activation step is possibly due to filling of the valleys in the surface by the Sn/Ag catalyst. The increase in surface roughness in the prolonged electroless copper deposition sample (e.g. 10 min electroless copper deposition sample) can be attributed to the characteristic grainy autocatalytic growth of electroless copper [124].

Table 3.1 The average (R_a) and root-mean-square (R_q) surface roughness values measured for samples at each step in electroless deposition process

Samples	Surface roughness (nm)	
	R_a	R_q
Plain	621	767
30 min H ₂ SO ₄ treated	685	840
Sn sensitized	691	860
Ag activated	660	808
1 min electroless Cu deposited	660	823
10 min electroless Cu deposited	706	878

The adhesion strength of the deposited electroless copper layer was measured, and the effect of the different sulfuric acid treatment times was evaluated. The adhesion strength values were measured to be 0.40 N/mm for the copper plated sample with 1 min H₂SO₄ treatment, 0.31 N/mm for the copper plated sample with 30 min H₂SO₄ treatment, and 0.33 N/mm for the copper plated sample with 180 min H₂SO₄ treatment. The errors corresponding to a 95% confidence interval were 0.07 N/mm, 0.05 N/mm, and 0.04 N/mm, respectively.

Thus, the H₂SO₄/tin-silver surface treatment was found to produce adherent electroless copper on the PWB substrates without increasing the surface roughness of the starting material. It should be noted that the as-received PWB sample had already some degree of roughness initially, i.e. $R_a=621$ nm and $R_q=767$ nm (see Table 3.1). In order to characterize the adhesion strength of smoother samples without changing the sample chemistry, the as-received samples were mechanically polished to decrease their surface roughness, as explained in the Experimental section. The surface roughness values evaluated from the Dektak line scans profilometer were $R_a=405$ nm and $R_q=493$ nm before polishing and $R_a=173$ nm and $R_q=225$ nm after polishing. A second sample had

an initial roughness of $R_a=430$ nm and $R_q=531$ nm before polishing, and $R_a=226$ nm and $R_q=315$ nm after polishing. The initial surface roughness values found here were less than the values obtained using AFM because the Dektak uses a larger diameter tip than the AFM. The surface roughness values of as-received (i.e. unpolished) samples were slightly different from each other because only one line scan was used to obtain the surface roughness values instead of the more accurate area scans in the AFM measurements. The polished samples were taken through the full H_2SO_4 /tin-silver electroless deposition process followed by electroplating copper to build the thickness for adhesion testing. The adhesion strength values of the samples were measured to be 0.032 N/mm and 0.054 N/mm, respectively, for the two samples. This shows that while the H_2SO_4 /tin-silver process did not increase the surface roughness, it still depended on the existing roughness to provide some of the adhesion strength.

The atomic composition of the sample surfaces was investigated using XPS survey scans. Table 3.2 shows the atomic percentages for a select number of elements at different points in the electroless process after 0, 10 and 20 s of argon ion etching. The analyzed elements include C, O, Sn, Ag, Cu, S, P, N, and Cl. These elements were selected because they make-up the chemical composition of the epoxy board and involve the species used in the surface pretreatments as well as electroless process. Trace amounts of other elements which do not affect this study, such as silicon and bromine, have been omitted from Table 3.2. The atomic percentages reported in Table 3.2 are reported with respect to all the elements found. The results in Table 3.2 show the surface and sub-surface elemental composition of the as-received PWB, a PWB taken through the steps of the H_2SO_4 /tin-silver process (H_2SO_4 treated, Sn sensitization, Ag activation

and electroless copper deposition), and the samples subjected to surface pretreatments similar to the H_2SO_4 treatment (i.e. the HCl and H_3PO_4 treatments). The sub-surface composition was obtained by ion etching of the sample using an Ar ion gun in the XPS tool. The etch rate of the Ar ion gun was 16.36 nm/s referenced to tantalum. Thus, a 10 s etch corresponds to about 160 nm into the sample, if its etch rate was similar to tantalum.

The as-received epoxy board was mainly composed of carbon (53.69%) and oxygen (24.75%) on the surface, as shown in Table 3.2. The oxygen-to-carbon (O/C) ratio of the as-received sample decreased from 0.46 to 0.08 to 0.05 with depth. Figure 3.3 shows the surface survey scan for the as-received PWB. Besides carbon and oxygen, small amount of other elements, such as magnesium (0.27%), sodium (1.01%), zinc (1.47%), copper (1.27%), iron (1.24%), chromium (1.81%), nitrogen (2.26%), calcium (0.58%), chlorine (3.63%), sulfur (1.89%), phosphorus (1.45%), silicon (3.68%) and bromine (1.01%) were also identified (not shown in Table 3.2). These are due to additives and other components of the PWB. Silicon comes from the glass fibers in the composite board, and bromine was likely due to flame retardant [107].

The hot H_2SO_4 treatment has been identified as an essential step in achieving adherent electroless copper. Omission of the hot sulfuric acid treatment resulted in no electroless copper deposition. Treating the as-received PWB with H_2SO_4 resulted in removal of the trace impurities including magnesium, sodium, zinc, copper, iron, chromium, calcium, chlorine, and phosphorus. The impurities remaining on the PWB were silicon, bromine, nitrogen and sulfur. The increase in the sulfur concentration was a result of the H_2SO_4 treatment. The H_2SO_4 treated sample also shows a decrease in the

O/C ratio compared to as-received sample. The O/C ratios going from the surface to the deepest level are 0.32, 0.04, and 0.03, respectively.

Table 3.2 The atomic percentage of elements in samples obtained from XPS survey spectra

Samples	Etch time (s)	Elements								
		C	O	Sn	Ag	Cu	S	P	N	Cl
Plain	0	53.69	24.75	0.00	0.00	1.27	1.89	1.45	2.26	3.63
	10	79.63	6.38	0.00	0.00	3.02	0.39	0.48	1.28	1.47
	20	83.98	4.36	0.00	0.00	2.24	0.39	0.35	1.08	0.96
H ₂ SO ₄ treated	0	69.65	22.33	0.00	0.00	0.00	3.08	0.00	2.01	0.00
	10	91.32	4.19	0.00	0.00	0.00	1.39	0.00	0.99	0.00
	20	92.30	3.19	0.00	0.00	0.00	1.40	0.00	1.03	0.00
H ₂ SO ₄ treated, Sn sensitized	0	55.40	29.42	7.59	0.00	0.00	2.65	0.00	2.28	0.81
	10	72.28	14.65	7.72	0.00	0.00	1.32	0.00	1.23	0.70
	20	75.40	11.95	6.85	0.00	0.00	1.27	0.00	1.21	0.85
H ₂ SO ₄ treated, Sn sensitized, Ag activated	0	60.73	24.80	2.43	2.67	0.00	3.62	0.00	3.78	0.38
	10	78.04	9.75	2.69	3.02	0.00	1.23	0.00	2.76	0.28
	20	81.25	7.54	2.42	2.68	0.00	1.08	0.00	2.89	0.29
H ₂ SO ₄ treated, Sn sensitized, Ag activated, 6 min Cu deposited	0	17.79	17.51	0.20	0.00	63.79	0.00	0.00	0.00	0.00
	10	5.66	6.38	0.15	0.18	86.98	0.00	0.00	0.00	0.00
	20	11.48	4.70	0.15	0.24	82.45	0.00	0.00	0.20	0.25
HCl treated	0	72.00	20.35	0.00	0.00	0.00	0.00	0.00	2.02	0.77
	10	92.51	3.70	0.00	0.00	0.00	0.00	0.00	0.65	0.35
	20	93.81	2.68	0.00	0.00	0.00	0.00	0.00	0.56	0.45
H ₃ PO ₄ treated	0	57.83	31.08	0.00	0.00	0.00	0.00	7.14	2.04	0.00
	10	88.66	6.31	0.00	0.00	0.00	0.00	2.52	0.81	0.00
	20	90.44	4.65	0.00	0.00	0.00	0.00	2.04	0.99	0.00
H ₃ PO ₄ treated, Sn sensitized	0	77.16	15.70	1.65	0.00	0.00	0.00	1.27	1.33	0.56
	10	91.72	3.20	0.73	0.00	0.00	0.00	1.00	0.80	0.08
	20	92.91	2.22	0.43	0.00	0.00	0.00	0.65	1.33	0.00

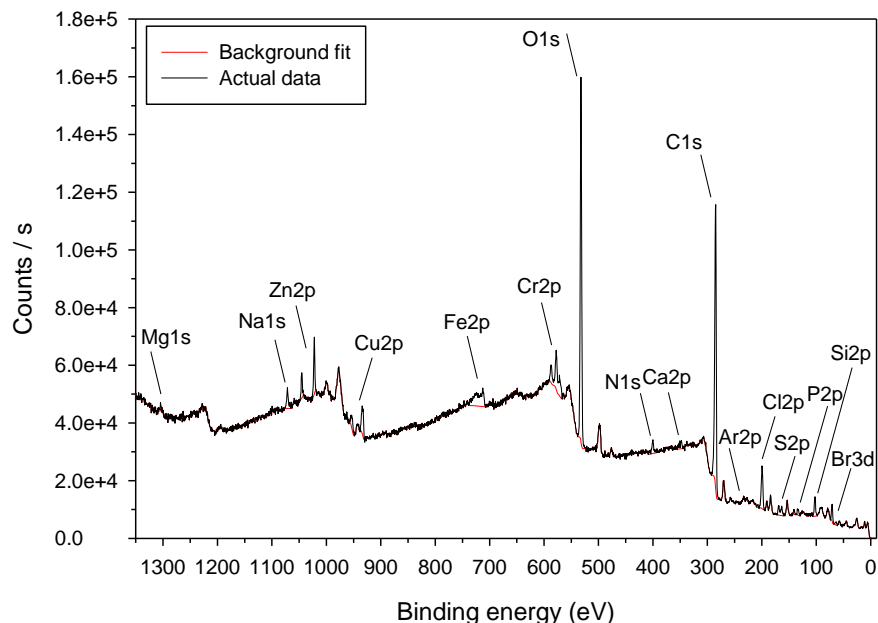


Figure 3.3 As-received PWB XPS survey spectrum

The first part of the catalyst seeding was the tin sensitization step. The tin sensitized sample had tin, chlorine, and sulfur in addition to carbon, oxygen, nitrogen, silicon and bromine. Some of the sulfur present on the surface was due to the previous H_2SO_4 treatment. Sn and Cl were likely from the $\text{SnCl}_2 \cdot 2\text{H}_2\text{O}$ bath used for tin sensitization. The Sn concentration was almost constant at about 7% with depth. The chlorine concentration was also found to remain constant at about 0.8%.

The second part of the catalyst seeding procedure involved silver activation after tin sensitization. In the silver activated sample, the elements identified were Ag, Sn, Cl, S, C, O, N, Si and Br. Ag comes from AgNO_3 bath. The presence of Sn and Cl is due to Sn sensitization. It was observed that the Ag and Sn concentrations are almost equal to each other at about 2.5% at the surface and the etched sub-surface. A small increase in the S concentration was observed with depth because of the presence of $(\text{NH}_4)_2\text{SO}_4$ in the

silver activation bath. AgNO_3 and $(\text{NH}_4)_2\text{SO}_4$ in the silver activation bath might also have contributed to the N content.

The deposition of electroless copper was performed after the tin sensitization and silver activation steps. The XPS survey scan of the copper plated sample shows the presence of Cu, Ag, Sn, Cl, N, C and O. The C and O were likely from adsorbed atmospheric gases onto the copper surface. In addition, a fraction of the O may be due to the oxidation of the electrolessly deposited copper.

The XPS survey scans were taken for the PWB samples exposed to other acids. The H_3PO_4 and HCl treatments were to see if the copper activation and adhesion was due to simply an acid treatment or if the H_2SO_4 had a more complex role. The elements detected on the HCl treated sample were C, O, Cl, N, Si, and Br. The impurities seen on the as-received sample were completely removed, except Cl. Given the fact the as-received sample also had Cl initially, it was concluded that the Cl content on the HCl treated sample decreased with HCl exposure. The HCl treated sample was taken through the tin sensitization and silver activation process followed by electroless copper plating. However, no electroless copper was deposited on the sample.

The H_3PO_4 treated sample had an elemental make-up including C, O, P, N, Si and Br. The other impurities were removed. An increase in the P content was observed compared to the as-received sample. The tin sensitization was performed on the H_3PO_4 treated sample. The Sn content on this sample was smaller than that for the sample taken through H_2SO_4 treatment and tin sensitization. The Cl coming from the tin sensitization bath was present in trace amounts. After tin sensitization and silver activation, the H_3PO_4 treated sample was electrolessly copper plated; however, the copper was not uniform in

color or thickness on the sample. The resulting surface film was not electrically conductive (i.e. it was not a contiguous film).

The XPS survey results shown above characterize the overall elemental composition of the surfaces after each chemical treatment; however, they are limited to simple identification and quantification of the elements present. High resolution elemental XPS analysis of specific elements, such as C1s and O1s, was performed to help understand the detailed changes that occurred on the sample surfaces. The individual elemental peaks were deconvoluted into several peaks corresponding to the different oxidation states or typical chemical functionalities present. In particular, the C1s scan is useful in terms of tracking the change in carbon functional groups as a result of chemical exposure [125]. Analysis of the O1s peak is less useful than C1s because oxygen has less of a change in peak position, and because of the presence of adsorbed oxygen on the sample [126]. It is known that surface treatments affect the outermost sample surface [7, 8].

The high resolution surface C1s results are shown in Figure 3.4 to Figure 3.7, and Table 3.3 to Table 3.6. The as-received PWB XPS scan, Figure 3.4 and Table 3.3, can be broken into four different functionalities: 64.39% hydrocarbon-like bonds (C-C, C-H), 29.59% alcohol and ether functionalities (C-O-H, C-O-C), 2.56% carbonyl-like species (C=O), and 3.38% acid and ester-like species (O-C=O). There was no higher oxidation state (i.e. carbonate-like peaks) observed on the as-received sample. After treatment of the as-received PWB in hot H₂SO₄, the molar concentration of functional groups changed to the following: 63.07% hydrocarbon groups, 31.90% alcohol and ether groups, 1.54% carbonyl groups and 1.05% carbonate groups, as shown in Figure 3.5 and Table 3.4. The

fraction identified as acid and ester group was statistically insignificant indicating that the content associated with an acid or ester oxidation state was removed in the hot H_2SO_4 treatment. A second change worth noting after the H_2SO_4 treatment is the emergence of a peak around 291.70 eV, which had a total area of 2.16%. In comparison, the H_3PO_4 treated sample had 70.27% hydrocarbon groups, and 27.82% alcohol and ether groups, as shown in Figure 3.6 and Table 3.5. There was no significant amount of carbonyl, acid and ester, and carbonate species observed on the sample. The peak at 291.40 eV corresponds to 1.74% of the total area. The species identified on the HCl treated sample in Figure 3.7 and Table 3.6 are 62.39% hydrocarbon, 35.48% alcohol and ether, and 1.29% carbonyl. There was no carbonate, and acid/ester species found. There was also a new peak observed at 291.53 eV corresponding to 0.84% of the total area. Overall, the amount of carbonyl, and acid/ester functionalities decreased after the acidic surface treatments. The hydrocarbon, and alcohol/ether remained the same or increased slightly, and a new peak at 291.5 eV was observed in all surface treated samples. The XPS spectra after argon ion milling did not show the emergence of this new peak (data is not shown). The peak at 291.5 eV was observed only at the surface of the acid treated samples.

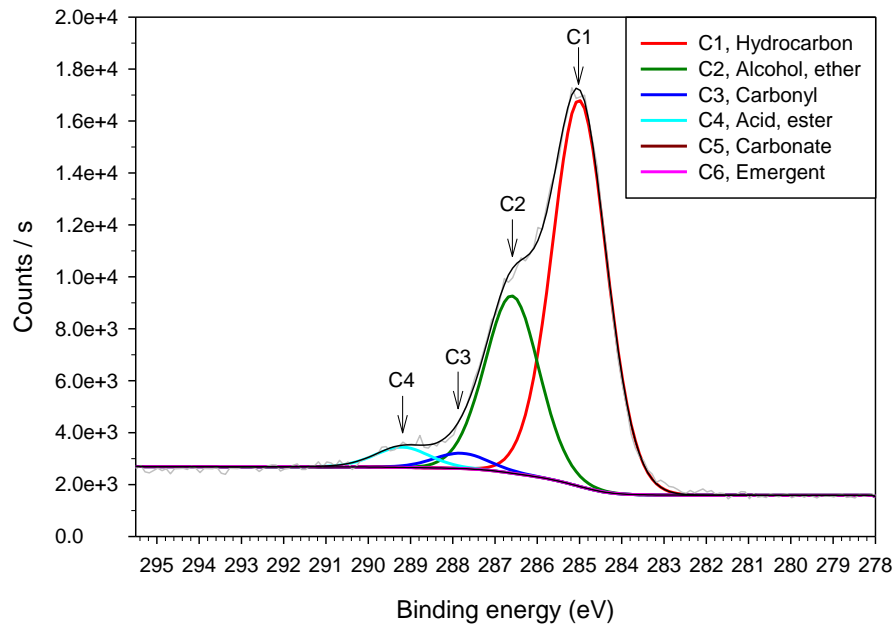


Figure 3.4 High resolution XPS C1s spectrum, peak fit and peak deconvolution for as-received PWB sample

Table 3.3 C1s peak deconvolution results of as-received PWB sample

Functionality	Peak Position (eV)	FWHM (eV)	Line Shape	% Area	% St. dev.
Hydrocarbon	285.00	1.516	GL(30)	64.39	1.00
Alcohol, ether	286.60	1.516	GL(30)	29.59	0.59
Carbonyl	287.80	1.516	GL(30)	2.56	1.00
Acid, ester	289.20	1.516	GL(30)	3.38	0.65
Carbonate	290.33	1.516	GL(30)	0.03	0.07
Emergent	291.45	1.516	GL(30)	0.05	0.12

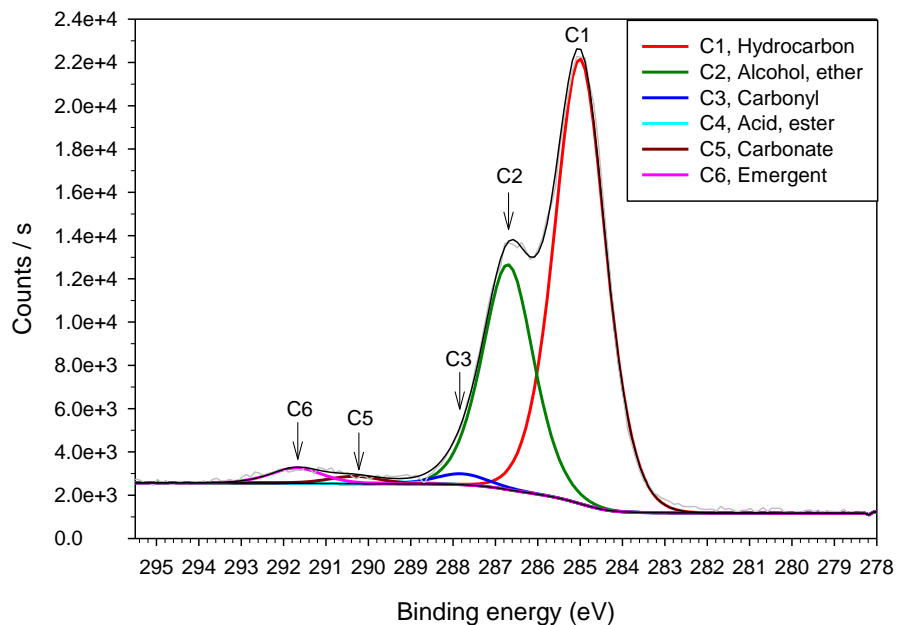


Figure 3.5 High resolution XPS C1s spectrum, peak fit and peak deconvolution for H₂SO₄ treated PWB sample

Table 3.4 C1s peak deconvolution results of H₂SO₄ treated PWB sample

Functionality	Peak Position (eV)	FWHM (eV)	Line Shape	% Area	% St. dev.
Hydrocarbon	285.00	1.423	GL(50)	63.07	1.20
Alcohol, ether	286.70	1.423	GL(50)	31.90	0.60
Carbonyl	287.80	1.423	GL(50)	1.54	0.58
Acid, ester	289.20	1.423	GL(50)	0.28	0.45
Carbonate	290.33	1.423	GL(50)	1.05	0.45
Emergent	291.70	1.423	GL(50)	2.16	0.51

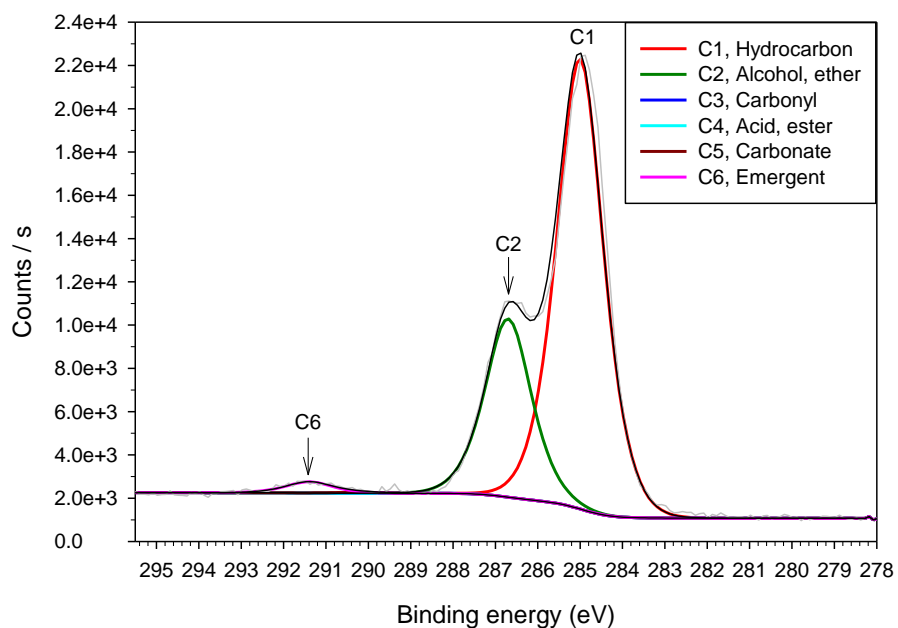


Figure 3.6 High resolution XPS C1s spectrum, peak fit and peak deconvolution for H_3PO_4 treated PWB sample

Table 3.5 C1s peak deconvolution results of H_3PO_4 treated PWB sample

Functionality	Peak Position (eV)	FWHM (eV)	Line Shape	% Area	% St. dev.
Hydrocarbon	285.00	1.291	GL(60)	70.27	0.80
Alcohol, ether	286.70	1.291	GL(60)	27.82	0.40
Carbonyl	287.98	1.291	GL(60)	0.01	0.01
Acid, ester	289.05	1.291	GL(60)	0.02	0.07
Carbonate	290.25	1.291	GL(60)	0.14	0.15
Emergent	291.40	1.291	GL(60)	1.74	0.49

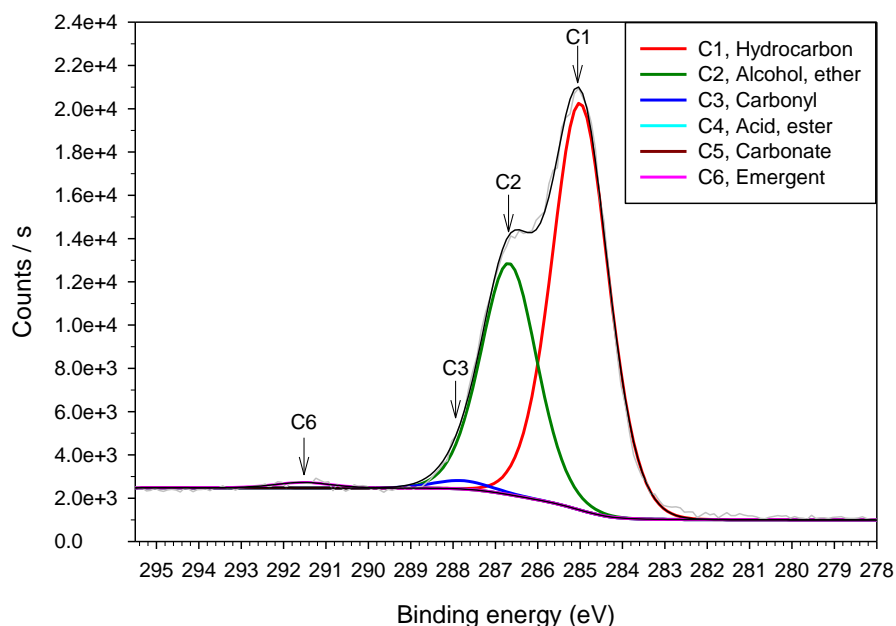


Figure 3.7 High resolution XPS C1s spectrum, peak fit and peak deconvolution for HCl treated PWB sample

Table 3.6 C1s peak deconvolution results of HCl treated PWB sample

Functionality	Peak Position (eV)	FWHM (eV)	Line Shape	% Area	% St. dev.
Hydrocarbon	285.00	1.562	GL(40)	62.39	0.76
Alcohol, ether	286.68	1.562	GL(40)	35.48	0.51
Carbonyl	287.80	1.562	GL(40)	1.29	0.78
Acid, ester	289.04	1.562	GL(40)	0.00	0.00
Carbonate	290.30	1.562	GL(40)	0.00	0.00
Emergent	291.53	1.562	GL(40)	0.84	0.41

The high resolution XPS scans of tin sensitized and silver activated samples (after a H₂SO₄ treatment) are shown in Figure 3.8 and Figure 3.9 (also in Table 3.7 and Table 3.8), respectively. The spectra were charged shifted holding the C-H, C-C bonds at 285 eV constant. The deconvolution of the peaks was performed using a single deconvolution region and two peak regions (one for each 3d_{5/2} and 3d_{3/2} peaks) for both tin and silver in order to determine the position and area for each peak. The Gaussian-Lorentzian mixture

line shapes were optimized for achieving the minimum residual. Using the same sensitivity factor for the major peaks for each element, the characteristic area ratio of 3:2 for the $3d_{5/2}$ and $3d_{3/2}$ peaks, due to spin-orbit coupling in tin and silver, was found [112], as shown in Figure 3.8 (Table 3.7) and Figure 3.9 (Table 3.8). The peak positions for the $3d_{5/2}$ and $3d_{3/2}$ peaks corresponded to 487.87 eV and 496.28 eV for tin, and 368.95 eV and 374.94 eV for silver, respectively. Even though it is difficult to distinguish between Sn(II) and Sn(IV) using XPS [127], it can be concluded that tin is not in the metallic state, i.e. no Sn(0) is present [108, 122]. The literature values reported for binding energy of 487.8 eV coincides mostly with SnO₂ [128-132], although there are some reports for SnO at that binding energy [133]. It is also possible that Sn may be in the form of a chloride complex [122, 134, 135]. The Ag $3d_{5/2}$ peak obtained at 368.95 eV is higher than that reported for elemental silver, 368.2 eV in [122, 136]; however the Ag $3d_{5/2}$ peak may be due to elemental Ag [108, 136, 137] because the binding energy can differ from bulk values when the metal is in the form of small clusters [136]. An increase in binding energy has been previously observed for small clusters of Pd, Pt, and Au [138, 139]. The formation of a Sn/Ag alloy could change the binding energy of the Ag $3d_{5/2}$ peak [140]; however, this appears unlikely due to the lack of a reducing agent for producing Sn from Sn(II). In addition, the formation of a Sn-Ag alloy is not thermodynamically favorable compared to formation of a Sn-Pd alloy in the Pd-based catalysts. The enthalpy of mixing and Gibbs energy of mixing values for Sn-Ag alloy are much less negative than that of Sn-Pd system [141]. The Sn-Pd binary alloy diagram shows a number of possible crystalline phases at room temperature (Pd₃Sn, Pd₂Sn, Pd₃Sn₂, PdSn, PdSn₂, PdSn₃, PdSn₄). However, the Sn-Ag system does not have a mixed crystalline phase [142]. The

XPS results show that the H₂SO₄ treated sample was indeed seeded with a tin-silver catalyst after the tin sensitization and silver activation steps. It is most likely that the Sn(II) served as the reducing agent for Ag(I) in a way analogous to the tin-palladium catalyst in the traditional Shipley process [14].

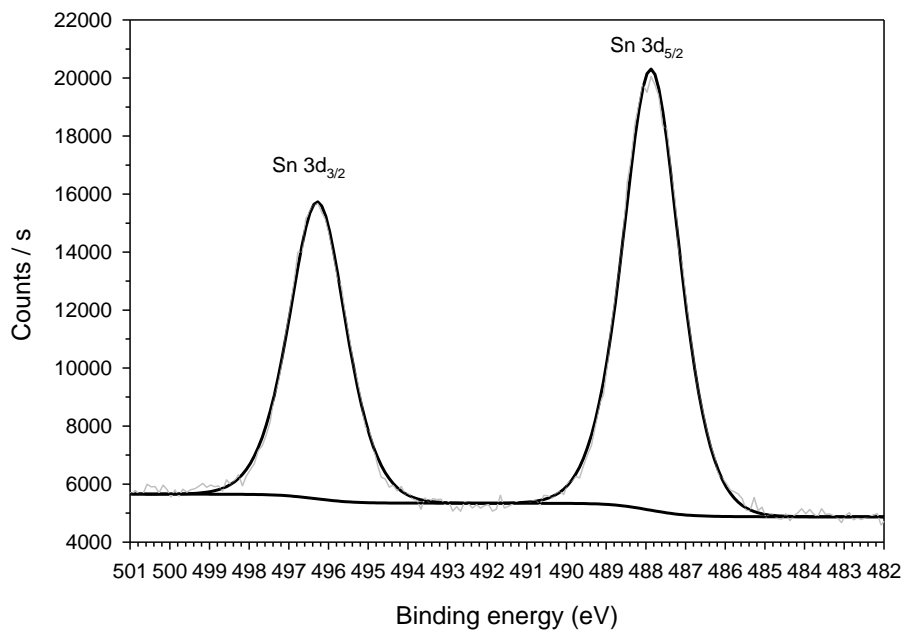


Figure 3.8 Ag activated PWB sample high resolution XPS spectrum, peak fit and peak deconvolution for Sn

Table 3.7 Sn peak deconvolution results

Peak	Peak Position (eV)	FWHM (eV)	Line Shape	% Area	% St. dev.
Sn 3d _{5/2}	487.87	1.687	GL(55)	59.77	0.27
Sn 3d _{3/2}	496.28	1.687	GL(55)	40.23	0.27

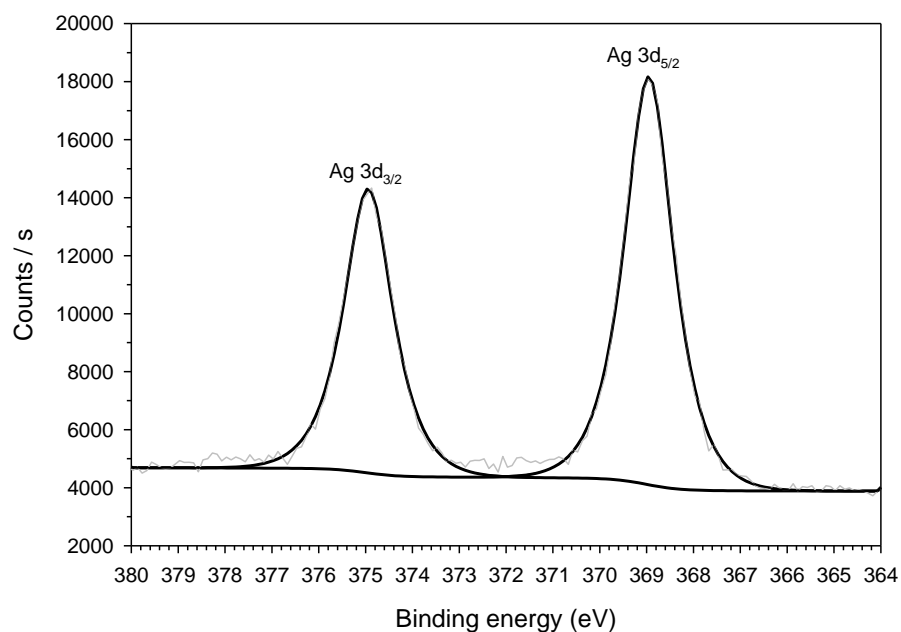


Figure 3.9 Ag activated PWB sample high resolution XPS spectrum, peak fit and peak deconvolution for Ag

Table 3.8 Ag peak deconvolution results

Peak	Peak Position (eV)	FWHM (eV)	Line Shape	% Area	% St. dev.
Ag 3d _{5/2}	368.95	1.235	GL(80)	58.96	0.30
Ag 3d _{3/2}	374.94	1.235	GL(80)	41.04	0.30

3.2 Discussion

The H₂SO₄ pre-treatment has been shown to establish a surface which can be tin sensitized and silver activated. The sensitization and activation process forms a colloidal catalyst for the electroless copper deposition. During the catalyst seeding (i.e. tin sensitization and silver activation), Sn(II) is oxidized to Sn(IV), while Ag(I) is reduced to Ag. Silver is a catalyst for the copper formaldehyde electroless bath [4, 15-17, 108].

Seeding of the tin/palladium catalytic colloid onto the epoxy surface is accompanied by an increase in surface roughness in the swell-and-etch process [7, 8, 18, 22, 25]. In contrast, the surface was not appreciably roughened by the H₂SO₄ pretreatment, even for over-etched surfaces, as shown in Figure 3.2. The results also show that the H₂SO₄ pretreatment produced a unique surface for catalyst seeding, which was not recreated by other strong acids, HCl and H₃PO₄. There was no electroless copper deposited onto the epoxy substrates when other strong acids of similar concentration were used. It was found that times as short as 30 s in H₂SO₄ were adequate to achieving adherent electroless copper deposits on an epoxy substrate. These observations imply that the H₂SO₄ pretreatment produces a chemical change to the surface specific to sulfate, rather than simply a mechanical effect, such as increasing the surface roughness.

XPS survey scans give insight into the nature of the H₂SO₄ pretreatment. The as-received sample contained carbon, oxygen, silicon, bromine and nitrogen which are part of the epoxy laminate. The other impurities, including magnesium, sodium, zinc, copper, iron, chromium, calcium, chlorine, and phosphorus were removed by the H₂SO₄ pretreated. The sulfur concentration increased, due to the presence of sulfate remaining on the sample surface. The replacement of metal ions, most likely in a positive oxidation state, with sulfate anions, may lead to a charge reversal on the epoxy surface which could assist in colloidal adhesion. The effectiveness of even short H₂SO₄ pretreatments shows that only surface changes are taking place. However, simply removing impurities was not sufficient to facilitate catalyst adhesion and electroless copper deposition because the HCl and H₃PO₄ treated surfaces also showed that the impurities were removed for the surface. Only phosphorus remained on the H₃PO₄ treated surface, in addition to the epoxy

containing carbon, oxygen, silicon, bromine and nitrogen. The H_2SO_4 and H_3PO_4 pretreat were similar to the extent that they are both strong acids, removed impurities and left an anion-containing surface. However, the H_3PO_4 pretreatment led to only irregular, trace amounts of electroless copper deposition. The amount of tin detected on the H_3PO_4 pretreated and tin sensitized sample was less than the amount of tin adsorbed on the H_2SO_4 pretreated surface (see Table 3.2). This may be due to the lower solubility for the tin-phosphate complex compared to the tin-sulfate complex [143]. If the tin precipitates on the surface as the simple salt and not a tin-sulfate complex, it may be washed away in subsequent washing steps.

In the case of the HCl treated sample, the residual Cl on the surface was less than in the as-received sample. The HCl pretreated sample produced no electroless copper deposition. Thus, it appears that the adsorbed sulfate ions (or small amounts of phosphate ions) enable the colloidal tin ions to be stabilized on the surface during tin sensitization.

Additional information about the chemical effect of the H_2SO_4 pretreatment can be gained from the high resolution surface C1s scans, shown in Figure 3.5. Apart from removing impurities from the surface and facilitating the sulfate or phosphate adsorption, the nature of the carbon moieties on the surface also can be important. In both the as-received and the acid pretreated samples, the majority of the carbon species, between 94-98%, were from the hydrocarbon (C-C, C-H), and alcohol and ether (C-O-C, C-O-H) groups. There was little or no change in the molar concentration of these functionalities between the as-received sample and those which had been acid pretreated. One common trend observed was a decrease in the carbonyl (C=O), and acid and ester (O-C=O) content after acid treatment, regardless of the acid used. The as-received sample had

2.56% carbonyl species and 3.38% acid and ester species. The concentration of carbonyl, and acid and ester species decreased to 1.54% and 0.28% after H₂SO₄ pre-treatment, 0.01% and 0.02% after H₃PO₄ pre-treatment, and 1.29% and 0.00% after HCl treatments, respectively. It is possible that the strong acids attack the carbonyl oxygens due to their Lewis base nature (i.e. electron pair donor). This acid-base interaction can lead to bond breaking and formation of CO and CO₂ [28, 36]. This is also reflected in the decrease in surface O/C ratio for the acid treated samples. The as-received sample had a O/C ratio of 0.46 whereas the H₂SO₄ pretreated sample had a surface ratio of 0.32 and the HCl sample had a value of 0.28. The H₃PO₄ pretreated sample did show an increase in the O/C ratio, possibly due the high oxygen content in the phosphate. It is noted that strong acids can oxidize the carbonyl, acid and ester species to a higher oxidation state, such as carbonate [28, 36].

An interesting difference in C1s scans between the as-received and acid treated samples is the occurrence of a new peak at 291.5 eV, as seen in Figure 3.5, Figure 3.6 and Figure 3.7. This new peak was found only at the surface and not in the argon ion etched scans. This peak may be due to newly formed CO₂ or CO upon bond breaking by acid treatment [144-146]. It is known that the surface pre-treatment mostly affects the surface and not the sub-surface [8].

The colloidal nature of the tin sensitized and silver activated surface can be seen in the Sn 3d_{5/2} peak at 487.87 eV with a spin-orbit splitting of 8.41 eV. This binding energy indicates that no elemental Sn is present [108, 122] (i.e. Sn is found to be either in Sn(II) or Sn(IV) form) [128-133]. The tin is more likely in the Sn(IV) form as in SnO₂ [128-132]. The binding energy for Sn is also in accordance with a Sn chloride complexes

[122, 134, 135]. Even though the observed binding energy of 368.95 eV for Ag 3d_{5/2} peak is slightly higher than the reported value of 368.2 eV in the literature [122, 136], it is likely that this increase is due to Ag being packed in small clusters [136], and Ag was most probably in elemental state [108, 136, 137]. These findings support the reduction of Ag(I) to Ag(0) by oxidation of Sn(II) to Sn(IV) [15, 16, 108]. It appears that the most likely form of the tin-silver species is as a core-shell nano-colloid which has a metallic silver core surrounded by a Sn(IV) species, which are likely to be SnO₂ and/or a tin-chloride complex. The possibility of the tin being in a tin-chloride complex is consistent with the high concentration of Cl in the XPS spectra, Table 3.2. The negatively charged Cl⁻ ions may serve as a stabilizer for the nano-colloid [9, 10, 16, 17].

The XPS survey results for the H₂SO₄ pretreated sample after tin sensitization and silver activation showed almost a 1:1 atomic concentration ratio for the Sn and Ag. In our two-step catalyst seeding process, the concentration of Ag in the Ag bath, 22.1 mM, was less than the concentration of Sn in the Sn bath, 36.6 mM. Similarly, in the study by Fujiwara et al., the nano-colloids showed approximately a 1:1 Sn:Ag atomic ratio (see “not conditioned” curve in Figure 4 in reference [16]), even though the catalyst seeding solution had 10 mM Ag and 100 mM Sn. These results indicate that Ag is likely the limiting reagent in the nano-colloid formation. This is supported by the study of Vaskelis et al. where an increase in the density of the Sn/Ag colloid was observed by UV-vis spectroscopy when the Ag(I) concentration was increased in the presence of excess Sn(II) [15]. The 1:1 atomic ratio observed in this study and also in the study by Fujiwara et al. [16], might indicate that all the Ag(I) which was reduced by the Sn(II) oxidation does not end up in the nano-colloid because then the Sn:Ag ratio would be 1:2 otherwise.

Alternatively, the Sn due to SnCl_3^- ions residing on the outer surface of the nano-colloid could account for Sn:Ag ratio being about 1:1.

Finally, the findings reported here can be used to summarize the mechanism for the adhesion of the electroless copper onto the epoxy laminate substrates. The H_2SO_4 treatment ultimately improves the copper adhesion and facilitates the adsorption of the Sn/Ag catalyst without increasing the surface roughness. Impurities were removed from the as-received substrate in the H_2SO_4 pretreatment leading to a charge reversal on the surface. The number of carbonyl, acid and ester functionalities gets decreased. In addition, the lower O/C ratio shows that the carbonyl surface was changed. The H_2SO_4 pretreated surface had adsorbed sulfate ions which enabled Sn(II) sensitization. Ag activation occurred through reduction of the Ag(I) forming a core-shell nano-colloid. The nano-colloids are likely negatively charged due to the presence of the chloride complexing agent. This negative charge can prevent the agglomeration of the nano-colloids. The electrochemical reaction involving reduction of Cu(II) to Cu(0) and oxidation of formaldehyde is catalyzed by the Sn/Ag nano-colloids leading to adherent, continuous and uniform electroless copper deposition on the epoxy laminate substrates.

3.3 Summary and Conclusions

In this study, electroless copper plating on epoxy laminates has been investigated using a Ag-based catalyst, and non-roughening sulfuric acid surface treatment. Conventional Pd-based catalyst is expensive, and the widely used swell-and-etch method creates substantial surface roughness which is detrimental for electrical performance. The H_2SO_4 treatment was observed to introduce little or no surface roughness to the epoxy laminate. No electroless copper deposition was observed without the H_2SO_4 treatment.

The amount of carbonyl (C=O) and acid/ester (O-C=O) functionalities were observed to decrease after the H₂SO₄ treatment. Surface pretreatment with H₂SO₄ was unique in catalyst seeding, compared to other acid treatments including HCl and H₃PO₄. The sulfate content adsorbed on the epoxy laminate after H₂SO₄ treatment enabled Sn(II) sensitization by electrostatic attraction. XPS results indicated Sn(II) oxidation to Sn(IV) and Ag(I) reduction to Ag(0), so as to form a core-shell nano-colloidal catalyst with Ag(0) core and SnO₂ shell. It is possible that some SnCl₃⁻ resided on the outer surface of the nano-colloids providing stability by preventing agglomeration [9, 10]. Sn/Ag nano-colloids were observed to catalyze the electroless copper deposition. Overall, the chemical adhesion was promoted by H₂SO₄ treatment rather than mechanical adhesion, and the use of Sn/Ag catalyst with H₂SO₄ surface treatment facilitated adherent, continuous and uniform electroless copper layers on epoxy laminates.

CHAPTER 4

SIZE-COMPATIBLE, POLYMER-BASED AIR-GAP FORMATION PROCESSES AND POLYMER RESIDUE ANALYSIS FOR WAFER- LEVEL MEMS PACKAGING APPLICATIONS

In this study, the polymer-based air-gap formation process for MEMS packaging applications was investigated with an emphasis on the formation of wide (>3 mm) and tall (>10 μm) air-gaps, and chemical assessment of the residue from photosensitive and non-photosensitive sacrificial polymers. Two different commercially available PPC materials were compared using thermogravimetric analysis (TGA) and nuclear magnetic resonance (NMR) analysis. A PPC purification method involving re-dissolution and precipitation was employed. BCB (Cyclotene 4026-46) was used as a PPC-compatible overcoat material with excellent mechanical strength. BCB was also used as a pattern-transfer layer in the RIE process. The residue thickness in the air-gap region was characterized by depth profiling using X-ray photoelectron spectroscopy (XPS). The chemical functionalities in the residue were analyzed by deconvolution of the XPS carbon peaks.

4.1 Results and Discussion

Two different PPC materials, Novomer 160K and QPAC 40 141K, were purified, as explained in the Experimental section. Figure 4.1 and Figure 4.2 show the TGA data of both types of PPCs before and after purification. As seen in Figure 4.1, the purified Novomer 160K had a lower decomposition temperature compared to its neat form (i.e. unpurified, as-received). The decomposition temperature at 50 wt% loss dropped from 241.9°C to 218.0°C when purified. The decomposition onset temperature at 5 wt% loss also dropped after purification from 224.6°C to 197.1°C. The rate of decomposition did not change appreciably with purification, i.e. the slopes of TGA curves during weight loss were similar. The as-received and purified form of the Novomer 160K decomposed without noticeable residue, as measured by the mass at 350°C. On the other hand, the QPAC 40 141K had a slightly higher decomposition temperature after purification, as seen in Figure 4.2. The decomposition temperature at 50 wt% loss was 233.7°C for the purified PPC compared to 224.4°C in the as-received (neat) form. A slight increase was observed also in the onset of decomposition temperature: 205.3°C for purified PPC vs. 196.3°C for the as-received neat form. The rate of decomposition increased slightly for the purified material, especially at the higher temperature end of the scan. Both neat and purified forms of QPAC 40 141K had about 0.23 wt% residue at 350°C.

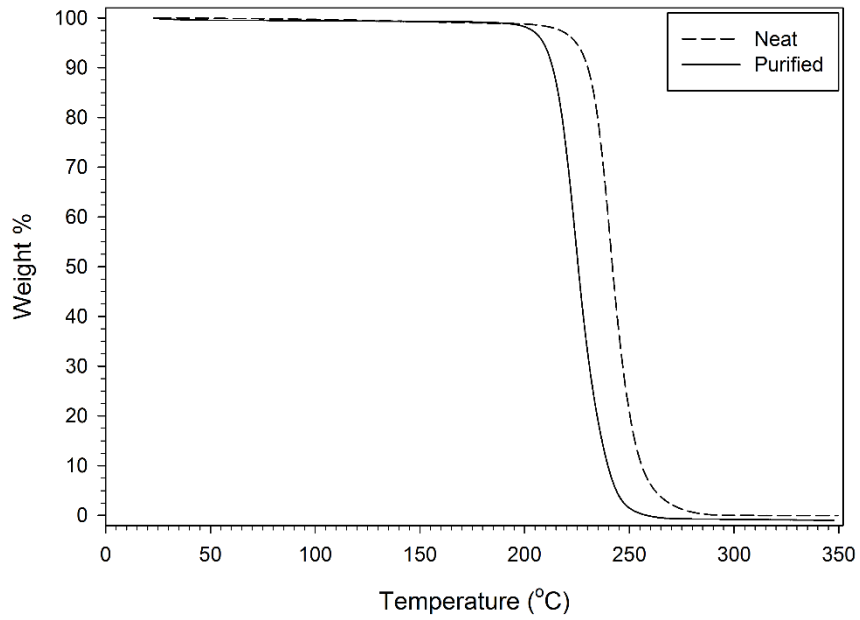


Figure 4.1 TGA results of neat and purified Novomer 160K

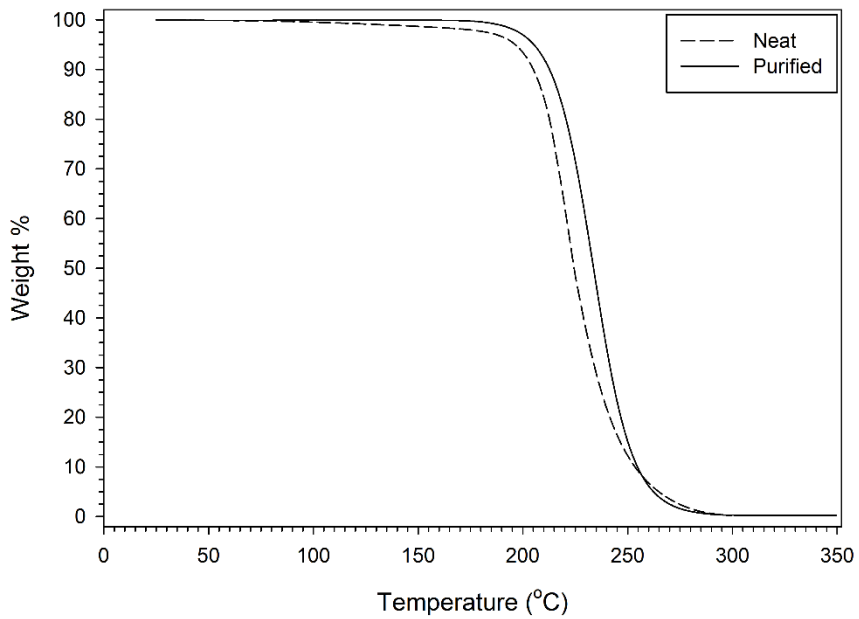


Figure 4.2 TGA results of neat and purified QPAC 40 141K

As shown previously, a majority of the shift in the PPC decomposition temperature was most likely due to residual solvent used during purification. Hydrogen bonding of the polymer, particularly at the end groups, could change the decomposition temperature by making the decomposition reaction (and intermediates) more facile or more labile [113].

The chemical structure and the impurity content of Novomer 160K and QPAC 40 141K were analyzed using $^1\text{H-NMR}$ and $^{13}\text{C-NMR}$. The chemical structure of PPC is shown in Figure 4.3 where the carbon and hydrogen atoms are labeled for referencing to the NMR spectra.

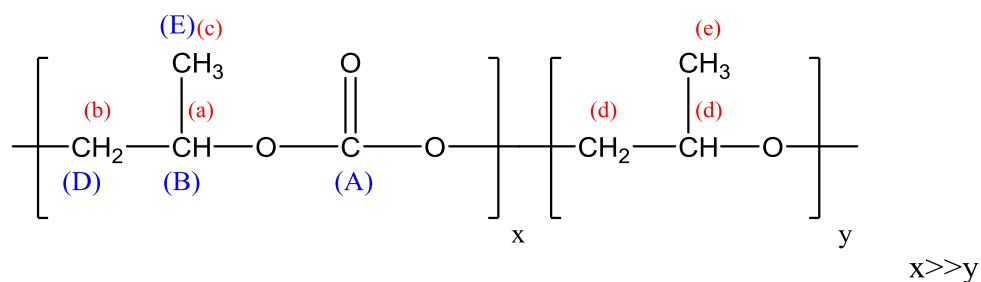


Figure 4.3 The chemical structure of PPC with carbon and hydrogen atoms labeled for referencing to NMR signals. The part on the left is polycarbonate, and the part on the right is polyether.

Residual polyether impurity is an unintended by-product in PPC synthesis [53-55]. Polyether may suppress PPC decomposition by disrupting the chain unzipping mechanism and consuming acid catalyst, and may contribute to residue after PPC decomposition [54, 113, 147]. Figure 4.4 shows the $^{13}\text{C-NMR}$ spectra obtained from neat QPAC 40 141K, neat Novomer 160K, and purified Novomer 160K. In Figure 4.4, the left column shows the full spectra, and the right column shows the high resolution spectra in the carbonate region. The triplet at 77.16 ppm was due to CDCl_3 which was used to calibrate the spectra.

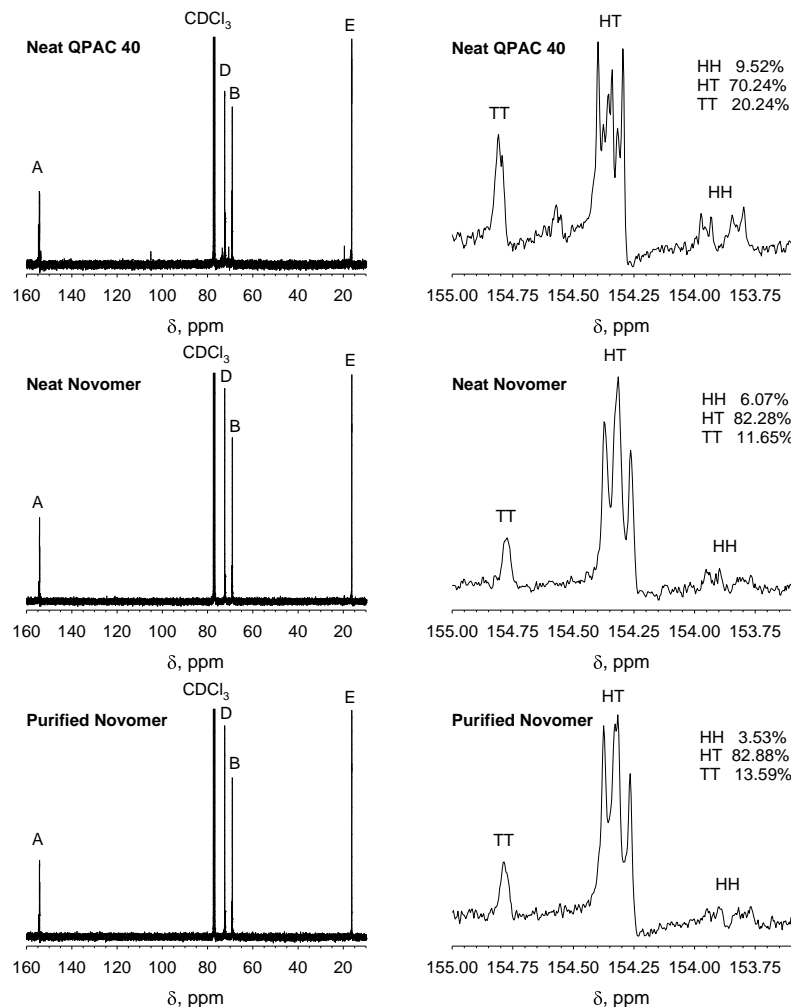


Figure 4.4 ^{13}C -NMR spectra for neat QPAC 40 141K (top), neat Novomer 160K (middle) and purified Novomer 160K PPC (bottom). The left column includes full spectra, and the right column includes the close-up spectra at the carbonate region.

The major peaks observed in ^{13}C -NMR spectra for all PPC types were assigned as follows: ^{13}C -NMR (CDCl_3 , δ , ppm), 16.3 (CH_3 , carbon E), 69.1 (CH_2CH , carbon B), 72.5 (CH_2CH , carbon D), 153.8-154.8 ($\text{O}(\text{C}=\text{O})\text{O}$, carbon A) [55, 148]. The QPAC 40 141K spectra had small peaks at 19.6 ppm, 70.7 ppm, 73.5 ppm, and 155.1 ppm due to propylene carbonate [149]. Propylene carbonate is a possible by-product of PPC synthesis [148, 150]. Propylene carbonate impurity in PPC can decrease PPC's glass

transition temperature (T_g) [54, 113, 147, 151]. No propylene carbonate peaks were observed in the neat and purified Novomer 160K spectra. A minor peak was observed in QPAC 40 141K spectrum at 105.1 ppm which might be due residual catalyst [149]. There appeared to be little or no difference between the spectra for purified and as-received for Novomer 160K.

The regioregularity of the PPC was compared in the high resolution spectra for the carbonate region, as shown on the right side of Figure 4.4. Depending on the synthesis, the PPC can be in head-to-head (HH), head-to-tail (HT) and tail-to-tail (TT) configuration [113, 150]. The terms HH, HT and TT refer to the termination groups (carbonate or propyl) in the polymer [113, 150]. A higher fraction of regioregular HT units corresponds to a higher glass transition temperature and improved mechanical strength. On the other hand, HH and TT regiostructures slow the rate of decomposition [113, 147]. For all PPC samples, the HH configuration had two peaks at 153.8 ppm and 153.9 ppm. The HT configuration was identified by multiple peaks between 154.3 ppm and 154.4 ppm, and the TT configuration was identified by a single peak at 154.8 ppm. The mole fraction of each configuration was calculated by integrating the area under the peaks and is shown in Figure 4.4. As-received Novomer 160K had more HT (88.28%) compared to QPAC 40 141K (70.24%). Comparing the as-received and purified Novomer 160K, the distribution of the configurations was similar within error.

The $^1\text{H-NMR}$ data is shown in Figure 4.5 for as-received QPAC 40 141K, as-received Novomer 160K, and purified Novomer 160K. $^1\text{H-NMR}$ was used to evaluate the polyether content. The major peaks were identified as follows: $^1\text{H-NMR}$ (CDCl_3 , δ , ppm), 1.31 (3H; CH_3 , hydrogen c), 4.18 (2H; CH_2CH , hydrogen b), 4.98 (1H; CH ,

hydrogen a), 1.15 (3H;CH₃, hydrogen e), 3.40-3.90 (2H;CH₂, hydrogen d). The peak located at 1.68 ppm was assigned to pyrrolidine, an impurity in the NMR solvent [119]. Since both polyether and polycarbonate have 6 hydrogens, the mole percent of polyether content was calculated as $(d+e)/(a+b+c+d+e)*100$. As seen in Figure 4.5, as-received QPAC 40 141K had a larger polyether content (~5%) compared to as-received Novomer 160K (~0.5%). The polyether content of Novomer 160K was essentially unchanged by purification (0.51% before and 0.67% after purification). The minor peaks observed at 1.48 ppm, 4.01 pm, 4.54 ppm and 4.84 ppm were identified as propylene carbonate [149]. The as-received QPAC 40 141K had a larger propylene carbonate content compared to as-received Novomer 160K. This finding is consistent with the ¹³C-NMR result described above. A small peak at 5.29 ppm due to methylene chloride was observed only in the as-received QPAC 40 141K spectrum [149]. Methylene chloride can be used to remove propylene carbonate and catalyst after PPC synthesis [150]. Spencer et al. previously showed that residual methylene chloride in PPC lowers the decomposition temperature [113]. Thus, the increase in thermal stability of purified QPAC 40 141K compared to the as-received material could be due in-part to methylene chloride removal.

The TGA and NMR measurements show that Novomer 160K has a lower decomposition temperature, less polyether content, high HT ratio, and fewer impurities, such as propylene carbonate, catalyst and residual solvent than QPAC 40 141K. Thus, Novomer 160K was the material used as the sacrificial polymer in the air-gap experiments along with BCB as the overcoat and pattern-transfer material.

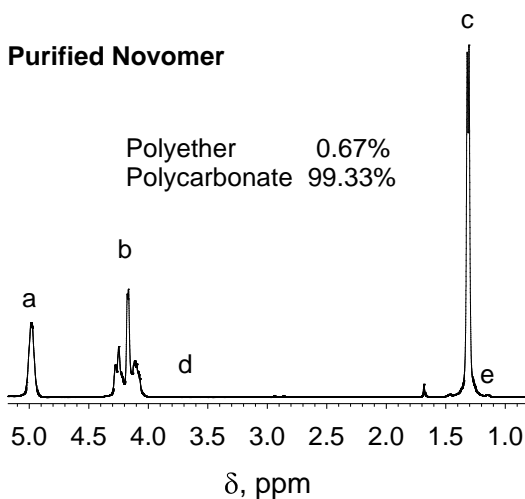
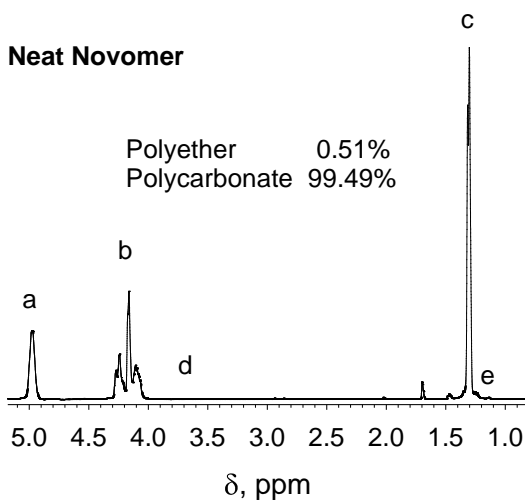
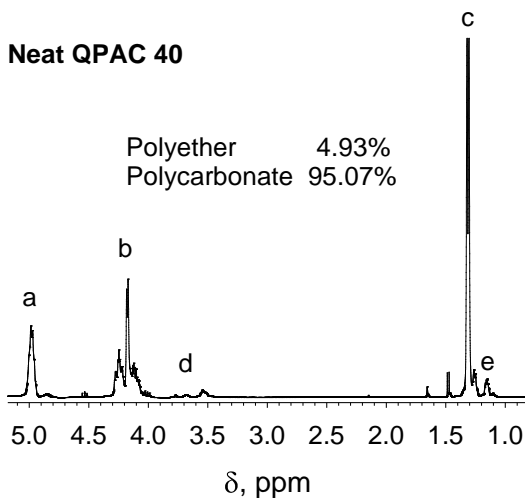


Figure 4.5 ^1H -NMR spectra for neat QPAC 40 141K (top), neat Novomer 160K (middle), and purified Novomer PPC 160K (bottom)

The air-gap formation involves two simultaneous thermal processes, namely PPC decomposition and BCB curing. That is, the thermal treatment decomposes the PPC, converting solid PPC to gas, and cures the BCB which results in a more rigid overcoat. Thus, the first step was to find a thermal treatment sequence where the BCB could be cured and PPC could be decomposed in such a way to create stable, reliable, enclosed cavities. Samples prepared with 10 μm non-photosensitive PPC, 3 μm BCB for pattern-transfer layer, and 7 μm BCB for overcoat layer were subjected to various thermal treatments. Different thermal treatments were surveyed separately on the samples to understand the effect of thermal treatments on air-gap formation: (i) single-step low temperature (26.5 hr at 190°C), (ii) single-step high temperature (4 hr at 250°C), (iii) constant 1 wt%/min PPC decomposition rate achieved by ramping the temperature at a specific rate [152], and (iv) two-step thermal treatment (2 hr at 190°C and 1 hr at 280°C). These experiments with different thermal treatment parameters showed that BCB must be cured to an appropriate extent before PPC decomposition is initiated, so that BCB has sufficient mechanical strength to withstand the pressure generated in the enclosed cavity during PPC decomposition. A two-step thermal treatment was found to be an optimal thermal treatment sequence. In the first step, BCB is cured at a lower temperature so that sufficient mechanical strength is achieved, and in the second step PPC is decomposed at a higher temperature so as to produce a clean cavity.

The BCB curing step in the two-step thermal treatment sequence is critical to obtaining reliable air-gap structures. The thermal treatment should be selected as to provide relatively fast BCB curing compared to PPC decomposition in a reasonable amount of time. In order to determine the optimal BCB curing recipe, the kinetics of

BCB curing and PPC decomposition processes were investigated. The kinetic parameters for PPC decomposition were calculated from isothermal PPC decomposition data obtained between 190°C and 220°C with 10°C intervals using TGA. The data were analyzed using first-order integral method where an Arrhenius-type relationship was assumed for the reaction rate. The calculated activation energy and frequency factor were 179.8 kJ/mol and $2.93 \times 10^{15} \text{ s}^{-1}$, respectively (R^2 of ~0.85). The percent BCB curing with time data was extracted from the oven curing data sheet of Cyclotene 4000 series between 170°C and 220°C with 5°C intervals [117]. In order to understand the relative rates of the two processes, the kinetic profiles of both processes were compared at temperatures between 170°C and 220°C. Figure 4.6 shows the percentage change in the processes plotted against time, i.e. the percent BCB cure and percent PPC undecomposed, at 170°C, 190°C and 210°C. The relative rates of the processes can be inferred by comparing the percentage change in the processes. At the low temperatures, BCB curing occurred faster than PPC decomposition. For example at 170°C, the BCB curing increased from 55% to 74% (i.e. 19% change), while PPC decomposition resulted in a change in mass from 98% to 91% (i.e. 7% change) (Figure 4.6a). That means the BCB cures faster than PPC decomposes at 170°C. At higher temperature, e.g. 210°C, the situation is reversed and PPC decomposition is slightly faster than BCB curing. PPC decomposition changed by 15% (98% to 83%), whereas BCB curing changed only by 13% (70% to 83%) at 210°C (Figure 4.6c).

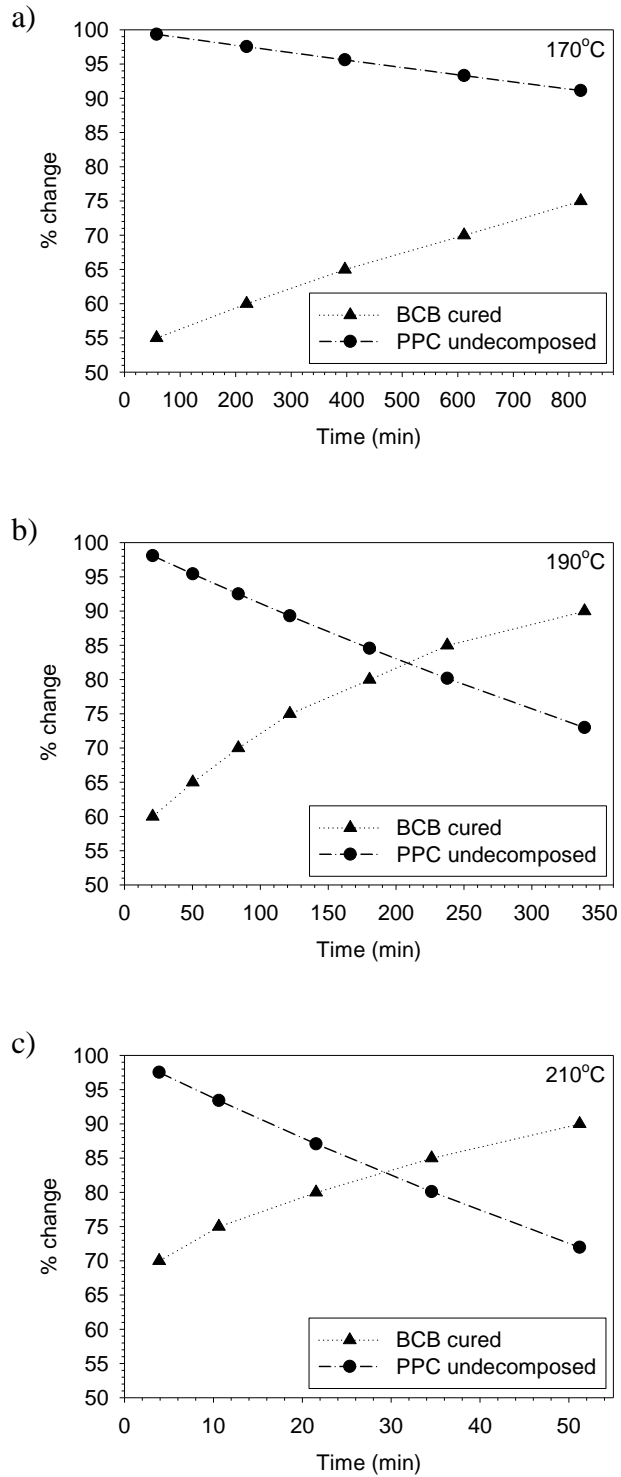


Figure 4.6 Kinetic comparison between BCB curing and PPC decomposition processes at (a) 170°C, (b) 190°C, and (c) 210°C

A target cure condition of 70% for the BCB was judged by trial and error experiments to be sufficient for withstanding the pressure developed from the PPC decomposition. Figure 4.6 was used to find the curing conditions for BCB. 190°C was the optimal temperature for BCB curing because the 70% BCB cure point can be reached in 1.3 hr. At lower temperature, such as 170°C, it takes an extended period of time, 10 hr, to reach the 70% BCB cure point. At higher temperature, such as 210°C, the required time for 70% BCB curing is only 4 min which is hard to control and the PPC decomposition rate becomes too rapid. Thus, 190°C for 1.3 hr for BCB curing was selected as the first part of the two-step process.

The RIE patterning process for PPC was investigated with the goal of achieving reliable air-gap formation. In order to understand the effect of PPC thickness and the BCB-to-PPC thickness ratio needed for air-gap stability, three samples with different PPC and BCB thicknesses were prepared. The PPC thickness was 11.8 μm (“thin”), 19.3 μm (“medium”) or 28.9 μm (“thick”). The total BCB thicknesses (pattern-transfer layer plus overcoat layer) were 11.8 μm , 14.8 μm and 17.1 μm , for thin, medium and thick PPC samples, respectively. A two-step thermal treatment for BCB-cure and PPC-decomposition was used for all samples where the first step was 1.3 hr at 190°C as described above, and the second step for PPC decomposition and final BCB cure was at 240°C. The air-gaps obtained with the thick PPC samples after 10 hr at second part of the thermal treatment had a cracked BCB layer and were judged unacceptable. The BCB-to-PPC thickness ratio was 0.59 in the thick PPC sample (i.e. the BCB thickness includes both the pattern-transfer layer and the overcoat BCB layer). Acceptable air-gaps were obtained with the medium and thin PPC samples because the BCB-to-PPC thickness ratio

was larger than that in the thick sample, i.e. ratio of 0.77 for the medium and 1 for the thin sample.

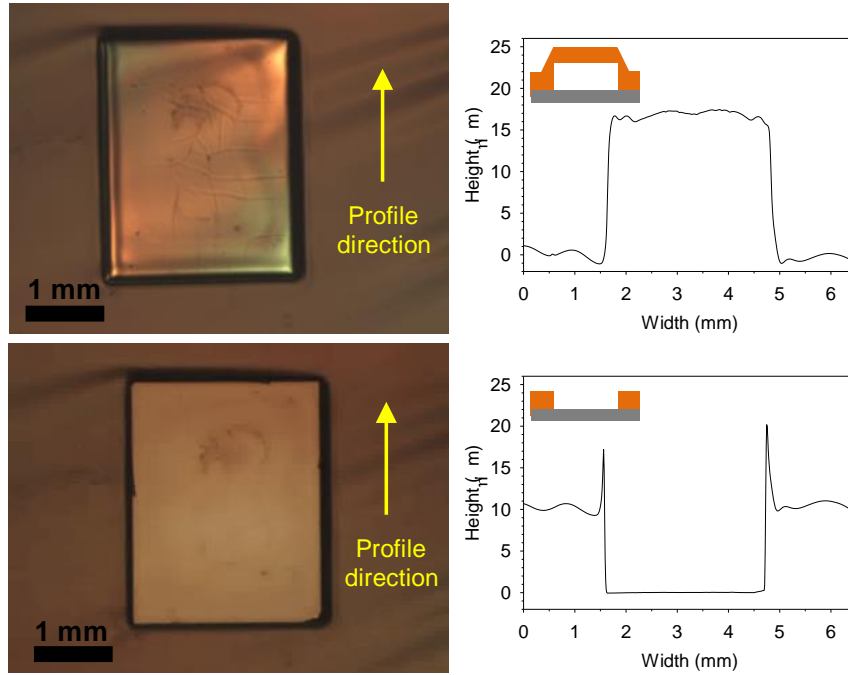


Figure 4.7 Top-view optical images and Dektak profiles of a 2.5x3.2 mm air-gap feature obtained from a medium thick non-photosensitive PPC sample subjected to two-step thermal treatment of 1.3 hr at 190°C and 11 hr at 240°C. All data was acquired after PPC decomposition. The optical image and Dektak profile on top were acquired before removal of BCB cap, and the optical image and Dektak profile at the bottom were obtained after removal of BCB cap. Dektak profile on top was leveled with respect to overcoat BCB layer, and Dektak profile at the bottom was leveled with respect to Si surface. The small schematics on each Dektak profile show the cross-section of the features from which Dektak profiles were obtained from.

Figure 4.7 shows optical images and surface profiles for the medium thickness PPC sample after 11 hr of thermal treatment at 240°C. As seen from the profile, the BCB cap was not perturbed in the middle after the air-gap was formed (top optical image and profile are shown in Figure 4.7). That is, the BCB overcoat did not bulge or collapse. After the BCB cap was removed, the optical image showed little-to-no sign of residue in

the air-gap region (bottom optical image). No spikes were seen in the surface profiles (bottom profile in Figure 4.7). This means that the residue layer was insignificant on the scale shown in Figure 4.7. The results for the thin PPC sample were similar to the ones with medium thickness PPC showing no visible residue in the air-gap region and no deformation of the BCB cap. The air-gap yield in both medium and thin PPC samples was about 80-90% with minor imperfection in the others from process defects.

The residue thickness on the silicon substrate in the cavity region was investigated using XPS depth profiling to understand the dependence of residue thickness on thermal decomposition time. The medium and thin PPC samples were decomposed for different time periods, and the residue thickness was measured immediately after removal of the BCB cap. Figure 4.8 shows a representative XPS depth profile obtained from the medium thickness PPC sample subjected to a 13 hr of second step thermal treatment.

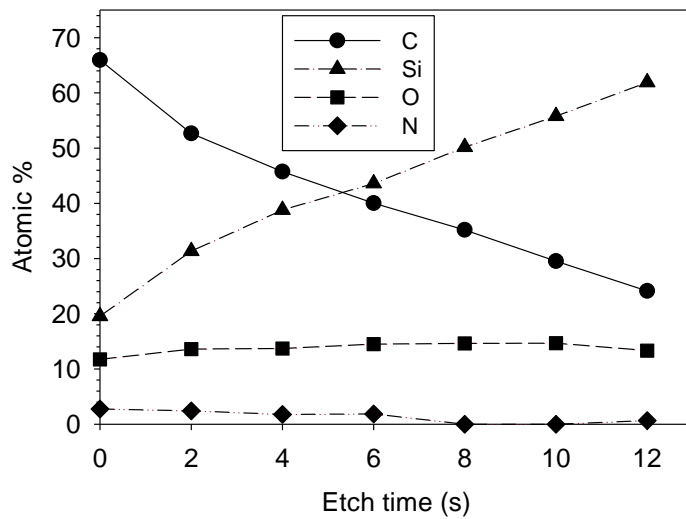


Figure 4.8 An XPS depth profile obtained from the air-gap region of a medium thick non-photosensitive PPC sample with initial PPC thickness of 19.3 μm subjected to a two-step thermal treatment of 1.3 hr at 190°C and 13 hr at 240°C

The residue mainly contained C and O. A small amount of N was also detected. The Si signal was from the Si substrate. The concentration of C and N decreased with depth as the Si concentration increased. The same species and similar trends were observed for the other samples. The medium thickness PPC samples were thermally treated for 11 hr, 13 hr and 15 hr as the final step in the two-step thermal treatment. For each medium thickness PPC sample, the residue thickness was obtained from two different air-gap features. The residue thicknesses were 19.2 nm and 59.9 nm for the 11 hr thermal treatment, 12.9 nm and 29.9 nm for the 13 hr thermal treatment, and 1.7 nm and 17.5 nm for the 15 hr thermal treatment. The residue thicknesses from the thin PPC sample were 34.5 nm for the 5 hr thermal treatment, 23.2 nm for the 6 hr thermal treatment and 26 nm for the 7 hr thermal treatment. The thickness of the residue decreased with thermal treatment time. The removal of residue was slower than the removal of residue for the neat PPC sample without overcoat.

The direct photopatterning process using a photoacid generator (PAG) in the PPC film was investigated. A 19.9 μm thick photosensitive PPC film with 3 wt% PAG was prepared and overcoated with 12.4 μm BCB. The sample was subjected to the two-step thermal treatment consisting of 1.3 hr at 190°C and 11 hr at 240°C. No air cavities were formed because the PAG was thermally activated at ca. 180°C leading to the decomposition of PPC at lower temperatures compared to the non-PAG containing PPC film. The lower temperature PPC decomposition occurred before the BCB became sufficiently rigid.

The direct photopatterning process was optimized to produce reproducible air-gap structures. First, in order to ensure the BCB was sufficiently rigid before substantial PPC

decomposition, the two-step thermal treatment (previously 1.3 hr at 190°C and 11 hr at 240°C) was modified as follows. An initial thermal treatment step at 150°C was added, resulting in a three-step thermal treatment. The temperature of the second step was lowered to 180°C from 190°C. Thus, the modified thermal treatment included treatments at 150°C, 180°C and 240°C. Also, the amount of PAG in the PPC film was lowered by using a two-layer PPC film. One of the two layers had PAG and the other one did not, as shown in Figure 4.9. The two-layered PPC film was previously shown to decrease the amount of PAG-related residue [56].

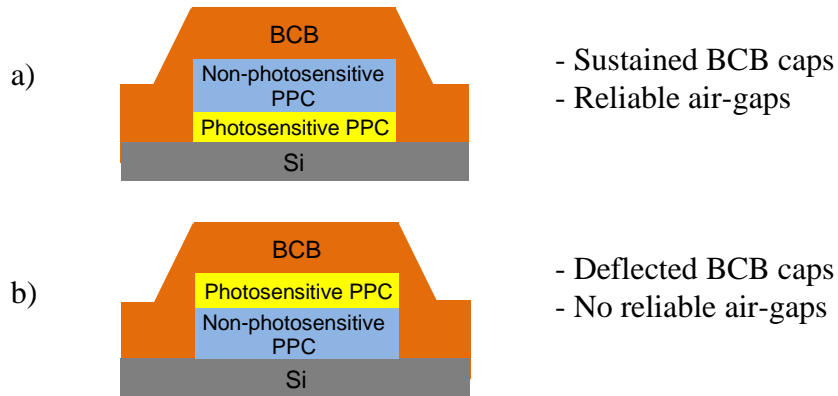


Figure 4.9 The configurations of two-layer PPC film for direct photopatterning process, where (a) photosensitive PPC layer is at the bottom, and (b) photosensitive PPC layer is on top

Reproducible air-gap structures were obtained using the two-layer PPC film where the PAG-loaded PPC was the bottom layer and the non-photosensitive PPC was the top layer, as seen in Figure 4.9a. Two samples were coated with 2.8 μm of PAG-containing PPC. Then, one sample was coated with 13.6 μm non-photosensitive PPC, and the other sample was coated with 23.5 μm non-photosensitive PPC. The BCB overcoat thickness on the samples was 13 μm and 16 μm , respectively. The samples were taken

through the three-step thermal treatment consisting of 15 hr at 150°C, 15 hr at 180°C, and 11 hr at 240°C. The resulting air-gap structures showed no deflection in BCB caps regardless of total PPC thicknesses because the non-photosensitive PPC making up most of the PPC film did not decompose before the BCB was cured. Duplicate samples were thermally treated for 30 hr at 150°C, 30 hr at 180°C, and 11 hr at 240°C. A greater air-gap yield (~80% vs. ~50%) was obtained for the longer treatment times (30 hr vs. 15 hr) because the BCB reached a greater extent of cure. On the other hand, no air-gaps were obtained using the two-layer PPC film when the PAG-loaded PPC was the top layer and non-photosensitive PPC was the bottom layer (Figure 4.9b). A non-uniform residue was visually observed in the air-gap region of the in all the PAG-containing samples. The residue thickness in the samples using the two-layer PPC film shown in Figure 4.9a was much less than when all the PPC contained PAG.

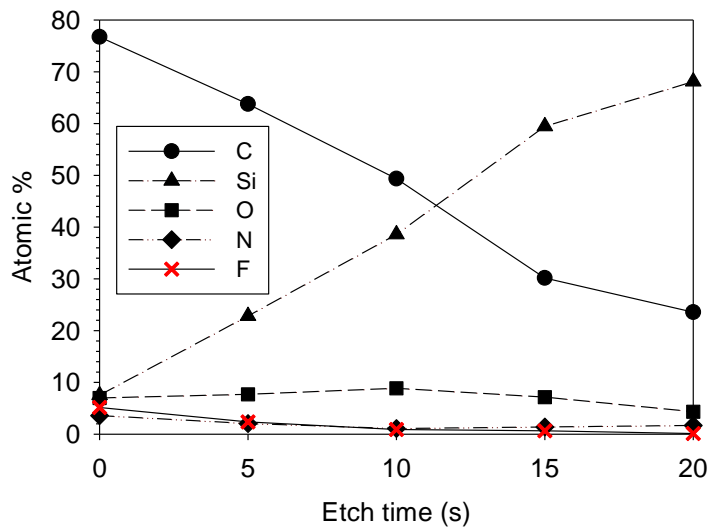


Figure 4.10 An XPS depth profile obtained from the air-gap region of a two-layer PPC sample with initial photosensitive (PAG-loaded) PPC at the bottom (2.8 μm), and non-photosensitive PPC on top (23.5 μm) subjected to a three-step thermal treatment of 30 hr at 150°C, 30 hr at 180°C and 11 hr at 240°C

Figure 4.10 is a representative XPS depth profile showing the distribution of Si, C, O and N with depth. The elemental distribution is similar to the profile shown in Figure 4.8 except that F is present due to its presence in the PAG [53]. On average, the measured minimum residue thickness for the two-layered PPC structure was at least 1.5 to 2 times greater than that for the PAG-free sample prepared by the RIE process.

Thus, the addition of PAG simplifies the process because the RIE patterning step is eliminated, however it results in a greater amount of residue due to the salt products of the PAG [53, 54]. The two-layer PPC photopatterning process using PAG in only one layer is a significant improvement over the fully PAG-loaded PPC approach. The amount of residue was reduced and the photopatterning was significantly crisper because excess PAG is eliminated restricting the amount diffusing into neighboring regions. Producing a two-layer PPC structure is challenging because spin-coating the second layer redissolves part of the first layer.

The carbon content of the PPC residue on the silicon were characterized by high resolution XPS (carbon peaks (C1s)). Two 20 μm thickness PPC films on silicon were prepared. One sample was coated with non-photosensitive PPC, and the other was coated with PAG-containing photosensitive PPC. The samples were thermally treated for 1.3 hr at 190°C and 10 hr at 240°C. The high resolution C1s peaks were deconvoluted and the results are shown in Figure 4.11 and Table 4.1 for non-photosensitive PPC residue, and Figure 4.12 and Table 4.2 for photosensitive PPC residue.

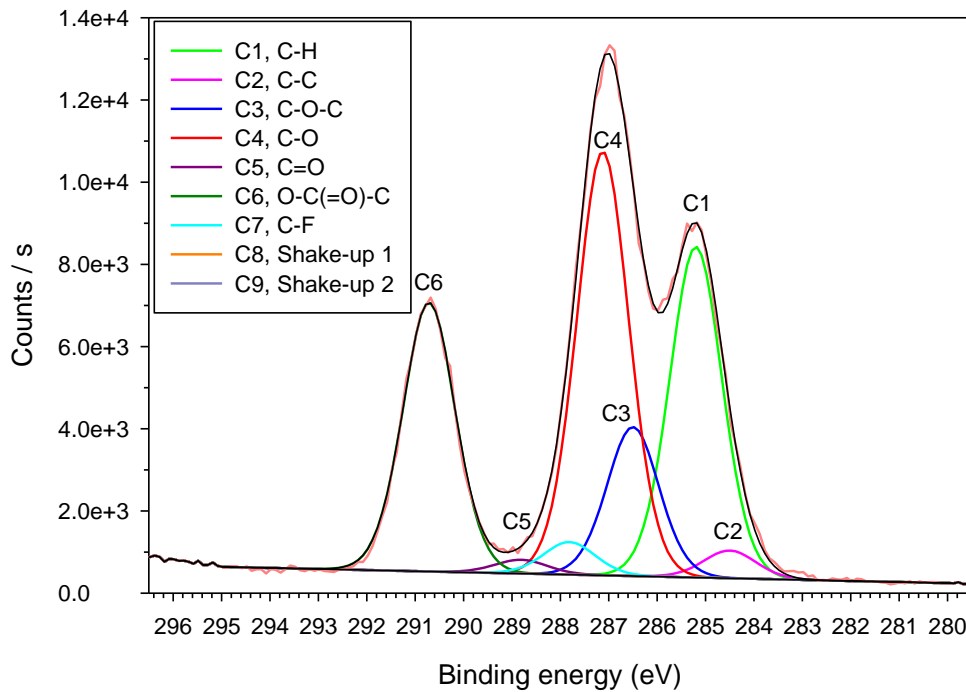


Figure 4.11 High resolution XPS scan, peak fit and peak deconvolution of C1s peaks obtained from non-photosensitive PPC residue

Table 4.1 Carbon functionalities in non-photosensitive PPC residue

Functionality	Peak Position (eV)	FWHM (eV)	Line Shape	% Area	% St. dev.
C-H	285.20	1.267	GL(30)	26.54	1.27
C-C	284.50	1.267	GL(30)	2.22	0.84
C-O-C	286.50	1.267	GL(30)	11.95	3.12
C-O	287.12	1.267	GL(30)	34.00	3.23
C=O	288.81	1.267	GL(30)	1.10	0.47
O-C(=O)-C	290.72	1.267	GL(30)	21.57	0.41
C-F	287.81	1.267	GL(30)	2.61	2.79
Shake-up 1	291.81	1.267	GL(30)	0.00	0.00
Shake-up 2	294.10	1.267	GL(30)	0.00	0.01

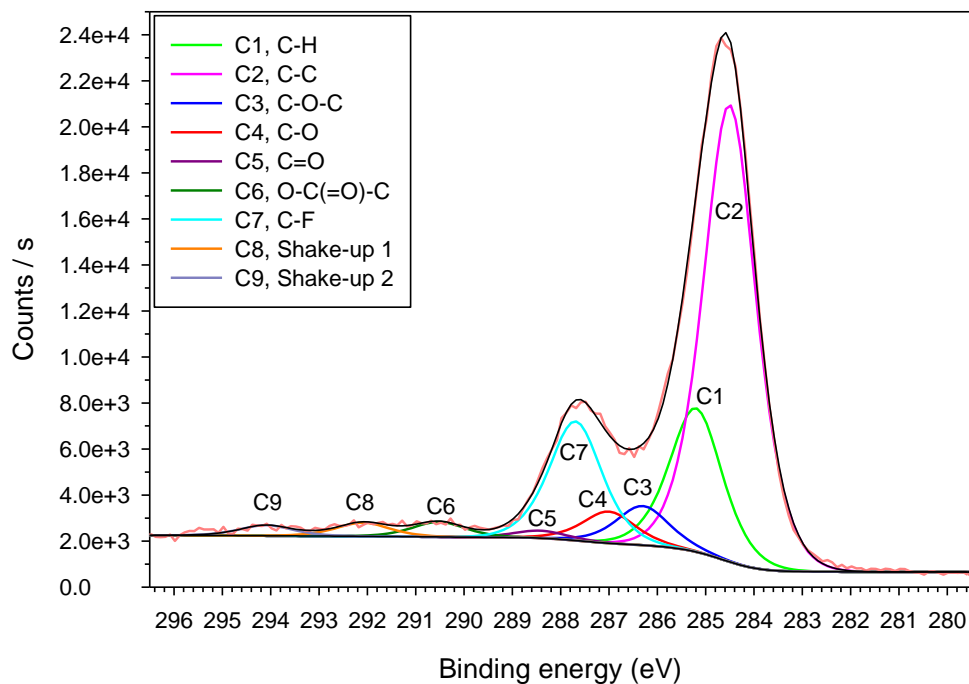


Figure 4.12 High resolution XPS scan, peak fit and peak deconvolution of C1s peaks obtained from photosensitive PPC residue

Table 4.2 Carbon functionalities in photosensitive PPC residue

Functionality	Peak Position (eV)	FWHM (eV)	Line Shape	% Area	% St. dev.
C-H	285.20	1.283	GL(60)	17.16	2.24
C-C	284.50	1.283	GL(60)	54.58	2.98
C-O-C	286.30	1.283	GL(60)	4.68	1.07
C-O	287.00	1.283	GL(60)	3.77	2.54
C=O	288.42	1.283	GL(60)	0.89	1.13
O-C(=O)-C	290.52	1.283	GL(60)	1.80	0.45
C-F	287.69	1.283	GL(60)	14.22	1.27
Shake-up 1	292.09	1.283	GL(60)	1.63	0.46
Shake-up 2	294.10	1.283	GL(60)	1.26	0.57

The non-photosensitive PPC residue had peaks corresponding to the binding energy of C-C, C-H, C-O-C, C-O, C=O, and O-C(=O)-C, as shown in Figure 4.11 and Table 4.1. The non-photosensitive PPC residue had a higher concentration of oxygen-containing carbon moieties. This may be indicative of residue containing undecomposed PPC. The photosensitive PPC had all moieties contained in the non-photosensitive PPC residue and three additional peaks corresponding to C-F and two shake-up peaks, as shown in Figure 4.12 and Table 4.2. The presence of F in the residue is from the PAG (14.22 ± 1.27 mol%). The shake-up peaks were due to π - π^* excitation in the aromatic rings in the PAG structure [122, 123]. The PAG-containing PPC residue had a higher concentration of C-C species. This suggests that the major residue contribution was from the anion portion of the PAG [53, 54].

To better understand the stiffness achieved in the BCB overcoat layers in the air-gap structures, the bulge equation shown in Equation 4.1 was used [153].

$$P = \frac{3.393ht\sigma_0}{a^2} + \frac{4h^3Et}{3a^4(1-\nu^2)} \quad (4.1)$$

P is the applied pressure on the membrane, E is the elastic modulus, σ_0 is the residual stress, and ν is Poisson's ratio, h is the vertical deflection of the membrane, t is the membrane thickness and a is the radius of the membrane [153]. The deflection due to pressure has two contributions. The first group of terms on the right-hand side of Equation 4.1 is due to prestressing the membrane and the second set is due to an unstressed membrane.

Nanoindentation measurements were performed on BCB cap of an air-gap feature to obtain the pressure versus deflection values. A circular air-gap structure, 2 mm diameter, was prepared with non-photosensitive PPC decomposed for 1.3 hr at 190°C and 4 hr at 240°C. The air-gap height was 9 μm , and the BCB thickness was 10 μm (3 μm pattern-transfer layer and 7 μm overcoat layer). The maximum force and the resulting deflection was 100.23 μN and 0.64 μm , respectively. The applied pressure (P) on the membrane was calculated to be 31.904 Pa. Poisson's ratio was 0.34 [118], and the elastic modulus of the BCB was calculated to be 2.3 GPa from nanoindentation measurement done on a BCB-only sample (no air-gap). It was found that the major contribution to the pressure was from the residual stress portion of Equation 4.1 (31.895 Pa), compared to the unstressed portion (0.009 Pa). This shows that the residual stress in the BCB cap increases the bending stiffness and provides the majority of the mechanical strength in the air-gap region. The residual stress in the BCB cap was calculated to be 1.46 MPa, tensile, and mostly originating from the thermal expansion of BCB, 52 ppm/K, versus the silicon substrate, 2.6 ppm/K [114].

The mode of PPC decomposition was observed visually and with surface profilometry. During decomposition of the PPC, the BCB overcoat is deflected downward and held in contact with a liquidus PPC, which is above its glass transition temperature during the decomposition process. Once the PPC converts to the gas phase, the BCB is released and returns to the planar configuration due to the internal stress in the BCB. Other overcoat materials which are not prestressed would more easily deflect downward or upward.

4.2 Summary and Conclusions

In this study, the polymer-based air-gap formation processes, and the chemical properties of polymer residue have been investigated. A thermally degradable sacrificial polymer, PPC, was used for creating air-gaps around enclosed regions encased with an overcoat polymer. Two different PPC materials were compared using TGA and NMR analysis. A precipitation-based PPC purification was used to remove some impurities. BCB was used as the overcoat material. A kinetic comparison of PPC decomposition and BCB curing was used to optimize the thermal treatment. A two-step thermal treatment was used to form air-cavities. The PPC was patterned by RIE or photopatterning using a PAG. Less residue was obtained with the non-photosensitive PPC. Adding PAG to the PPC allowed direct photopatterning but also increased the residue and restricted the heating conditions due to thermally generated acid catalyzing the PPC decomposition. The amount of residue from the PAG-loaded PPC was 1.5 to 2 times greater than the PPC-only films. The PAG-loaded PPC residue contained a greater C-C content than the residue from pure PPC. Nanoindentation measurements showed an increased BCB bending stiffness due to its residual stress.

CHAPTER 5

THERMAL AND PHOTOCATALYTIC STABILITY ENHANCEMENT MECHANISM OF POLY(PROPYLENE CARBONATE) DUE TO COPPER(I) IMPURITIES

In this study, the details of the change in thermal stability with contact to copper have been investigated. It is proposed that rather than the copper ions interacting with PPC, a copper-PAG interaction occurs. X-ray photoelectron spectroscopy (XPS) was used to identify the oxidation state of the dissolved copper as Cu(I). A general mechanism for thermal stability is proposed in which copper ion interacts with iodonium moiety of the Rhodorsil-FABA PAG forming a Cu(I)-I complex so as to inhibit acid creation, thus leading to the apparent increase in the stability of the PPC. The mechanism and interaction with the iodonium-based PAG were tested by examining the thermal decomposition of PPC films with three iodonium-based PAGs and two sulfonium-based PAGs.

5.1 Results

It was previously shown that the oxidation and dissolution of trace amounts of copper in the PPC is essential for observed thermal stability increase [74]. However, the oxidation state of the dissolved copper, which is important in determining the role of copper, was not identified. XPS analysis was used here to determine the oxidation state of the copper in the PPC film after the copper was incorporated into it.

An experiment was done in order to understand the copper oxidation event. A small amount of copper nano-powder was added to the PPC/Rhodorsil-FABA PAG solution. The solution was mixed by ball-milling for two days and then the solution was left for 3 weeks. The solution color turned from colorless to turquoise after 3 weeks indicating the presence of copper ions. The most probable oxidizing agent in the PPC/PAG solution is dissolved oxygen from air. Even if there was a small amount of PAG decomposition over time creating an acid, hydrogen ions do not have a suitable redox potential for copper oxidation, unless a ligand is present for copper complexation.

The sample used for XPS analysis was prepared by spin-coating a copper surface with a PPC/Rhodorsil-FABA PAG solution, and allowing the copper to oxidize and dissolve into the PPC, as explained in the Experimental section. The XPS spectra obtained from the surface of the sample are shown in Figure 5.1. The full XPS scan in Figure 5.1 shows the presence of Cu, F, O, and C, as expected. The intensity of the Cu peak is very small since there are only trace amounts present in the PPC film. The atomic and mass percentages of the elements in Figure 5.1 are shown in Table 5.1. There was no iodine identified because of its low concentration in the mixture. One can see from the relative intensity of the fluorine peak that iodine would have a very low intensity peak because the atomic ratio of I-to-F is 1:20 (see PAG structure in Table 2.1). The peak binding energies in the Cu scan are 933.18 eV and 952.88 eV, as shown in Figure 5.2, corresponding to Cu(I) [154-159]. No Cu(II) peaks were identified. Cu(I) is stable in the presence of an oxidizing agent like oxygen only when it is complexed because it is easier to oxidize Cu(I) to Cu(II) than it is to oxidize Cu(0) to Cu(I). Thus, once Cu(0) is oxidized to Cu(I), it is immediately oxidized to Cu(II), unless Cu(I) is stabilized by a

complexing agent. The presence of an iodide-containing species in the mixture was considered as a possible source of a suitable complexing agent for Cu(I) [160]. There are no other obvious choices of ligands for stabilizing Cu(I) in the mixtures used in this study. It is also noted that the concentration of Cu(I) in the film observed previously is about the same as that of the iodonium-based PAG in the mixture [74]. Thus, we conclude that the most likely form of copper dissolved in the PPC/PAG mixture is a Cu(I)-I complex. If this hypothesis were true, then the thermal stability effect of the PPC on a copper surface would be specific to an iodonium-based PAG, and it would not be observed with other PAGs (non-iodonium ones) or other acids.

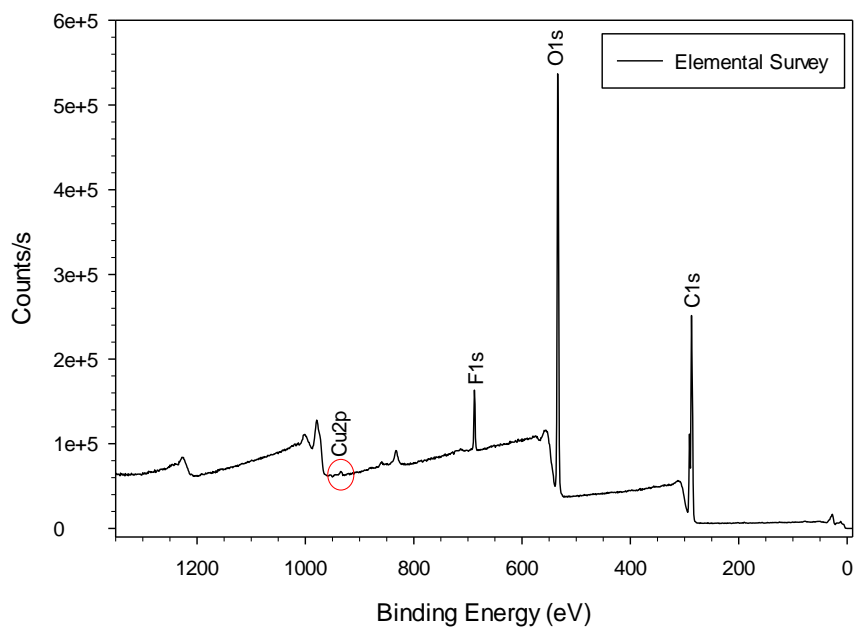


Figure 5.1 XPS elemental survey scan of surface of a PPC film cast on copper surface, UV exposed, and post-baked

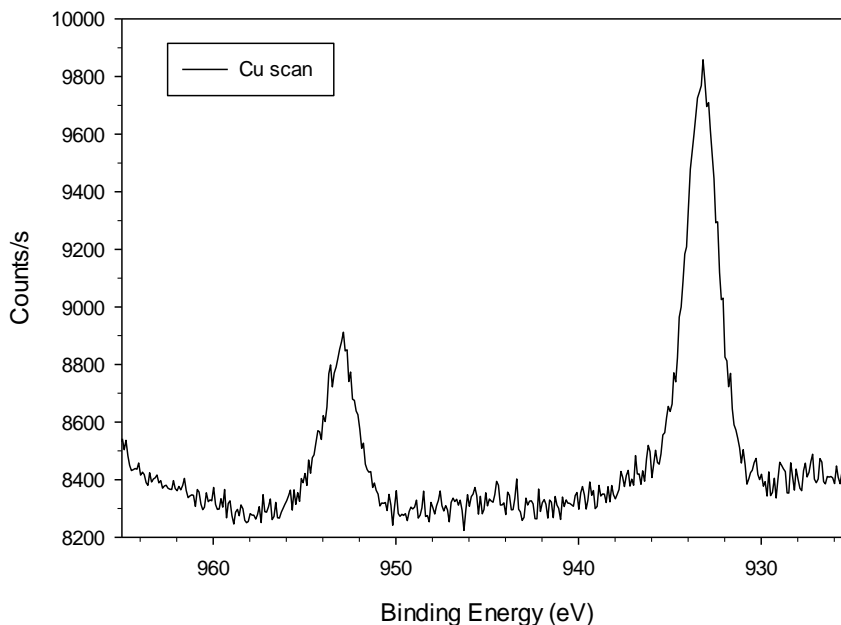


Figure 5.2 High resolution XPS Cu scan on surface of a PPC film cast on copper surface, UV exposed, and post-baked

Table 5.1 XPS analysis results for elements and relative percentages

Element	Atomic percent	Weight percent
Cu	0.06	0.28
F	3.62	4.99
O	37.43	43.45
C	58.86	51.29

To test the iodonium-specific copper/PAG interaction, mixtures with sulfonium-based PAGs were investigated. Sulfonium-based PAGs also produce a strong acid, which can be used to catalytically decompose polycarbonates [53]. Two sulfonium-based PAGs, TAPSPS-FABA and TAPSPS-TMM, whose structures are shown in Table 2.1, were investigated in the decomposition experiments. The two sulfonium-based PAGs have the same cations with different anions. Since the strength of the acid is related to conjugate base formed (i.e. the anion part of the PAG), the effect of a different anion was

investigated. In addition, the anion in TAPSPS-FABA is the same as that in Rhodorsil-FABA. This allows a direct comparison of the cation effect. The sulfonium-based PAGs have a higher molecular weight than Rhodorsil-FABA. The mass loading of the sulfonium-based PAGs in the PPC/PAG solutions were adjusted so as to maintain the same PAG-to-PPC mole ratio as used in the Rhodorsil-FABA solutions.

The TGA results for the PPC films containing sulfonium-based PAGs are shown in Figure 5.3 and Figure 5.4. The set of TGA results follows a consistent pattern and they are discussed together. The sample which was prepared by solvent casting the PPC/sulfonium-based PAG solution onto copper-sputtered substrate followed by UV exposure was labeled “Cu Exposed”. A similar sample was prepared but on a silicon substrate and labeled “Si Exposed”. UV irradiation of the PAG creates an acid which catalyzes the decomposition of PPC lowering the decomposition temperature for the PPC. The decomposition of neat PPC, labeled “PPC”, is also shown in Figure 5.3 and Figure 5.4. 50% weight loss temperature was taken as the characteristic temperature for decomposition. The value for the UV-exposed samples on copper and silicon was about 100°C. It is important to note that there is almost no difference in the decomposition profiles for the Si Exposed and Cu Exposed samples here, contrary to the case of the iodonium-based PAG solution. If the cause of the temperature shift on the copper surface was an acid-only effect, then the TGA results with sulfonium-based PAGs would be similar to those of the iodonium-based PAGs. On the other hand, if the interaction of the copper is with the iodide in the PAG, the presence of Cu(I) in the PPC/sulfonium-based PAG film would have no impact on thermal stability, which it doesn't, as shown in Figure 5.3 and Figure 5.4.

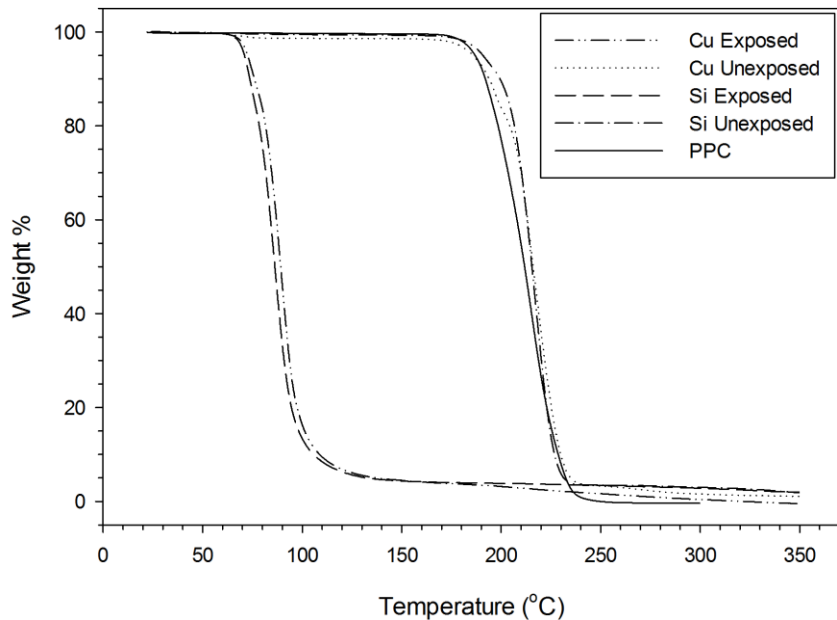


Figure 5.3 TGA results for PPC film containing sulfonium-based PAG TAPSPS-FABA

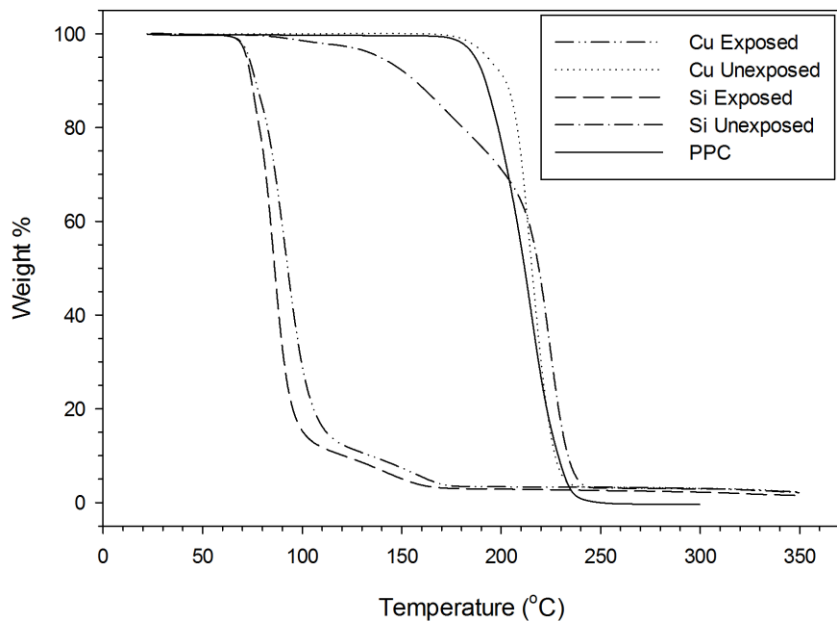


Figure 5.4 TGA results for PPC film containing sulfonium-based PAG TAPSPS-TMM

The samples prepared by solvent casting PPC/sulfonium-based PAG solutions onto copper-sputtered or silicon substrates without UV irradiation are labeled “Cu Unexposed” and “Si Unexposed” in both Figure 5.3 and Figure 5.4, respectively. In the absence of UV-exposure, PAG thermally decomposes to produce an acid which catalyzes the decomposition of PPC. In other words, the decomposition temperature of the PPC films in the unexposed cases is dictated by the PAG decomposition temperature, as shown previously by Spencer et al. [74]. In Figure 5.3 and Figure 5.4, it is seen that the unexposed samples decomposed around 210°C, except for the initial lower decomposition temperature observed in the Si Unexposed case for TAPSPS-TMM, seen in Figure 5.4. Since neat PPC also decomposed at 210°C, it is concluded that PAG decomposition does initiate the PPC decomposition at the lower decomposition temperatures of the TGA scan. More importantly, there is almost no difference in decomposition temperature between the Cu Unexposed and Si Unexposed cases, supporting the hypothesis that the iodide in the iodonium-based PAGs is the species that interacts with Cu(I) leading to thermal stability improvement for PPC.

The set of sulfonium-based PAGs show that copper has virtually no effect on the PPC decomposition temperature. There were small increases in decomposition temperature observed for some of the cases. For example, for TAPSPS-FABA, there was about 5°C increase in both copper and silicon unexposed cases relative to neat PPC and a 3°C increase in the Cu Exposed case relative to Si Exposed case. For TAPSPS-TMM, there were 5°C and 8°C increases in the copper and silicon unexposed cases relative to neat PPC. There was also a 6°C increase in Cu Exposed case relative to the Si Exposed case. These increases are small and can be caused by a variety of experimental conditions

in the TGA, such as sample contact with the TGA pan. These temperature shifts are insignificant compared to the increases observed by Spencer et al. for the iodonium-based PAG [74]. For that reason, it is reasonable to conclude that there is no significant thermal stability increase observed due to a copper interaction in the exposed and unexposed cases for the sulfonium-based PAGs. Moreover, since the anions of the Rhodorsil-FABA and TAPSPS-FABA are the same, another conclusion is that the thermal stability increase due to copper is directly related to the cation portion of the PAG and not the anion. This supports the idea that iodide is an essential component in the copper-induced suppression of the decomposition in the PPC/PAG films.

In order to confirm that copper-induced PPC decomposition is specific to the iodonium-based PAGs, three iodonium-based PAGs, BTBPI-TF, BTBPI-NF and DPI-TF, whose structures are shown in Table 2.1, were used in the PPC decomposition experiments. BTBPI-TF and BTBPI-NF have the same cation, whereas BTBPI-TF and DPI-TF have the same anion. In addition, the cation portion of BTBPI-TF and DPI-TF closely resembles the cation portion in Rhodorsil-FABA, where the isopropyl and methyl groups in Rhodorsil-FABA are replaced by tertiary butyl groups in BTBPI-TF and DPI-TF. These similarities allow us to study the effects of both cations and anions on the copper-induced temperature shift for the iodonium-based PAGs. The molecular weights of the iodonium-based PAGs are smaller than Rhodorsil-FABA. The mass loading of the iodonium-based PAGs in the PPC/PAG solutions were adjusted so as to maintain a constant PAG to PPC mole ratio, just as used in the Rhodorsil-FABA solutions. The TGA results for the iodonium-based PAGs are shown in Figure 5.5 to Figure 5.7. The TGA results are discussed separately for each iodonium-based PAG.

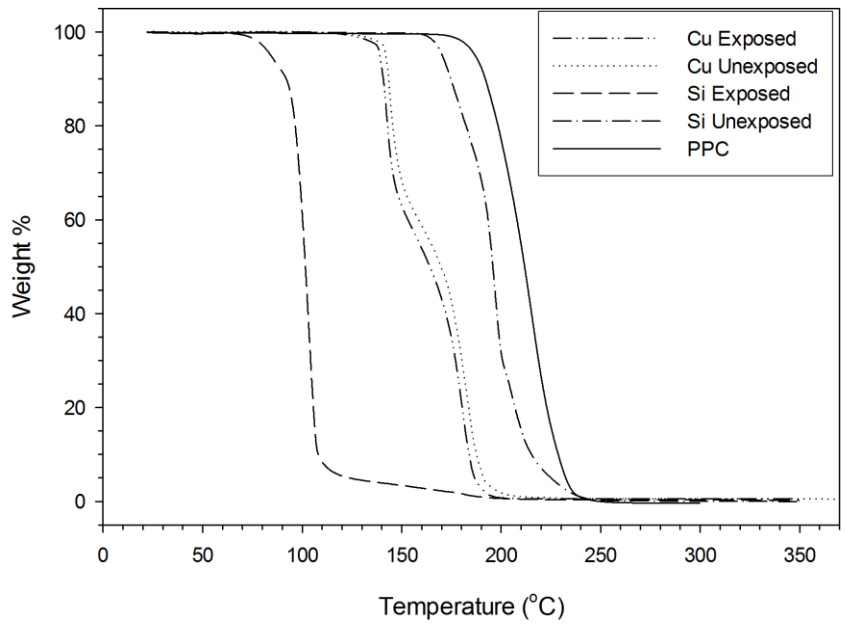


Figure 5.5 TGA results for PPC film containing iodonium-based PAG BTBPI-TF

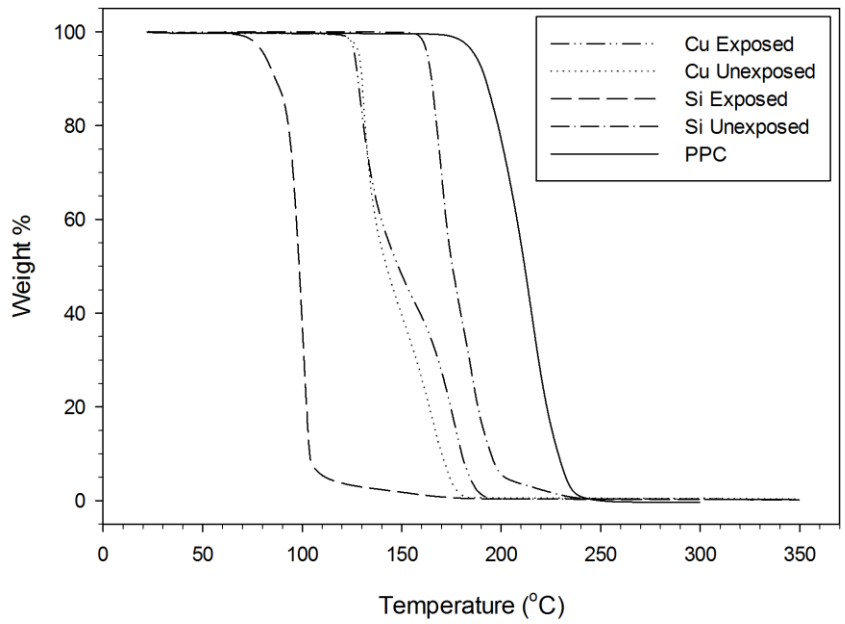


Figure 5.6 TGA results for PPC film containing iodonium-based PAG BTBPI-NF

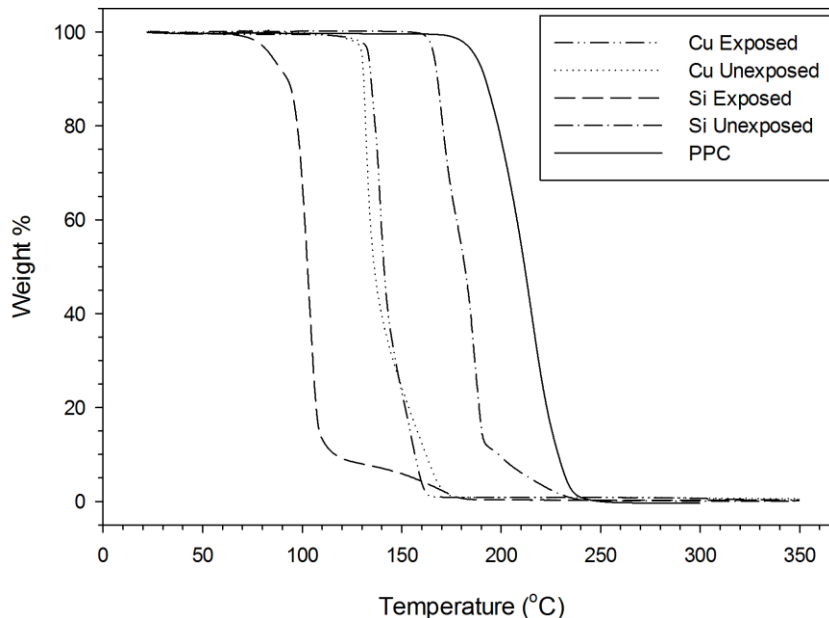


Figure 5.7 TGA results for PPC film containing iodonium-based PAG DPI-TF

Figure 5.5 shows the TGA results for the solution containing BTBPI-TF PAG. Si Exposed sample decomposed at 101°C due to UV activation of the PAG and subsequent acid creation. On the other hand, the Cu Exposed sample decomposed at 164°C, where there was a 63°C temperature shift relative to the Si Exposed case. This temperature shift due to the presence of copper was consistent with the hypothesis that if there is an interaction between the iodonium portion of the PAG and the dissolved Cu(I) in PPC, the Cu(I) ion appears to inhibit the PAG's ability to create an acid to catalyze PPC decomposition.

For the unexposed cases using BTBPI-TF, there was no thermal stability effect observed, contrary to the Rhodorsil-FABA case. That is, the decomposition temperature of Cu Unexposed sample was not higher than that of the Si Unexposed sample using BTBPI-TF. Contrarily, the Si Unexposed sample decomposed at a higher temperature

(196°C) compared to Cu Unexposed sample (169°C). In the Si Unexposed case, the thermal activation of the PAG and subsequent acid creation take place lowering the decomposition temperature compared to neat PPC. The situation is, however, more complex for the Cu Unexposed case. It appears that in the unexposed case, the Cu(I) ion interaction with the PAG destabilizes the PAG and facilitates acid creation, lowering the decomposition temperature relative to both the Si Unexposed case and neat PPC. In contrast to our result, Spencer et al. showed that the decomposition temperature of the Cu Unexposed samples was higher than the Si Unexposed samples. The decomposition temperature was even higher than neat PPC. This observation was left unexplained in the previous study [74]. A combination of the results here with the previous ones in [74] seems to lead to a two-step mechanism for the PPC thermal stability increase. First, Cu(I) inhibits acid creation in the PAG. Second, end-capping of PPC chains occurs by the copper species resulting in a higher thermal decomposition temperature than for neat PPC. This two-step mechanism is plausible because if the Cu(I) inhibits the acid creation, the decomposition temperature of the Cu Unexposed sample should not exceed the neat PPC decomposition temperature. It was previously reported that end-capping increases the thermal stability of PPC [77, 79, 86, 99]. Moreover, there is evidence in the literature for a thermal stability increase facilitated by metal ion coordination with the polymer backbone, as well as chain terminations [74, 78]. Thus, in our case, it is possible that the acid creation catalyzed in the unexposed case dominated over the end-capping of PPC, so that the net effect observed was the lowering of decomposition temperature for the Cu Unexposed samples. Another interesting result with BTBPI-TF PAG is that the decomposition temperatures of the PPC on copper (exposed or unexposed) were about

the same. The values were lower than the value observed for Si Unexposed. This result shows a significant interaction between the Cu(I) and the iodonium cation which results in acid creation independent of UV radiation.

Figure 5.6 shows the TGA results for the PPC/BTBPI-NF film. The PPC decomposition behavior resembles that of BTBPI-TF, shown in Figure 5.5. The Cu Exposed sample decomposed at a higher temperature (148°C) compared to Si Exposed sample (98°C), which is consistent with the previous results for the other iodonium-based PAGs. However, no thermal stability was observed for the unexposed cases. That is, the Cu Unexposed sample did not decompose at a higher temperature relative to the Si Unexposed sample due to acid creation, as discussed above. The PAG was thermally activated in the Si Unexposed case and in both cases on copper (exposed and unexposed), as shown by their lower decomposition temperature compared to neat PPC.

The TGA results for the films containing DPI-TF PAG are shown in Figure 5.7. The DPI-TF behavior is similar to BTBPI-TF and BTBPI-NF. The Cu Exposed sample decomposed at 141°C whereas the Si Exposed sample decomposed at 103°C showing the thermal stability increase for the exposed case. As already mentioned, there is no thermal stability increase for the unexposed cases. The decomposition temperatures for the Cu Exposed and Cu Unexposed films for DPI-TF are almost the same as the films containing BTBPI-TF and BTBPI-NF PAGs. This is due to the similarity between the DPI-TF and BTBPI cations.

It appears there are two steps in the TGA plots for PPC decomposition on copper, as shown in Figure 5.5, Figure 5.6, and Figure 5.7. Each shows an initial decrease in mass at about 150°C in the first step followed by further decomposition in the second step at a

higher temperature. This appears to be an indication of the complexity of the decomposition mechanism of PPC on copper with some acid being created by the copper-PAG interaction. The decomposition mechanism that occurred at lower temperatures may be different than at higher temperatures, e.g. by chain unzipping in the first region at lower temperatures, and by chain scission in the second region at a higher temperature [77-79, 81-83]. There is little or no residue, i.e. less than 0.5 wt%, left after full PPC decomposition which indicates that BTBPI-TF, BTBPI-NF and DPI-TF PAGs work well with PPC and can be used for air-cavity creation.

In light of the full body of results for the PPC films containing an iodonium-based PAGs, it is clear that there is a thermal stability increase for each sample when the film was coated on copper. No iodonium-based PAG was tested that did not show the result. Further, no sulfonium-based PAG showed any temperature effect of copper incorporation. This supports our hypothesis of a Cu(I)-I interaction. A possible explanation for thermal stability increase is that formation of a Cu(I)-I complex disrupts the decomposition of the PAG and its acid creation at the lowest decomposition temperatures (i.e. Cu Exposed). The formation of a Cu(I)-I complex in the unexposed cases seems to lead to two kinds of results. The first is the creation of an acid at a lower temperature than otherwise observed for the PPC/PAG mixture (Figure 5.5, Figure 5.6 and Figure 5.7) and the second is a stabilization of the PPC (Figure 1.5).

UV-vis spectroscopy was used to investigate the photo-bleaching of the PAGs and any other effects of UV irradiation. The same Rhodorsil-FABA concentration, 0.286 μ mole per ml of GBL solvent, was used in each of the six experiments, corresponding to: No PAG (PPC without PAG), Mixture (PPC and PAG), Cu Exposed, Cu Unexposed, Si

Exposed and Si Unexposed. The UV-vis results are shown in Figure 5.8 and tabulated in Table 5.2. The peak observed at 260 nm is due to the absorbance of the PAG and no other peaks were observed in the visible range. There were little changes in peak wavelength or absorbance as a result of UV irradiation or presence of copper. UV irradiation of the PAG and creation of the photoacid did not result in photo-bleaching of the PAG. The peak wavelength likely shifted slightly due to the PAG degradation products, such as toluene and isopropyl benzene, which are very close to each other (261 nm and 258 nm, respectively [161]).

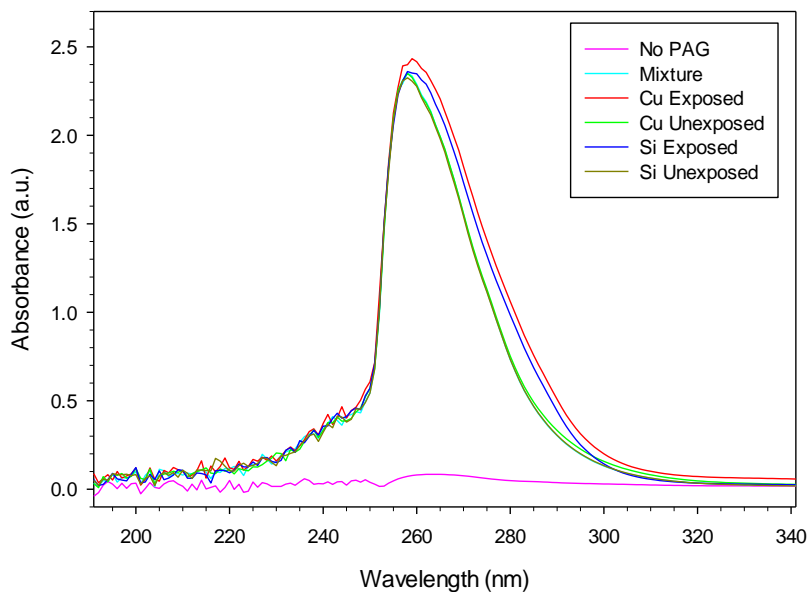


Figure 5.8 UV-vis spectroscopy results of PPC films on copper and on silicon with or without UV exposure

Table 5.2 UV-vis spectra peak wavelength (nm) and absorbance (AU) values

Sample	Wavelength (nm)	Absorbance (AU)
No PAG	264	0.08375
Mixture	258	2.35320
Cu Exposed	260	2.43400
Cu Unexposed	258	2.35400
Si Exposed	259	2.36130
Si Unexposed	258	2.32590

5.2 Discussion

Since the thermal stability increase of PPC was observed whenever the PPC/Rhodorsil-FABA solution was in contact with the copper surface, a specific interaction between the film and the copper is proposed. The effect was more clearly observed when a fresh copper surface was used where there was no native oxide layer on copper surface before coating the PPC film. This implies that dissolution of the native cupric oxide has no effect on the shift in PPC decomposition temperature. There is convincing evidence in the literature showing that metal ion incorporation can lead to an increase in thermal stability of polymers through the formation of complexes with polymer backbones or end-capping of the polymer [74, 78, 162]. Burrows et al. reported an increase in thermal stability of polyacrylamide by various metal ions such as Cu(II), Fe(II), Ni(II), Hg(I) caused by formation of a metal-polymer complex involving the amide group oxygen [162]. Yu et al. showed the inhibition of the end-initiated, unzipping decomposition of the PPC via Ca(II) coordination with carbonate groups of the PPC chains [78]. In contrast, the copper-initiated results shown here occur with a scarcity of copper ions where there are only 18 copper ions per 1720 monomers monomer units (average polymer chain length) [74]. Moreover, there is no guarantee that copper ions

will form complexes with chain ends and not with other sites in the polymer backbone. That is, it is possible for copper ions to interact with the PPC backbone rather than chain ends. Thus, the mechanism of temperature suppression observed here for the Cu(I)/PAG/PPC system is most likely due primarily to a Cu(I)/PAG interaction. The feasible scenario is an interaction between Cu(I) and I in the PAG where a Cu(I)-I complex disrupts the acid creating mechanism of the thermally or photolitically activated PAG. This mechanism is plausible from a stoichiometric point of view since the concentration of copper matches that of the PAG and not that of the PPC or its end groups, according to energy-dispersive x-ray spectroscopy (EDS) analysis in [74]. In addition, it is known that the cation is the portion of PAG responsible for the acid creation and UV absorbance [53]. Moreover, Crivello et al. studied the interaction of copper with diaryliodonium PAGs, such as 4-methyl-phenyl[4-(methylethyl)phenyl] iodoniumtetrakis (pentafluorophenyl)borate (FABA) and showed that Cu(I) is the only ion which interacts with PAGs among a group of ions including Ni(II), Co(II), Fe(II), Ag(I), Mn(III), Cr(III) and Pd(II) [163].

Thus, a mechanism for copper ion complexation with an iodonium-based PAG can be proposed. The Cu(I) ion is formed through oxidation of metallic copper and it forms an iodide complex with the iodide from the PAG, probably degrading the cation of the PAG without acid creation, or stabilizing it to prevent activation and subsequent acid creation. Since the acid is not produced at the same temperature, the thermal stability of PPC increases. Cupric ions have no effect on the PPC decomposition temperature [74].

The copper-PPC interaction proposed by Spencer et al. (i.e. end-capping stabilization) seems unlikely to be the primary effect since the stoichiometry does not

match. Further, all iodonium-based PAGs show the temperature shift and no sulfonium-based PAGs give the response even though they may have the same acid strength, as evidenced by the same conjugate base (i.e. common anion experiments). Moreover, it was previously shown that interactions between diaryliodonium salts and a small amount of Cu(I) are essential for the decomposition of diaryliodonium salts [163].

5.3 Summary and Conclusions

The PPC decomposition in the presence of the photolitically or thermally activated PAG was studied. Previously observed shifts in the decomposition temperature of PPC were investigated. The decomposition temperature of PPC can be altered when the PPC/PAG films contacts copper metal. XPS results show copper is in the Cu(I) oxidation state. The Cu(I) stoichiometry is similar to that of the PAG. Every iodonium-based PAG shows the PPC temperature shift and no sulfonium-based PAG shows the effect. Thus, it appears that the copper interacts with iodonium in the cation of the PAG and the acid creation mechanism of the PAG changes, often shifting the PPC decomposition to a higher temperature.

CHAPTER 6

CONCLUSIONS AND SUGGESTIONS FOR FUTURE WORK

The work presented in this dissertation focuses on improvements for electronic packaging technology. Specifically, three topics were investigated in this work: electroless copper deposition on PWBs, polymer-based air-gap MEMS packaging technology, and thermal stability enhancement in sacrificial polymers, such as poly(propylene carbonate) (PPC).

In the electroless copper deposition study, a new electroless copper deposition process was studied to achieve adherent electroless copper deposition using a Sn/Ag catalyst on non-roughened epoxy laminate substrates (PWBs). Compared to other the mineral acids used for surface pretreatment such as H_3PO_4 and HCl, hot H_2SO_4 treatment was identified as a simple and low-cost surface pretreatment method unique in catalyzing electroless copper deposition with Sn/Ag catalysts and in avoiding addition of surface roughness to PWB substrate. No deposition was possible without H_2SO_4 treatment. H_2SO_4 was found to remove impurities in PWB that prevent deposition, and to provide bond breaking in the vicinity of carbonyl (C=O) and acid/ester (O-C=O) functionalities. The sulfate content was found to adsorb on PWB after H_2SO_4 treatment, which facilitated Sn(II) sensitization by electrostatic interaction. The Sn/Ag catalysts were observed to provide successful electroless copper deposition on PWBs. XPS analysis revealed that the oxidation state of Ag and Sn in Sn/Ag catalysts were Ag(0) and Sn(IV) with a possible small content of Sn(II). This finding confirmed Sn(II) to Sn(IV) oxidation, and Ag(I) to Ag(0) reduction during catalyst formation. The structure of Sn/Ag catalyst was deduced

to be a core-shell nano-colloid with Ag(0)-only core and SnO₂ shell. It was plausible to consider some Sn(II) complexing with chloride ions to form SnCl₃⁻ on the outer surface of nano-colloids and preventing agglomeration. A practical deposition rate was obtained by Sn/Ag catalyst in agreement with the mixed the mixed potential theory. A satisfactory adhesion strength value was achieved in the electroless copper layer by the use of H₂SO₄ pretreatment and Sn/Ag catalyst. Although chemical adhesion was promoted by H₂SO₄ treatment, the mechanical adhesion was found to dominate the adhesion strength of electroless copper layer.

In the MEMS packaging study, a polymer-based air-gap MEMS packaging approach was investigated to reduce the cost, to simplify the packaging process and to analyze the polymeric residue. The idea was to achieve wide (~2.5x3.2 mm) and tall (10-20 μm) air-gaps to provide size-compatible packaging to MEMS devices, such as accelerometers and gyroscopes. Two different PPC sacrificial polymers, Novomer 160K and QPAC 40 141K, were compared using TGA and NMR analysis. Novomer 160K was found to have a smaller catalyst residue and residual solvent, less polyether content and greater head-to-tail (HT) ratio. A precipitation-based PPC purification method was observed to decrease the decomposition temperature of Novomer 160K by removing impurities and residual solvent coming from PPC synthesis. BCB was identified as a PPC-compatible overcoat material providing excellent mechanical stability to air-gap structures. A kinetic comparison was done between PPC decomposition and BCB curing processes to determine the optimal thermal treatment recipe. It was found that the optimal treatment is a two-step heating process that includes a BCB curing at a lower temperature in the first step, and PPC decomposition at a higher temperature. It is because PPC goes

from solid to gaseous phase during heating, and creates a pressure inside the air-gap. The BCB should have a sufficient cross-linking to withstand the generated pressures. Two air-gap formation processes, RIE process (uses non-photosensitive PPC) and direct photopatterning process (uses photosensitive PPC), were proposed depending on how the PPC was patterned. Less residue and more reliable air-gap structures were obtained using the RIE process. The direct photopatterning process was simpler, however a greater amount of residue was observed due to photoacid generator (PAG), at least 1.5-2x of the residue in the RIE process. XPS comparison of the residues indicated that photosensitive PPC residue included a large elemental amorphous carbon content (C-C) and C-F functionality, whereas non-photosensitive PPC residue included more oxidized carbon functionalities (e.g. ether, carbonyl, carbonate). The thermal conditions in direct photopatterning process were observed to be limited by the thermal activation of PAG at lower temperatures (~180°C) before BCB becoming rigid enough. Comparison of two-layer PPC structures with both photosensitive and non-photosensitive PPC layers revealed that it was possible to obtain reliable air-gap structures only if the photosensitive PPC was the bottom layer. Nanoindentation measurements indicated that the mechanical strength of BCB caps were due to prestressing in BCB because of its tensile stress on silicon substrates.

In the study of thermal stability of PPC, the thermal stability enhancement of PPC by Cu(I) ions was investigated to determine its mechanism. An increased thermal stability of PAG-containing PPC film was previously reported by our group (PAG was Rhodorsil-FABA, an iodonium-based PAG). XPS analysis done on the surface of PPC/PAG films prepared on Cu-sputtered substrates showed the presence of copper in

Cu(I) oxidation state in the film, with an amount similar to the amount of PAG (Rhodorsil-FABA). Cu(I) ion can be formed through oxidation of copper surface by dissolved oxygen in the PPC solution. Based on these observations, a thermal stability mechanism was proposed as follows. A complexation-type of interaction between the iodonium in the cation of the PAG and Cu(I) inhibits acid creation mechanism of PAG. In the absence of acid, the PPC decomposition is not catalyzed, so the thermal stability of PPC increases on Cu surfaces. This hypothesis was tested by comparing the thermal stability of PPC/PAG films prepared by using a number of iodonium and sulfonium-based PAGs. Every PAG/PPC film including iodonium-based PAGs showed thermal stability increase in the UV exposed cases. No thermal stability increase was observed using any sulfonium-based PAG, as expected. The findings were observed to support the proposed mechanism in-part. However, the actual mechanism was more complex since PPC films with the iodonium-based PAGs did not show thermal stability increase in the UV unexposed cases.

The future work of the above projects can proceed in the following directions. For electroless copper study, the Sn/Ag core-shell nano-colloid structure can be investigated using X-ray diffraction (XRD) in order to confirm the presence of SnO₂ and SnCl₃⁻ complex in the shell. This is because it is difficult to distinguish between Sn(II) and Sn(IV) using X-ray photoelectron spectroscopy (XPS) since the associated binding energies are close. To widen the applicability of the electroless copper deposition process, deposition on nano-sized trenches can be investigated to determine its applicability for transistor fabrication. For the polymer-based air-gap study, the electrical properties of the residue, i.e. dielectric constant and loss tangent, can be measured using

comb electrodes or split post dielectric resonators [164]. This is important for the reliable and low-loss operation of MEMS devices packaged using polymer-based air-gaps. In order to quantify the exact kinetics of air-gap formation processes, pressure sensors can be fabricated and used for *in situ* pressure monitoring while PPC is decomposing inside an air-gap structure. The adhesion between undecomposed PPC and BCB can be investigated experimentally, and computationally assuming a Lennard-Jones type of interaction [165]. Combined with the *in situ* kinetic data that could be obtained using pressure sensors mentioned above, this could allow complete modeling and simulation of reliable air-gap formation processes. The modeling and simulation can enable fast and low-cost exploration and optimization of new materials and processing conditions. The polymer-based air-gap packaging can be performed on actual MEMS devices, along with wire-bonding to a lead-frame and epoxy-overmolding, to demonstrate the industrial viability of the method. For the thermal stability of PPC study, solvent-based thermal stability control mechanisms can be investigated, such as reversible end-capping with solvents. New PPC polymers with higher glass transition temperature, lower decomposition temperature and lesser impurities can be synthesized and characterized. The improvements in the sacrificial polymers can be directly tested in polymer-based air-gap formation processes.

REFERENCES

- [1] E. J. O'Sullivan, "Fundamental and Practical Aspects of the Electroless Deposition Reaction," *Advances in Electrochemical Science and Engineering, Volume 7*, pp. 225-273: Wiley-VCH Verlag GmbH, 2001.
- [2] C. P. L. Li, P. Ciccolo, and D. K. W. Yee, "Inner-layer copper reliability of electroless copper processes," *Circuit World*, vol. 36, no. 1, pp. 31-37, 2010.
- [3] M. Paunovic, "Electroless Deposition of Copper," *Modern Electroplating*, pp. 433-446: John Wiley & Sons, Inc., 2010.
- [4] N. Fritz, H. Koo, Z. Wilson *et al.*, "Electroless Deposition of Copper on Organic and Inorganic Substrates Using a Sn/Ag Catalyst," *Journal of the Electrochemical Society*, vol. 159, no. 6, pp. D386-D392, November, 2012.
- [5] E. J. Denlinger, "LOSSES OF MICROSTRIP LINES," *IEEE Transactions on Microwave Theory and Techniques*, vol. 28, no. 6, pp. 513-522, 1980.
- [6] N. A. Z. Zakaria, and C. Free, "An investigation of losses in microstrip lines," in RF and Microwave Conference, RFM 2004 Proceedings, Selangor, MALAYSIA, 2004, pp. 93-98.
- [7] S. Siau, A. Vervaet, E. Schacht *et al.*, "Influence of chemical pretreatment of epoxy polymers on the adhesion strength of electrochemically deposited Cu for use in electronic interconnections," *Journal of the Electrochemical Society*, vol. 151, no. 2, pp. C133-C141, February, 2004.
- [8] S. Siau, A. Vervaet, L. Van Vaeck *et al.*, "Adhesion strength of the epoxy polymer/copper interface for use in microelectronics," *Journal of the Electrochemical Society*, vol. 152, no. 6, pp. C442-C455, May, 2005.
- [9] R. L. Cohen, and K. W. West, "GENERATIVE AND STABILIZING PROCESSES IN TIN-PALLADIUM SOLS AND PALLADIUM SOL SENSITIZERS," *Journal of the Electrochemical Society*, vol. 120, no. 4, pp. 502-508, April, 1973.
- [10] O. Holderer, T. Epicier, C. Esnouf *et al.*, "Direct structural and chemical analysis of individual core-shell (Pd, Sn) nanocolloids," *Journal of Physical Chemistry B*, vol. 107, no. 8, pp. 1723-1726, February, 2003.
- [11] C. L. Yaws, *Yaws Handbook of Properties of the Chemical Elements*, Norwich, N.Y.: Knovel [electronic source], 2011.

- [12] I. OHNO, O. WAKABAYASHI, and S. HARUYAMA, "ANODIC-OXIDATION OF REDUCTANTS IN ELECTROLESS PLATING," *Journal of the Electrochemical Society*, vol. 132, no. 10, pp. 2323-2330, May, 1985.
- [13] M. Paunovic, and M. Schlesinger, *Fundamentals of Electrochemical Deposition*, New York: Wiley, 1998.
- [14] C. R. SHIPLEY, "METHOD OF ELECTROLESS DEPOSITION ON A SUBSTRATE AND CATALYST SOLUTION THEREFOR," *U.S. Patent*, no. 3,011,920, 1961.
- [15] A. Vaskelis, A. Jagminiene, L. Tamasauskaite-Tamasiunaite *et al.*, "Silver nanostructured catalyst for modification of dielectrics surface," *Electrochimica Acta*, vol. 50, no. 23, pp. 4586-4591, August, 2005.
- [16] Y. Fujiwara, Y. Kobayashi, K. Kita *et al.*, "Ag nanoparticle catalyst for electroless Cu deposition and promotion of its adsorption onto epoxy substrate," *Journal of the Electrochemical Society*, vol. 155, no. 5, pp. D377-D382, March, 2008.
- [17] Y. Fujiwara, Y. Kobayashi, T. Sugaya *et al.*, "Adsorption Promotion of Ag Nanoparticle Using Cationic Surfactants and Polyelectrolytes for Electroless Cu Plating Catalysts," *Journal of the Electrochemical Society*, vol. 157, no. 4, pp. D211-D216, February, 2010.
- [18] S. Siau, A. Vervaet, A. Van Calster *et al.*, "Epoxy polymer surface roughness modeling based on kinetic studies of wet chemical treatments," *Journal of the Electrochemical Society*, vol. 151, no. 8, pp. J54-J61, July, 2004.
- [19] A. Pizzi, and K. L. Mittal, *Handbook of Adhesive Technology*, 2nd ed., New York, U.S.A.: Marcel Dekker, Inc., 2003.
- [20] S. Ebnesajjad, *Surface Treatment of Materials for Adhesion Bonding*, Norwich, NY, U.S.A.: p. 77, William Andrew Pub., 2006.
- [21] S. Siau, A. Vervaet, E. Schacht *et al.*, "Epoxy polymer surface modification through wet-chemical organic surface synthesis for adhesion improvement in microelectronics," *Thin Solid Films*, vol. 495, no. 1-2, pp. 348-356, January, 2006.
- [22] S. Siau, A. Vervaet, E. Schacht *et al.*, "Chemical modification of buildup epoxy surfaces for altering the adhesion of electrochemically deposited copper," *Journal of the Electrochemical Society*, vol. 152, no. 9, pp. D136-D150, August, 2005.
- [23] J. Ge, R. Tuominen, and J. K. Kivilahti, "Adhesion of electrolessly-deposited copper to photosensitive epoxy," *Journal of Adhesion Science and Technology*, vol. 15, no. 10, pp. 1133-1143, April, 2001.

- [24] J. Ge, M. P. K. Turunen, and J. K. Kivilahti, "Surface modification and characterization of photodefinable epoxy/copper systems," *Thin Solid Films*, vol. 440, no. 1-2, pp. 198-207, September, 2003.
- [25] D. Schroer, R. J. Nichols, and H. Meyer, "PRETREATMENT OF POLYMER SURFACES - THE CRUCIAL STEP PRIOR TO METAL-DEPOSITION," *Electrochimica Acta*, vol. 40, no. 10, pp. 1487-1494, July, 1995.
- [26] S. Siau, A. Vervaet, S. Nalines *et al.*, "Kinetic study of wet chemical treatments on the surface roughness of epoxy polymer layers for buildup layers - I. Sweller influence," *Journal of the Electrochemical Society*, vol. 151, no. 12, pp. C816-C830, November, 2004.
- [27] T. Laine-Ma, P. Ruuskanen, S. Kortet *et al.*, "Electroless copper plating and surface characterization of thermoplastic PPO based printed circuit boards," *Circuit World*, vol. 35, no. 4, pp. 22-30, 2009.
- [28] J. Ge, M. P. K. Turunen, M. Kusevic *et al.*, "Effects of surface treatment on the adhesion of copper to a hybrid polymer material," *Journal of Materials Research*, vol. 18, no. 11, pp. 2697-2707, November, 2003.
- [29] S. Siau, A. Vervaet, S. Nalines *et al.*, "Kinetic study of wet chemical treatments on the surface roughness of epoxy polymer layers for buildup layers - II. Oxidative treatment of the surface," *Journal of the Electrochemical Society*, vol. 151, no. 12, pp. C831-C849, November, 2004.
- [30] S. Asakura, S. Fukutani, and A. Fuwa, "Fabrication of built-in copper microstructures on epoxy resin," *Microelectronic Engineering*, vol. 75, no. 4, pp. 375-382, November, 2004.
- [31] D. Schaubroeck, J. De Baets, T. Desmet *et al.*, "Surface modification of an epoxy resin with polyamines via cyanuric chloride coupling," *Applied Surface Science*, vol. 256, no. 21, pp. 6269-6278, August, 2010.
- [32] D. Schaubroeck, E. Van Den Eeckhout, J. De Baets *et al.*, "Surface Modification of a Photo-Definable Epoxy Resin with Polydopamine to Improve Adhesion with Electroless Deposited Copper," *Journal of Adhesion Science and Technology*, vol. 26, no. 18-19, pp. 2301-2314, October, 2012.
- [33] B. Mkhlef, A. Cobley, L. Paniwnyk *et al.*, "Initial studies to optimise the sonochemical surface modification of a high Tg laminate," *Circuit World*, vol. 38, no. 3, pp. 124-129, 2012.
- [34] A. Cobley, and T. Mason, "The sonochemical surface modification of materials for electronic manufacturing. The effect of ultrasonic source to sample distance," *Circuit World*, vol. 34, no. 3, pp. 18-22, 2008.

- [35] G. G. Kim, J. A. Kang, J. H. Kim *et al.*, "Metallization of polymer through a novel surface modification applying a photocatalytic reaction," *Surface & Coatings Technology*, vol. 201, no. 6, pp. 3761-3766, December, 2006.
- [36] J. Ge, M. P. K. Turunen, and J. K. Kivilahti, "Surface modification of a liquid-crystalline polymer for copper metallization," *Journal of Polymer Science Part B-Polymer Physics*, vol. 41, no. 6, pp. 623-636, March, 2003.
- [37] H. Hayden, E. Elce, S. A. B. Allen *et al.*, "Adhesion Enhancement Between Electroless Copper and Epoxy-based Dielectrics," *IEEE Transactions on Advanced Packaging*, vol. 32, no. 4, pp. 758-767, November, 2009.
- [38] E. Sheng, I. Sutherland, D. M. Brewis *et al.*, "EFFECTS OF THE CHROMIC-ACID ETCHING ON PROPYLENE POLYMER SURFACES," *Journal of Adhesion Science and Technology*, vol. 9, no. 1, pp. 47-60, January, 1995.
- [39] F. P. M. Mercx, A. Benzina, A. D. Vanlangeveld *et al.*, "IMPROVED ADHESIVE PROPERTIES OF HIGH-MODULUS POLYETHYLENE STRUCTURES .1. OXIDATIVE ACID ETCHING," *Journal of Materials Science*, vol. 28, no. 3, pp. 753-759, February, 1993.
- [40] "Material Safety Data Sheet (MSDS) of Potassium Dichromate," <http://hazard.com/msds/mf/baker/baker/files/p5719.htm>.
- [41] "MEMS Packaging Market and Technology Trends Report," 2012, Yole Développement.
- [42] J. H. Lau, "Design and Process of 3D MEMS System-in-Package (SiP)," *Journal of Microelectronic & Electronic Packaging*, vol. 7, no. 1, pp. 10-15, May, 2010.
- [43] M. Gaitan, "MEMS Technology Roadmapping," in Nano-Tec Workshop 3, 2012.
- [44] "Compound Annual Growth Rate - CAGR," <http://www.investopedia.com/terms/c/cagr.asp>.
- [45] P. S. Liu, J. L. Wang, L. Y. Tong *et al.*, "Advances in the Fabrication Processes and Applications of Wafer Level Packaging," *Journal of Electronic Packaging*, vol. 136, no. 2, June, 2014.
- [46] M. Esashi, "Wafer level packaging of MEMS," *Journal of Micromechanics and Microengineering*, vol. 18, no. 7, July, 2008.
- [47] J. Kim, Y.-T. Cheng, M. Chiao *et al.*, "Packaging and Reliability Issues in Micro/Nano Systems," *Springer Handbook of Nanotechnology*, 2007, p. 1777.
- [48] P. Monajemi, P. J. Joseph, P. A. Kohl *et al.*, "Wafer-level MEMS packaging via thermally released metal-organic membranes," *Journal of Micromechanics and Microengineering*, vol. 16, no. 4, pp. 742-750, April, 2006.

- [49] R. Saha, N. Fritz, S. A. Bidstrup-Allen *et al.*, “Packaging-compatible wafer level capping of MEMS devices,” *Microelectronic Engineering*, vol. 104, pp. 75-84, April, 2013.
- [50] P. J. Joseph, P. Monajemi, F. Ayazi *et al.*, “Wafer-level packaging of micromechanical resonators,” *IEEE Transactions on Advanced Packaging*, vol. 30, no. 1, pp. 19-26, February, 2007.
- [51] J. P. Jayachandran, H. A. Reed, H. S. Zhen *et al.*, “Air-channel fabrication for microelectromechanical systems via sacrificial photosensitive polycarbonates,” *Journal of Microelectromechanical Systems*, vol. 12, no. 2, pp. 147-159, April, 2003.
- [52] H. A. Kelleher, “AIR-GAPS VIA THERMALLY DECOMPOSABLE POLYMERS AND THEIR APPLICATION TO COMPLIANT WAFER LEVEL PACKAGING (CWLP),” School of Chemical and Biomolecular Engineering, Georgia Institute of Technology, 2004.
- [53] M. Gupta, P. Joseph, and P. Kohl, “Photoacid generators for catalytic decomposition of polycarbonate,” *Journal of Applied Polymer Science*, vol. 105, no. 5, pp. 2655-2662, September, 2007.
- [54] M. G. Gupta, “PHOTOACID GENERATORS FOR CATALYTIC DECOMPOSITION OF POLYCARBONATE,” School of Chemical and Biomolecular Engineering, Georgia Institute of Technology, 2006.
- [55] L. J. Gao, M. Xiao, S. J. Wang *et al.*, “Copolymerization of carbon dioxide and propylene oxide with zinc glutarate as catalyst in the presence of compounds containing active hydrogen,” *Journal of Applied Polymer Science*, vol. 104, no. 1, pp. 15-20, April, 2007.
- [56] Y.-C. Chen, and P. A. Kohl, “Photosensitive sacrificial polymer with low residue,” *Microelectronic Engineering*, vol. 88, no. 10, pp. 3087-3093, October, 2011.
- [57] B. A. Peeni, M. L. Lee, A. R. Hawkins *et al.*, “Sacrificial layer microfluidic device fabrication methods,” *Electrophoresis*, vol. 27, no. 24, pp. 4888-4895, December, 2006.
- [58] D. Bhusari, H. A. Reed, M. Wedlake *et al.*, “Fabrication of air-channel structures for microfluidic, microelectromechanical, and microelectronic applications,” *Journal of Microelectromechanical Systems*, vol. 10, no. 3, pp. 400-408, September, 2001.
- [59] P. Kohl, Q. Zhao, K. Patel *et al.*, “Air-gaps for electrical interconnections,” *Electrochemical and Solid State Letters*, vol. 1, no. 1, pp. 49-51, July, 1998.

- [60] T. J. Spencer, T. Osborn, and P. A. Kohl, "Materials science - High-frequency chip connections," *Science*, vol. 320, no. 5877, pp. 756-757, May, 2008.
- [61] T. J. Spencer, P. J. Joseph, T. H. Kim *et al.*, "Air-gap transmission lines on organic substrates for low-loss interconnects," *IEEE Transactions on Microwave Theory and Techniques*, vol. 55, no. 9, pp. 1919-1925, September, 2007.
- [62] T. J. Spencer, J. K. Chen, R. Saha *et al.*, "Air Cavity Low-Loss Signal Lines on BT Substrates for High Frequency Chip-to-Chip Communication," in IEEE 59th Electronic Components and Technology Conference (ECTC), San Diego, CA, USA, 2009, pp. 1221-1226.
- [63] S. Park, S. A. B. Allen, and P. A. Kohl, "Air-gaps for high-performance on-chip interconnect part II: Modeling, fabrication, and characterization," *Journal of Electronic Materials*, vol. 37, no. 10, pp. 1534-1546, October, 2008.
- [64] Y. C. Lee, and C. S. Park, "A novel CPW-to-stripline vertical via transition using a stagger via structure and embedded air cavities for V-band LTCC SiP applications," in IEEE Asia-Pacific Microwave Conference, Suzhou, CHINA, 2005, pp. 1307-1310.
- [65] J. M. Yook, K. M. Kim, and Y. S. Kwon, "Air-Cavity Transmission Lines on Anodized Aluminum for High-Performance RF Modules," *IEEE Microwave and Wireless Components Letters*, vol. 19, no. 10, pp. 623-625, October, 2009.
- [66] S. S. Song, and K. S. Seo, "A W-Band Air-Cavity Filter Integrated on a Thin-Film Substrate," *IEEE Microwave and Wireless Components Letters*, vol. 19, no. 4, pp. 200-202, April, 2009.
- [67] S. Song, C. S. Yoo, and K. S. Seo, "W-Band Bandpass Filter Using Micromachined Air-Cavity Resonator With Current Probes," *IEEE Microwave and Wireless Components Letters*, vol. 20, no. 4, pp. 205-207, April, 2010.
- [68] N. R. Devlin, D. K. Brown, and P. A. Kohl, "Patterning decomposable polynorbornene with electron beam lithography to create nanochannels," *Journal of Vacuum Science & Technology B*, vol. 27, no. 6, pp. 2508-2511, November, 2009.
- [69] X. Q. Wu, H. A. Reed, Y. Wang *et al.*, "Fabrication of microchannels using polynorbornene photosensitive sacrificial materials," *Journal of the Electrochemical Society*, vol. 150, no. 9, pp. H205-H213, September, 2003.
- [70] W. L. Li, J. O. Tegenfeldt, L. Chen *et al.*, "Sacrificial polymers for nanofluidic channels in biological applications," *Nanotechnology*, vol. 14, no. 6, pp. 578-583, June, 2003.

- [71] P. J. Joseph, H. A. Kelleher, S. A. B. Allen *et al.*, "Improved fabrication of micro air-channels by incorporation of a structural barrier," *Journal of Micromechanics and Microengineering*, vol. 15, no. 1, pp. 35-42, January, 2005.
- [72] H. A. Reed, C. E. White, V. Rao *et al.*, "Fabrication of microchannels using polycarbonates as sacrificial materials," *Journal of Micromechanics and Microengineering*, vol. 11, no. 6, pp. 733-737, November, 2001.
- [73] C. E. White, and C. L. Henderson, "Photosensitive copolycarbonates for use as sacrificial materials in the fabrication of microfluidic and microelectromechanical devices," in Conference on Advances in Resist Technology and Processing XXI, Santa Clara, CA, USA, 2004, pp. 850-860.
- [74] T. Spencer, Y. Chen, R. Saha *et al.*, "Stabilization of the Thermal Decomposition of Poly(Propylene Carbonate) Through Copper Ion Incorporation and Use in Self-Patterning," *Journal of Electronic Materials*, vol. 40, no. 6, pp. 1350-1363, June, 2011.
- [75] V. Rajarathinam, N. Fritz, S. A. B. Allen *et al.*, "Imprint lithography enabling ultra-low loss coaxial interconnects," *Microelectronic Engineering*, vol. 88, no. 3, pp. 240-246, March, 2011.
- [76] S. Inoue, H. Koinuma, and T. Tsuruta, "COPOLYMERIZATION OF CARBON DIOXIDE AND EPOXIDE," *Journal of Polymer Science Part B-Polymer Letters*, vol. 7, no. 4, pp. 287-292, April, 1969.
- [77] D. D. Dixon, M. E. Ford, and G. J. Mantell, "THERMAL STABILIZATION OF POLY(ALKYLENE CARBONATE)S," *Journal of Polymer Science Part C-Polymer Letters*, vol. 18, no. 2, pp. 131-134, February, 1980.
- [78] T. Yu, Y. Zhou, K. Liu *et al.*, "Improving thermal stability of biodegradable aliphatic polycarbonate by metal ion coordination," *Polymer Degradation and Stability*, vol. 94, no. 2, pp. 253-258, February, 2009.
- [79] S. W. Peng, Y. X. An, C. Chen *et al.*, "Thermal degradation kinetics of uncapped and end-capped poly(propylene carbonate)," *Polymer Degradation and Stability*, vol. 80, no. 1, pp. 141-147, April, 2003.
- [80] X. Li, Y. Meng, Q. Zhu *et al.*, "Thermal decomposition characteristics of poly(propylene carbonate) using TG/IR and Py-GC/MS techniques," *Polymer Degradation and Stability*, vol. 81, no. 1, pp. 157-165, July, 2003.
- [81] B. Y. Liu, X. J. Zhao, X. H. Wang *et al.*, "Thermal degradation kinetics of poly(propylene carbonate) obtained from the copolymerization of carbon dioxide and propylene oxide," *Journal of Applied Polymer Science*, vol. 90, no. 4, pp. 947-953, October, 2003.

- [82] G. Luinstra, "Poly(propylene carbonate), old copolymers of propylene oxide and carbon dioxide with new interests: Catalysis and material properties," *Polymer Reviews*, vol. 48, no. 1, pp. 192-219, February, 2008.
- [83] T. Spencer, and P. Kohl, "Decomposition of poly(propylene carbonate) with UV sensitive iodonium salts," *Polymer Degradation and Stability*, vol. 96, no. 4, pp. 686-702, April, 2011.
- [84] H. Yan, W. Cannon, and D. Shanefield, "Thermal decomposition behaviour of poly(propylene carbonate)," *Ceramics International*, vol. 24, no. 6, pp. 433-439, December, 1998.
- [85] G. Luinstra, G. Haas, F. Molnar *et al.*, "On the formation of aliphatic polycarbonates from epoxides with chromium(III) and aluminum(III) metal-salen complexes," *Chemistry-a European Journal*, vol. 11, no. 21, pp. 6298-6314, October, 2005.
- [86] M. J. Yao, F. Mai, H. Deng *et al.*, "Improved Thermal Stability and Mechanical Properties of Poly(propylene carbonate) by Reactive Blending with Maleic Anhydride," *Journal of Applied Polymer Science*, vol. 120, no. 6, pp. 3565-3573, June, 2011.
- [87] J. Jiao, M. Xiao, D. Shu *et al.*, "Preparation and characterization of biodegradable foams from calcium carbonate reinforced poly(propylene carbonate) composites," *Journal of Applied Polymer Science*, vol. 102, no. 6, pp. 5240-5247, December, 2006.
- [88] X. F. Ma, P. R. Chang, J. G. Yu *et al.*, "Preparation and properties of biodegradable poly(propylene carbonate)/thermoplastic dried starch composites," *Carbohydrate Polymers*, vol. 71, no. 2, pp. 229-234, January, 2008.
- [89] S. S. Joshi, and A. M. Mebel, "Computational modeling of biodegradable blends of starch amylose and poly-propylene carbonate," *Polymer*, vol. 48, no. 13, pp. 3893-3901, June, 2007.
- [90] Z. H. Zhang, Z. S. Mo, H. F. Zhang *et al.*, "Miscibility and hydrogen-bonding interactions in blends of carbon dioxide/epoxy propane copolymer with poly (p-vinylphenol)," *Journal of Polymer Science Part B-Polymer Physics*, vol. 40, no. 17, pp. 1957-1964, September, 2002.
- [91] X. D. Shi, and Z. H. Gan, "Preparation and characterization of poly(propylene carbonate)/montmorillonite nanocomposites by solution intercalation," *European Polymer Journal*, vol. 43, no. 12, pp. 4852-4858, December, 2007.
- [92] N. Wang, X. X. Zhang, J. G. Yu *et al.*, "Partially miscible poly(lactic acid)-blend-poly(propylene carbonate) filled with carbon black as conductive polymer composite," *Polymer International*, vol. 57, no. 9, pp. 1027-1035, September, 2008.

- [93] D. Z. Yang, and P. Hu, "Miscibility, crystallization, and mechanical properties of poly(3-hydroxybutyrate) and poly(propylene carbonate) biodegradable blends," *Journal of Applied Polymer Science*, vol. 109, no. 3, pp. 1635-1642, August, 2008.
- [94] Z. Zhang, Q. Shi, J. Peng *et al.*, "Partial delamination of the organo-montmorillonite with surfactant containing hydroxyl groups in maleated poly(propylene carbonate)," *Polymer*, vol. 47, no. 26, pp. 8548-8555, December, 2006.
- [95] Z. Zhang, J. H. Lee, S. H. Lee *et al.*, "Morphology, thermal stability and rheology of poly(propylene carbonate)/organoclay nanocomposites with different pillaring agents," *Polymer*, vol. 49, no. 12, pp. 2947-2956, June, 2008.
- [96] S. D. Thorat, P. J. Phillips, V. Semenov *et al.*, "Physical properties of aliphatic polycarbonates made from CO₂ and epoxides," *Journal of Applied Polymer Science*, vol. 89, no. 5, pp. 1163-1176, August, 2003.
- [97] L. J. Gao, M. Xiao, S. J. Wang *et al.*, "Copolymerization of carbon dioxide and propylene oxide with zinc glutarate in the presence of compounds containing active hydrogen," *Journal of Applied Polymer Science*, vol. 104, no. 1, pp. 15-20, April, 2007.
- [98] L. J. Gao, M. Xiao, S. J. Wang *et al.*, "Thermally stable poly(propylene carbonate) synthesized by copolymerizing with bulky naphthalene containing monomer," *Journal of Applied Polymer Science*, vol. 108, no. 2, pp. 1037-1043, April, 2008.
- [99] P. F. Song, M. Xiao, F. G. Du *et al.*, "Synthesis and properties of aliphatic polycarbonates derived from carbon dioxide, propylene oxide and maleic anhydride," *Journal of Applied Polymer Science*, vol. 109, no. 6, pp. 4121-4129, September, 2008.
- [100] L. B. Lu, and K. L. Huang, "Synthesis and characteristics of a novel aliphatic polycarbonate, poly(propylene oxide)-co-(carbon dioxide)-co-(gamma-butyrolactone)," *Polymer International*, vol. 54, no. 6, pp. 870-874, June, 2005.
- [101] Q. Y. Liu, Y. N. Zou, Y. L. Bei *et al.*, "Mechanic properties and thermal degradation kinetics of terpolymer poly(propylene cyclohexene carbonate)s," *Materials Letters*, vol. 62, no. 17-18, pp. 3294-3296, June, 2008.
- [102] L. B. Lu, S. Q. Liu, and K. L. Huang, "Molecular simulation of structure and loading-drug character of poly(propylene-co-gamma-butyrolactone carbonate)," *Journal of Applied Polymer Science*, vol. 107, no. 2, pp. 872-880, January, 2008.
- [103] Y. S. Qin, Q. W. Ma, X. H. Wang *et al.*, "Electron-beam irradiation on poly(propylene carbonate) in the presence of polyfunctional monomers," *Polymer Degradation and Stability*, vol. 92, no. 10, pp. 1942-1947, October, 2007.

- [104] Y. H. Tao, X. H. Wang, X. J. Zhao *et al.*, "Crosslinkable poly(propylene carbonate): High-yield synthesis and performance improvement," *Journal of Polymer Science Part a-Polymer Chemistry*, vol. 44, no. 18, pp. 5329-5336, September, 2006.
- [105] T. Yu, Y. Zhou, Y. Zhao *et al.*, "Hydrogen-bonded thermostable liquid crystalline complex formed by biodegradable polymer and amphiphilic molecules," *Macromolecules*, vol. 41, no. 9, pp. 3175-3180, May, 2008.
- [106] "ISOLA 185HR Laminate Product Page," <http://www.isola-group.com/products/185hr/>.
- [107] M. W. Jawitz, *Printed Circuit Board Materials Handbook*, New York: McGraw-Hill, 1997.
- [108] Y. Kobayashi, V. Salgueirino-Maceira, and L. M. Liz-Marzan, "Deposition of silver nanoparticles on silica spheres by pretreatment steps in electroless plating," *Chemistry of Materials*, vol. 13, no. 5, pp. 1630-1633, May, 2001.
- [109] M. Schlesinger, and M. Paunovic, *Modern electroplating*, 4th edition ed., New York: John Wiley, 2000.
- [110] "Avantage Data System," <http://www.thermoscientific.com/surfaceanalysis>.
- [111] "CasaXPS: Processing Software for XPS, AES, SIMS and More," <http://www.casaxps.com/>.
- [112] J. C. Vickerman, *Surface Analysis : The Principal Techniques*, Chichester, UK: 2nd ed., John Wiley, 1997.
- [113] T. J. Spencer, and P. A. Kohl, "Decomposition of poly(propylene carbonate) with UV sensitive iodonium salts," *Polymer Degradation and Stability*, vol. 96, no. 4, pp. 686-702, April, 2011.
- [114] S. Ying-Hung, P. Garrou, I. Jang-Hi *et al.*, "Benzocyclobutene-based polymers for microelectronics," *Chemical Innovation*, vol. 31, no. 12, pp. 41, December, 2001.
- [115] Y. H. So, P. Foster, J. H. Im *et al.*, "Divinylsiloxane-bisbenzocyclobutene-based polymer modified with polystyrene-polybutadiene-polystyrene triblock copolymers," *Journal of Polymer Science Part a-Polymer Chemistry*, vol. 44, no. 5, pp. 1591-1599, March, 2006.
- [116] "Cure and Oxidation Measurements for CYCLOTENE 3000 & 4000 Series Resins," <http://www.dow.com/cyclotene/resource/prodlit.htm>.
- [117] "CYCLOTENE Advanced Electronics Resins - CYCLOTENE 4000 Resin Oven Curing," <http://www.dow.com/cyclotene/solution/4000oven.htm>.

- [118] "Processing Procedures for CYCLOTENE 4000 Series Resins – DS3000 Immersion Develop Process," <http://www.dow.com/cyclotene/resource/prodlit.htm>.
- [119] G. R. Fulmer, A. J. M. Miller, N. H. Sherden *et al.*, "NMR Chemical Shifts of Trace Impurities: Common Laboratory Solvents, Organics, and Gases in Deuterated Solvents Relevant to the Organometallic Chemist," *Organometallics*, vol. 29, no. 9, pp. 2176-2179, May, 2010.
- [120] J. Zhang, J. Kang, P. Hu *et al.*, "Surface modification of poly(propylene carbonate) by oxygen ion implantation," *Applied Surface Science*, vol. 253, no. 12, pp. 5436-5441, April, 2007.
- [121] D. Briggs, *Surface analysis of polymers by XPS and static SIMS*: Cambridge, U.K. ; New York : Cambridge University Press, 1998.
- [122] "NIST X-ray Photoelectron Spectroscopy Database," <http://srdata.nist.gov/xps/>.
- [123] G. Beamson, and D. Briggs, "HIGH-RESOLUTION MONOCHROMATED X-RAY PHOTOELECTRON-SPECTROSCOPY OF ORGANIC POLYMERS - A COMPARISON BETWEEN SOLID-STATE DATA FOR ORGANIC POLYMERS AND GAS-PHASE DATA FOR SMALL MOLECULES," *Molecular Physics*, vol. 76, no. 4, pp. 919-936, July, 1992.
- [124] R. Sard, "The Nucleation, Growth, and Structure of Electroless Copper Deposits," *Journal of The Electrochemical Society*, vol. 117, no. 7, pp. 864-870, 1970.
- [125] D. Briggs, *Surface analysis of polymers by XPS and static SIMS*, New York, U.S.A.: Cambridge University Press, 1998.
- [126] E. I. Yasuda, M. Inagaki, K. Kaneko *et al.*, *Carbon Alloys: Novel Concepts to Develop Carbon Science and Technology*, Oxford, UK: Elsevier Science Ltd, 2003.
- [127] G. Alonzo, N. Bertazzi, J. R. Ferraro *et al.*, "MOSSBAUER, FAR-INFRARED, AND XPS INVESTIGATIONS OF SNCL₂ AND SNCL₄ INTRODUCED IN POLYCONJUGATED MONOSUBSTITUTED ACETYLENE MATRICES," *Applied Spectroscopy*, vol. 49, no. 2, pp. 237-240, February, 1995.
- [128] J. Pla, M. Tamasi, R. Rizzoli *et al.*, "Optimization of ITO layers for applications in a-Si/c-Si heterojunction solar cells," *Thin Solid Films*, vol. 425, no. 1-2, pp. 185-192, February, 2003.
- [129] F. H. Li, J. X. Song, F. Li *et al.*, "Direct electrochemistry of glucose oxidase and biosensing for glucose based on carbon nanotubes@SnO₂-Au composite," *Biosensors & Bioelectronics*, vol. 25, no. 4, pp. 883-888, December, 2009.

- [130] B. Mirkelamoglu, and G. Karakas, "The role of alkali-metal promotion on CO oxidation over PdO/SnO₂ catalysts," *Applied Catalysis a-General*, vol. 299, pp. 84-94, January, 2006.
- [131] Z. B. Zhou, R. Q. Cui, G. M. Hadi *et al.*, "Mixed phase F-doped SnO₂ film and related properties deposited by ultrasonic spraying," *Journal of Materials Science-Materials in Electronics*, vol. 12, no. 7, pp. 417-421, July, 2001.
- [132] A. Lewera, P. J. Barczuk, K. Skorupska *et al.*, "Influence of polyoxometallate on oxidation state of tin in Pt/Sn nanoparticles and its importance during electrocatalytic oxidation of ethanol - Combined electrochemical and XPS study," *Journal of Electroanalytical Chemistry*, vol. 662, no. 1, pp. 93-99, November, 2011.
- [133] M. Mancini, P. Kubiak, M. Wohlfahrt-Mehrens *et al.*, "Mesoporous Anatase TiO₂ Electrodes Modified by Metal Deposition: Electrochemical Characterization and High Rate Performances," *Journal of the Electrochemical Society*, vol. 157, no. 2, pp. A164-A170, 2010.
- [134] S. A. Bocanegra, A. Guerrero-Ruiz, S. R. de Miguel *et al.*, "Performance of PtSn catalysts supported on MAI₂O₄ (M : Mg or Zn) in n-butane dehydrogenation: characterization of the metallic phase," *Applied Catalysis a-General*, vol. 277, no. 1-2, pp. 11-22, December, 2004.
- [135] A. Sharma, G. Andersson, and D. A. Lewis, "Role of humidity on indium and tin migration in organic photovoltaic devices," *Physical Chemistry Chemical Physics*, vol. 13, no. 10, pp. 4381-4387, January, 2011.
- [136] L. J. Zhi, T. Zhao, and Y. Z. Yu, "Preparation of phenolic resin/silver nanocomposites via in situ reduction," *Scripta Materialia*, vol. 47, no. 12, pp. 875-879, December, 2002.
- [137] R. Adhikari, G. Gyawali, T. Sekino *et al.*, "Microwave assisted hydrothermal synthesis of Ag/AgCl/WO₃ photocatalyst and its photocatalytic activity under simulated solar light," *Journal of Solid State Chemistry*, vol. 197, pp. 560-565, January, 2013.
- [138] M. G. Mason, "ELECTRONIC-STRUCTURE OF SUPPORTED SMALL METAL-CLUSTERS," *Physical Review B*, vol. 27, no. 2, pp. 748-762, January, 1983.
- [139] G. K. Wertheim, S. B. Diczko, and S. E. Youngquist, "UNIT CHARGE ON SUPPORTED GOLD CLUSTERS IN PHOTOEMISSION FINAL-STATE," *Physical Review Letters*, vol. 51, no. 25, pp. 2310-2313, December, 1983.
- [140] K. Santhi, E. Thirumal, S. N. Karthick *et al.*, "Synthesis, structure stability and magnetic properties of nanocrystalline Ag-Ni alloy," *Journal of Nanoparticle Research*, vol. 14, no. 5, pp. 12, May, 2012.

- [141] R. Hultgren, P. D. Desai, D. T. Hawkins *et al.*, *Selected Values of the Thermodynamic Properties of Binary Alloys*, Ohio: American Society for Metals, 1973.
- [142] *ASM Handbook, Volume 3*, Ohio: ASM International, 1992.
- [143] *CRC Handbook of Chemistry and Physics*, Florida, U.S.A.: 69th ed, CRC Press, Inc., 1977.
- [144] J. Knudsen, N. M. Martin, E. Granas *et al.*, "Carbonate formation on p(4 x 4)-O/Ag(111)," *Physical Review B*, vol. 84, no. 11, pp. 6, September, 2011.
- [145] T. E. Felter, W. H. Weinberg, G. Y. Lastushkina *et al.*, "AN XPS AND UPS STUDY OF THE KINETICS OF CARBON MONOXIDE OXIDATION OVER Ag(111)," *Surface Science*, vol. 118, no. 3, pp. 369-386, March, 1982.
- [146] M. W. Abee, "Interaction of Acid/Base Probe Molecules with Specific Features on Well-Defined Metal Oxide Single-Crystal Surfaces," Chemical Engineering Department, Doctor of Philosophy Thesis, Virginia Polytechnic Institute and State University, 2001.
- [147] T. J. Spencer, "AIR-GAP TRANSMISSION LINES ON PRINTED CIRCUIT BOARDS FOR CHIP-TO-CHIP INTERCONNECTIONS," School of Chemical and Biomolecular Engineering, Georgia Institute of Technology, 2010.
- [148] X. B. Lu, and Y. Wang, "Highly active, binary catalyst systems for the alternating copolymerization of CO₂ and epoxides under mild conditions," *Angewandte Chemie-International Edition*, vol. 43, no. 27, pp. 3574-3577, July, 2004.
- [149] "Spectral Database for Organic Compounds (SDBS)," http://sdfs.db.aist.go.jp/sdfs/cgi-bin/cre_index.cgi.
- [150] C. T. Cohen, T. Chu, and G. W. Coates, "Cobalt catalysts for the alternating copolymerization of propylene oxide and carbon dioxide: Combining high activity and selectivity," *Journal of the American Chemical Society*, vol. 127, no. 31, pp. 10869-10878, August, 2005.
- [151] C. Barreto, E. Hansen, and S. Fredriksen, "Novel solventless purification of poly(propylene carbonate): Tailoring the composition and thermal properties of PPC," *Polymer Degradation and Stability*, vol. 97, no. 6, pp. 893-904, June, 2012.
- [152] X. Q. Wu, H. A. Reed, L. F. Rhodes *et al.*, "Photoinitiation systems and thermal decomposition of photodefinable sacrificial materials," *Journal of Applied Polymer Science*, vol. 88, no. 5, pp. 1186-1195, May, 2003.
- [153] J. J. Vlassak, and W. D. Nix, "A NEW BULGE TEST TECHNIQUE FOR THE DETERMINATION OF YOUNG MODULUS AND POISSON RATIO OF

- THIN-FILMS," *Journal of Materials Research*, vol. 7, no. 12, pp. 3242-3249, December, 1992.
- [154] S. K. Chawla, N. Sankarraman, and J. H. Payer, "DIAGNOSTIC SPECTRA FOR XPS ANALYSIS OF CU-O-S-H COMPOUNDS," *Journal of Electron Spectroscopy and Related Phenomena*, vol. 61, no. 1, pp. 1-18, December, 1992.
- [155] G. D. Khattak, A. Mekki, and A. Al-Shukri, "X-ray photoelectron spectroscopy study of copper tellurite glasses," *Physica Scripta*, vol. 70, no. 2-3, pp. 187-192, August-September, 2004.
- [156] M. Yin, C. K. Wu, Y. B. Lou *et al.*, "Copper oxide nanocrystals," *Journal of the American Chemical Society*, vol. 127, no. 26, pp. 9506-9511, July, 2005.
- [157] A. I. Stadnichenko, A. M. Sorokin, and A. I. Boronin, "XPS, UPS, and STM studies of nanostructured CuO films," *Journal of Structural Chemistry*, vol. 49, no. 2, pp. 341-347, March-April, 2008.
- [158] T. Ghodselahi, M. A. Vesaghi, A. Shafiekhani *et al.*, "XPS study of the Cu@Cu(2)O core-shell nanoparticles," *Applied Surface Science*, vol. 255, no. 5, pp. 2730-2734, December, 2008.
- [159] J. Ghijsen, L. H. Tjeng, J. Vanelp *et al.*, "ELECTRONIC-STRUCTURE OF CU2O AND CUO," *Physical Review B*, vol. 38, no. 16, pp. 11322-11330, December, 1988.
- [160] L. G. Sillén, *Stability constants of metal-ion complexes. Supplement no. 1*, 2nd ed., London: Chemical Society, 1971.
- [161] "NIST Chemistry WebBook," <http://webbook.nist.gov/chemistry/>.
- [162] H. BURROWS, H. ELLIS, and S. UTAH, "ADSORBED METAL-IONS AS STABILIZERS FOR THE THERMAL-DEGRADATION OF POLYACRYLAMIDE," *Polymer*, vol. 22, no. 12, pp. 1740-1744, December, 1981.
- [163] J. CRIVELLO, T. LOCKHART, and J. LEE, "DIARYLIODONIUM SALTS AS THERMAL INITIATORS OF CATIONIC POLYMERIZATION," *Journal of Polymer Science Part a-Polymer Chemistry*, vol. 21, no. 1, pp. 97-109, January, 1983.
- [164] "Agilent Split Post Dielectric Resonators for Dielectric Measurements of Substrates," <http://cp.literature.agilent.com/litweb/pdf/5989-5384EN.pdf>.
- [165] S. K. Ryu, J. Im, P. S. Ho *et al.*, "A kinetic decomposition process for air-gap interconnects and induced deformation instability of a low-k dielectric cap layer," *Journal of Mechanical Science and Technology*, vol. 28, no. 1, pp. 255-261, January, 2014.